CHAPTER I

INTRODUCTION

In the late 1970s the mesoscale convective system (MCS) that is referred to as the "bow echo" was identified by Fujita (1978). The bow echo is defined as a curved line of deep convection in the shape of a "bow." Bow echoes are frequently associated with intense damaging winds or downbursts (Johns 1993). As more of these systems were studied, a better understanding was gained concerning their kinematic structure and dynamical processes. Bow echoes can range in size from 15 km to 150 km, and can occur at anytime of year (Klimowski et al. 2000, 2004). Much of the damage reported in the United Sates from non-tornadic winds is a result of bow echo systems.

The conceptual "model" bow echo evolves from a single or large group of strong convective cells, to a bow-shaped line segment, and finally, to a comma-shaped echo in its declining phase (Fujita, 1978). The development of a bow echo can be related to a number of different synoptic variables and conditions. Strong bow echoes that produce widespread damage can occur in strong migrating low pressure systems as well as in rather benign synoptic patterns.

During the Bow Echo and MCV Experiment (BAMEX) ground-based platforms – the Mobile Integrated Profiling System (MIPS) and two NCAR Mobile GLASS (MGLASS) units – were deployed in advance of evolving bow echo and mesoscale convective

systems to monitor their environmental and storm properties of bow echo systems. Three aircraft, the Naval Research Laboratory P-3 (NRL P-3), National Oceanic and Atmospheric Administration P-3 (NOAA P-3), and the Weather Modification, Inc Lear Jet were deployed to the region.

On 24 June 2003 the ground-based instrumentation was deployed at a site just south of Fort Dodge in northwest Iowa. Around 0650 UTC, the ground based and air based systems acquired an excellent data set on a surging bow echo near the time of maximum radial velocity (exceeding 30 m s^{-1}) measured from the Des Moines (DMX) WSR-88D. The peak updraft within deep convection over the MIPS site, ~20 m s^{-1}, occurred about 10 minutes after the gust front arrival. The maximum surface wind gust of 24 m s^{-1} was measured about 10 minutes after the gust front arrival, well behind the leading edge within relatively heavy precipitation. There were several reports of wind damage to structures as well as trees as the storm approached the MIPS location

This case study integrates analyses of data from the ground based and air based platforms. The overall goal is to document, using both the air based and ground based measurements, the life cycle of a bow echo, emphasizing mechanisms of severe weather production and predictability. For this case both ground based and airborne instruments documented the bow echo during the mature and decaying stages as it passed through the Fort Dodge region of central Iowa.

CHAPTER II

BACKGROUND

2.1 General Properties and Climatology of Bow Echoes

There have been numerous studies in the past that have tried to understand how these convective windstorms form, evolve, and dissipate, as well as why some produce damage, while others do not. Some of the more prominent convective wind events are discussed below. One of these events occurred on the early morning of 15 July 1995, when a convective system spawned over Ontario moved across much of upper New York State and central New England, producing surface winds of 30 to over 45 m s^{-1} (60 to over 90 kts), killing 8 people. This storm also produced a large area of tree damage across the Adirondack Mountains (Cannon et al. 1998, McCarthy 1996, Bosart et al. 1998). In another case on 5 May 1996, a MCS moved rapidly across the Lower Ohio Valley, producing wind gusts up to 41 ms^{-1} and widespread wind damage over much of eastern Missouri, southern Illinois and northern Kentucky (Spoden et al. 1998). On the night of 16 May and early on the morning of 17 May 1996, a convective system raced across South Dakota, producing straight-line winds in excess of 50 m s^{-1} (100 kts), toppling nearly 600 power poles and producing widespread damage to buildings (Rasch and Ess, 1998).

Convectively produced windstorms, such as those mentioned above, pose a significant hazard to life and property over much of the U.S. during the spring and summer months. According to Storm Data, from January 1995 to July 2000 over $1.4 billion in property damage, 72 deaths and 1008 injuries were reported to the National Weather Service (NWS) as having been caused by such events. The longer-lived, larger-scale events have been given the general name of "derecho" (Johns and Hirt 1987), a term that originated in the late 1800's to refer to convective systems producing wide and long swaths of straight-line wind damage (Hinrichs 1888). More detailed studies of these systems, however, have shown that a vast majority is associated with a particular type of organized convective wind system, which is more popularly referred to as a "bow echo." This type of system was given the name due to its characteristic bow shape on radar displays. These systems were first described in detail by Fujita (1978), and today, bow echoes represent one of the best-known modes of convective organization associated with severe weather events, especially for high winds.

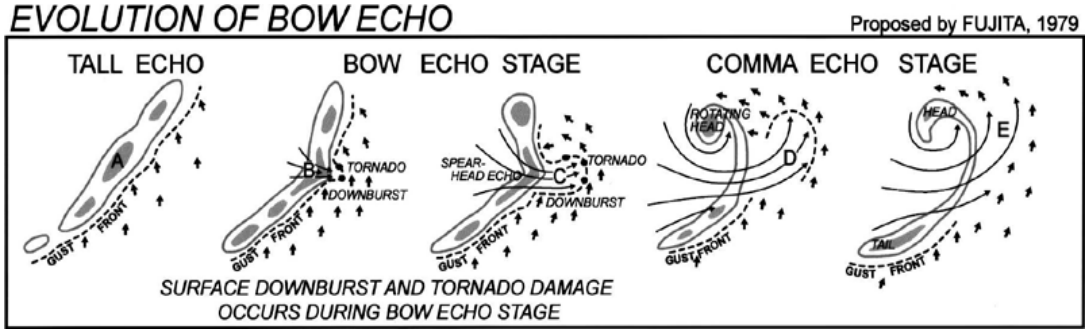

Figure 2.1 Idealized morphology of an isolated bow echo associated with strong and extensive downbursts. Figure adapted after Fujita 1978 (Atkins et al. 2004).

A typical bow echo is best depicted using radar data. A typical evolution of a bow echo is shown in Figure 2.1 (Fujita, 1978). This conceptual model shows a bow echo evolving from a single or large group of strong convective cells, to a bow-shaped line segment, and finally, to a comma-shaped echo in its declining phase. During the early part of the bow echo development stage intense downbursts descend from the strongest echo. This results in distortion along the convective line, or within the individual cell. As the bow continues to intensify, the center may form a "spearhead" type structure, with cyclonic and anti-cyclonic rotations respectively on the left and right of the bow (bookend vortices). As the bow continues to strengthen rear inflow notches along the trailing edge of the line segment may form, denoting where the strongest downburst and winds are located (Przybylinski and Gery 1983; Burgess and Smull 1990; Wilson et al. 1980). During the dissipation stage the system evolves into a large comma-

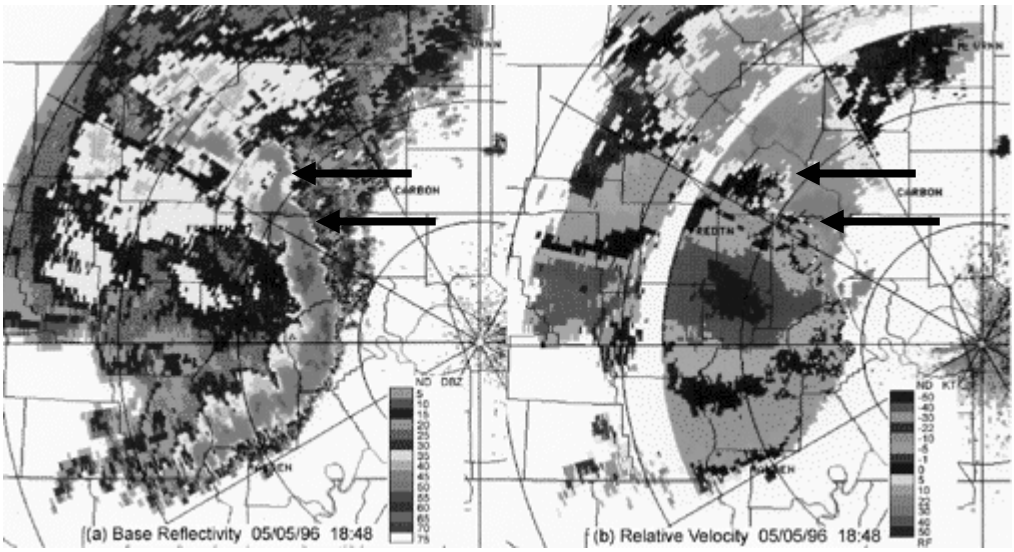

Figure 2.2 (a) Base reflectivity and (b) relative velocity from the Paducah WSR-88D radar at 18:48 GMT for 5 May 1996. Velocities are presented relative to a storm motion of 33 kts from 280 deg. Arrows denote locations of smaller embedded bows along the main bow echo.

shaped echo with cyclonic rotation being prominent (due to the Coriolis force) on the upper end of the bow.

Figure 2.2 shows a typical radar image of a typical mature bow echo system. This example occurred on 5 May 1996 near Paducah, Kentucky and depicts a large bow-shaped convective system which has two smaller scale bows embedded with the larger circulation. These smaller scale bow show that a range of bow echo scales can occur, sometimes within the same convective system. The Doppler radial velocity image shows many of the well known kinematic features of bow echoes, including the rear inflow jet associated with the rear inflow notch behind the core of the system. Also present is an area of weak anticyclonic shear to the south of the bow and string cyclonic shear behind the northern end of the bow.

Besides their association with strong, straight line surface winds, there is also a strong association between bow echoes and tornadoes (e.g., Fujita 1978, Przybylinski et al. 1996, Funk et al. 1996a, Wakimoto 1983, Smith and Partacz 1985, Przybylinski 1988, Funk et al. 1996b, Prost and Gerard 1997, Pence et al. 1998, Wakimoto 2001). A recent study by Tessendoff and Trapp (2000) suggests that bow echo or linear MCS tornadoes account for up to 20 per cent of all tornadic events nationwide. Also, this research has shown that such tornadoes can be quite strong and long-lived. A particularly intriguing property of bow-echo tornadoes is their tendency to be located near or left of the apex of the bow. To date, there has been very little study or research-quality observations of such events. One of the many goals of the BAMEX project was to analyze bow echo and linear MCS tornadoes in greater detail.

On the synoptic scale the development of bow echoes can be related to a number of different variables and conditions. It is interesting to note that strong bow echoes that produce widespread damage can occur in both strong migrating low pressure systems and in stagnant weather patterns. The 24 June 2003 bow echo case occurred during a period when the flow was weak, and air mass was stagnant, which corresponds to the warm season pattern discussed by Johns and Hirt (1987). Also the systems of primary interest for this case study are the especially severe, well-organized bow echoes, which generally range between 40 and 140 km in horizontal scale and have a longevity greater than three hours.

Climatological studies of the synoptic environments associated with severe bow echoes (derechoes) depict a wide range of conditions in which such events occur (e.g., Johns and Hirt 1987, Bentley and Mote 1998, Evans and Doswell 2000). The especially

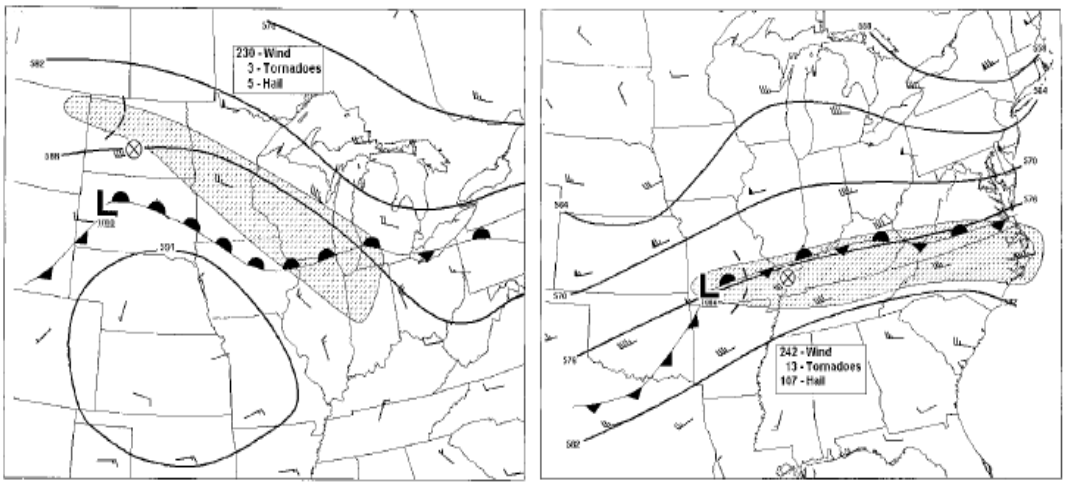

Figure 2.3 Geopotential height and radiosonde winds at 500 hPa along with surface cyclone center position and frontal analysis at 1200 UTC of two severe bow echoes episodes: (a) weakly forced case of July 19, 1983 (left or top), and (b)moderately forced case of June 4, 1993 (right or bottom). Stippled region outlines area of damaging winds during each case. Curved dashed line denotes position of primary convective line at 1200 UTC (from Evans and Doswell, 2001).

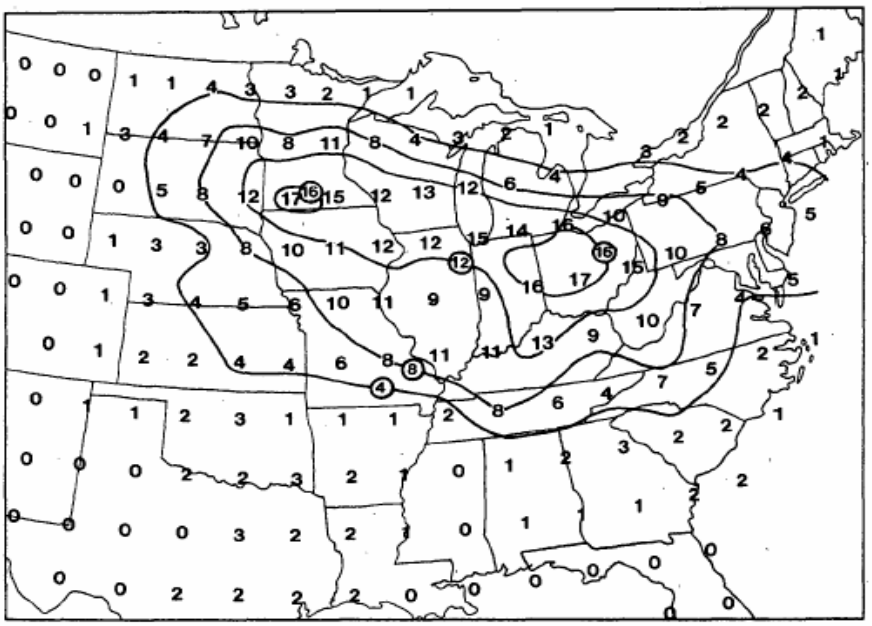

Figure 2.4 Total number of derechoes occurring in during the months of May through August for the period 1980-1983 (from Johns and Hirt 1987).

severe, long-lived events during the warm season (May-August) tend to occur in environments with very large CAPE (e.g., 2000-5000 J kg^{-1}) and moderate-to-strong low-to-mid level shear of the horizontal wind. Wind values tend to be at least 15-20 m s^{-1}over the lowest 2-5 km AGL. These systems may consist of one isolated bow echo or several bow echo segments along an advancing squall line. The most common synoptic pattern that supports bow echo development is described by Johns (1982, 1984) for severe weather outbreaks in northwesterly flow. Over 80% of the 70 events studied by Johns and Hirt (1987) began along or to the north of a weak east-to-west oriented quasi-stationary frontal boundary and then moved along the boundary (Figure 2.3). These boundaries are usually oriented parallel to the mean tropospheric flow. Midlevel winds (500 mb) are typically moderately strong, averaging between 18-21 m s^{-1} from the west to northwest (Johns 1993). The wind direction at the middle and upper levels is generally westerly to northwesterly direction. Water vapor is generally plentiful at the surface, as

well as in the upper levels. Surface temperatures are high, which further promotes high instability, i.e. high values of CAPE. Optimum values have been found by Johns and Hirt (1987) to range from 3500 – 4500 J kg^{-1}. However, there have also been many bows that have formed and matured in areas of low stability near the surface. Many bows form in the early evening hours, and persist well into the nocturnal period. In a recent study of 110 bow echo events, Klimowski et al. (2000) also found that roughly half formed within 50 km of a mesoscale outflow or preexisting thermal boundary.

The specific frequency of bow-echo occurrence has not been directly established, but it can be estimated from the frequencies of the most significant and long-lived bow echo events through recent climatological studies. During the period of May through August for the years 1980-1983, Johns and Hirt (1987) identified 70 such cases in the U.S., most of which occurred over the Midwestern states (Figure 2.4). This figure shows that the highest frequency of derechoes and bow echoes occur over the states of Iowa, Minnesota, Michigan, Illinois, Indiana, and Ohio. More recent climatological studies by Bentley and Mote (1998) and Evans and Doswell (2000) identify a similar corridor of development in the upper Midwest, as well as additional corridors along an axis from Kansas through Oklahoma and Texas, and also in the Southeast.

2.2 Structure of Bow Echoes

Several observational and numerical studies that have examined bow echo kinematics and dynamics, but many unanswered questions about these systems remain. Two important features include the rear inflow jet and the cold pool processes. Both play an important role in the way these systems evolve, mature, and decline.

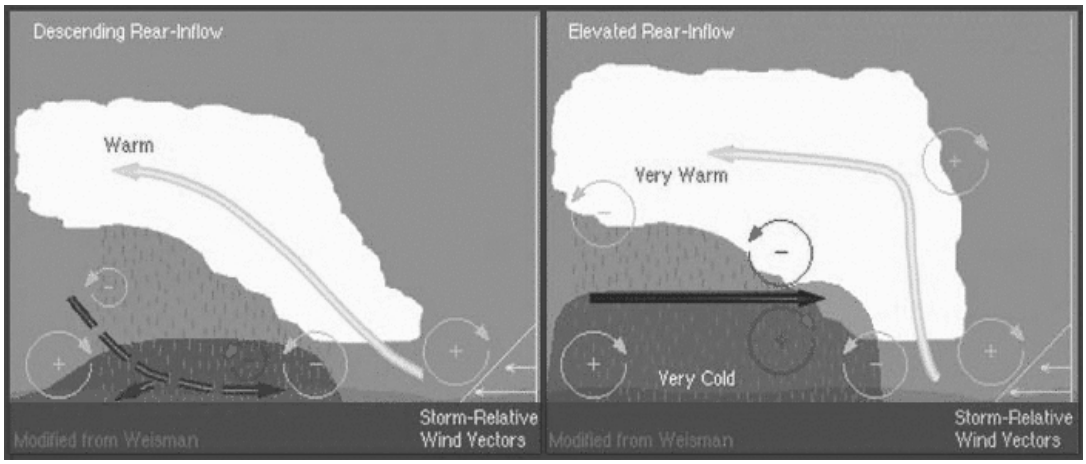

Figure 2.5 Schematic vertical cross section of a mature convective system with (a) descending rear-inflow jet and (b) an elevated rear-inflow jet. The updraft current is denoted by the yellow vector, with the rear-inflow current in denoted by the blue vectors. The shading denotes the surface cold pool. The thin, circular arrows depict the most significant sources of horizontal vorticity, which are either associated with the ambient shear or which are generated within the convective system, as described in the text. Regions of lighter or heavier rainfall are indicated by the more sparsely or densely packed. vertical lines, respectively. The scalloped line denotes the outline of the cloud. (adapted from Weisman, 1993).

Numerical studies have provided valuable insight into the internal structure and evolution of bow echoes. Noteworthy papers include Weisman and Klemp 1986, Rotunno et al. 1988, Weisman et al. 1988, Shamarock et al. 1994, Coniglio and Stensrud 2000. Figure 2.5 shows a two-dimensional picture of two contrasting mature bow echo systems, one with a descending rear-inflow jet (a), and the other with an elevated rear-inflow jet (b). The figure shows a mature system that has evolved from an initially downshear-tilted storm, to upright and then an upshear-tilted configuration as the convectively-generated cold pool strengthened and deepened over time (e.g., Weisman 1993). When an upshear tilt is attained (Figure 2.5a), a rear-inflow jet is

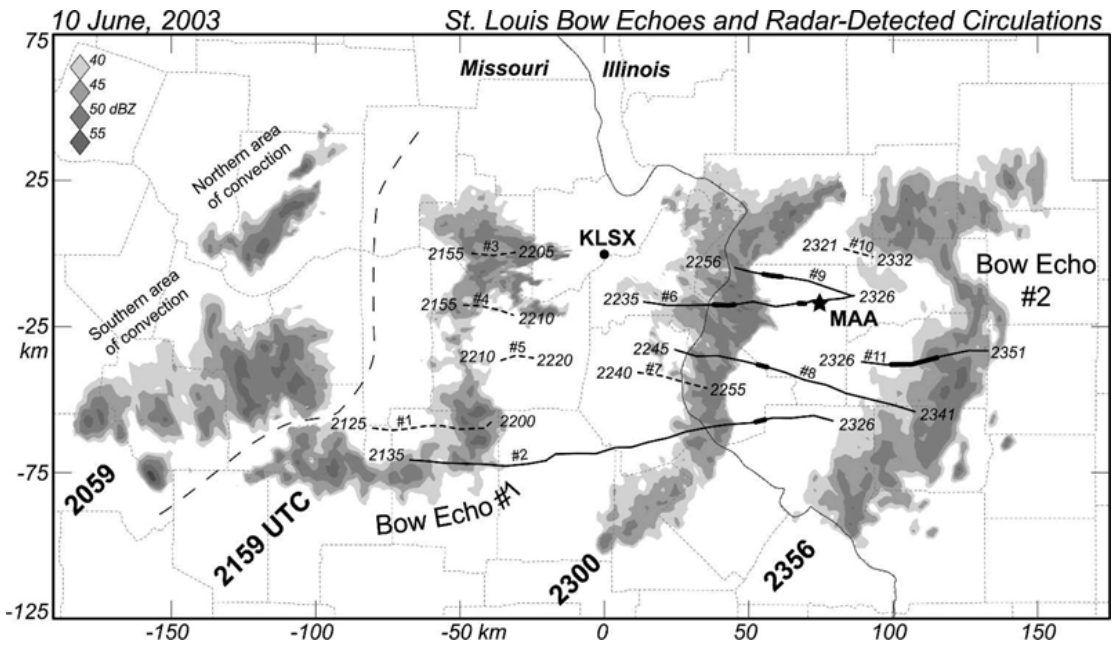

Figure 2.6: Radar reflectivity data from 10 June 2003 from the KLSX radar at 2059, 2159, 2300, and 2356 UTC. Solid and thick-dashed lines represent the locations of radar-detected tornadic and nontornadic mesovortices, respectively. Start and end times (UTC) for all mesovortices are also shown. Thick solid lines along the tornadic mesovortex paths represent the location of observed tornado damage. Thin-dashed lines are county boundaries. The long-dashed line separates the 2059 and 2159 UTC radar data (from Atkins et al. 2004).

generated in response to the buoyant front-to-rear ascending current aloft and rearward spreading cold pool at the surface (e.g., Lafore and Moncrieff 1989; Weisman1992). Figure 2.5a shows a rear-inflow jet has descended to the surface, contributing to stronger surface outflow but weaker leading-line convection. Figure 2.5b shows an inflow jet that remained aloft, enhancing the lifting at the leading edge of the system, and promoting stronger leading line convection.

The mid-level line-end vortices (Figure 2.1) contribute further to bow echo severity by focusing and strengthening the mid-level rear inflow jet between the vortices, thereby enhancing the resultant convective downdrafts and surface outflow. Weisman (1993) and Weisman and Davis (1998) showed that the vorticity source within the line-

end (or bookend) vortices was a combination of both the localized downward tilting of vortex lines associated with the ambient shear layer, as well as the upward tilting of system-generated easterly shear, associated with the cold pool-warm inflow interface along the leading edge of the bow. The relative significance of these vorticity sources depended on both the time in the lifecycle of the system as well as the strength of the ambient shear. The convergence of Coriolis rotation explains the development of a preferred cyclonic vortex on the left end over a several hour period.

Another topic of great interest is the role that mesovortices play in the production of high winds. Weisman and Trapp (2003) and Trapp and Weisman (2003) performed several idealized simulations on bow echo to analyze the mesovortices. From their simulations it was found that many of these mesovortices form just behind the leading gust front, initially anywhere in the along-system direction with typical diameters approximately 2-40 km. As the bow matures the cyclonic northern vortex is most prominent. These simulations also showed that the mesovortices first form within the lowest several hundred meters AGL and grow upwards to the mid-levels. This study did not explicitly address the association between mesovortices and tornadoes. Rather, it showed a strong correspondence between the several long parallel paths of multiple tornadoes within the bow echo system of the type documented by Forbes and Wakimoto (1983) and the long parallel mesovortex paths highlighted in this paper. These mesovortices are thought to make important contributions to generation of strong surface winds.

As technology has advanced during recent years more bow echo observation have been acquired. Since the completion of BAMEX in the summer of 2003, several

published observational studies have provided new insights into the past numerical studies and observational studies. Atkins et al. (2005) analyzed a severe bow echo that produced widespread damage near St. Louis, MO on 10 June 2003. This bow was well sampled by the St. Louis WSR-88D radar. Figure 2.7 shows a radar reflectivity composite from 2059 – 2356 UTC. This system formed from two separate areas of convection and produced two separate bow echoes, one at 2159 UTC and the other one at 2356 UTC. Several tornadic mesovortices were observed within this system. Figure 2.7 shows a time series of radar reflectivity and velocity from 2230-2300 UTC at five minute intervals. This figure shows the formation of the rear-inflow jet, and its relationship to widespread damage. This observation provides some validation of numerical model results, but additional details regarding the descent of this rear-inflow jet remain to be clarified. More numerical and observational studies are required to gain a better understating of the rear-inflow and its relation to damage, maturity, and cold pool.

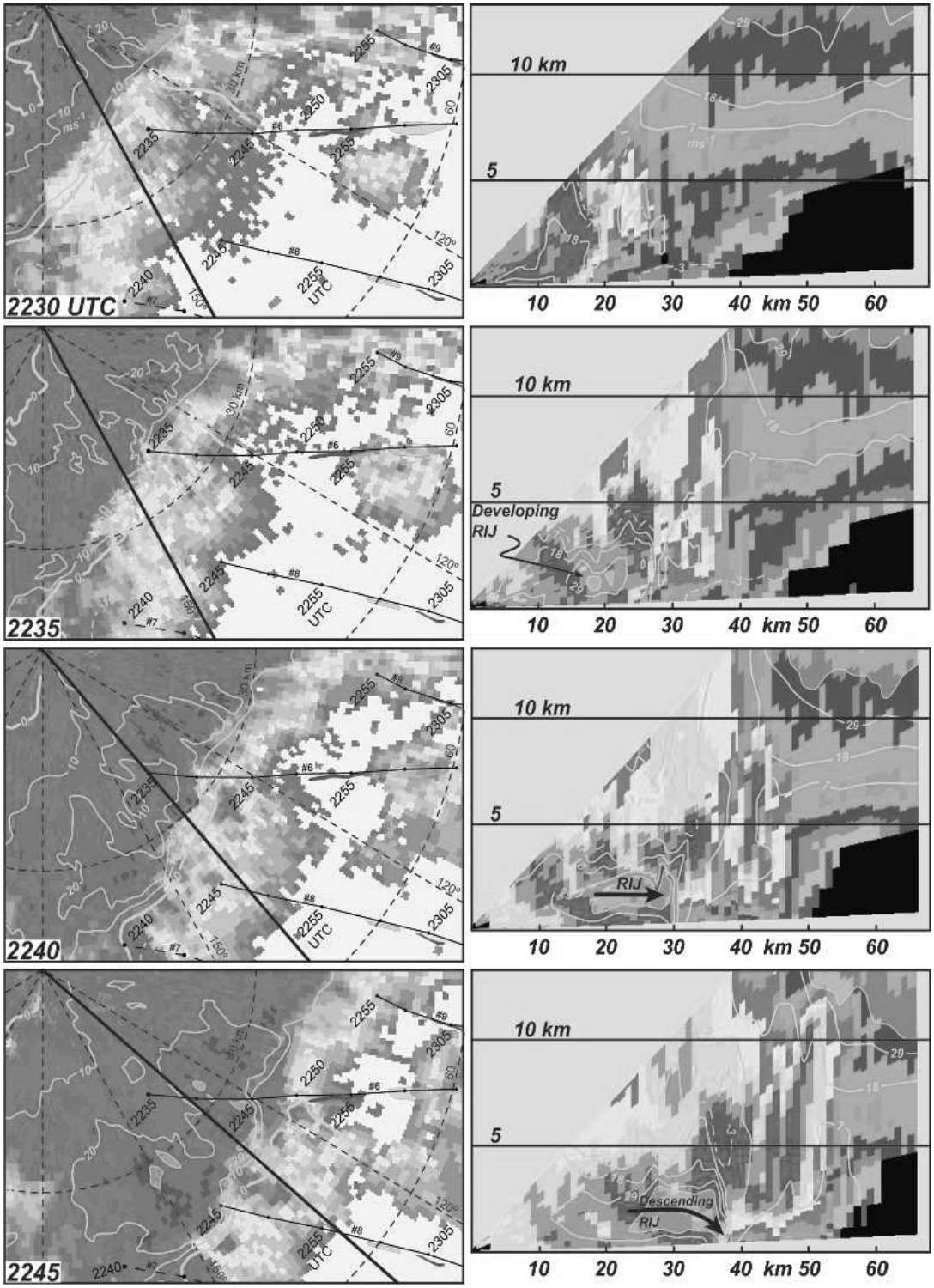

Figure 2.7: Continued on the next page with description (from Atkins et al. 2005).

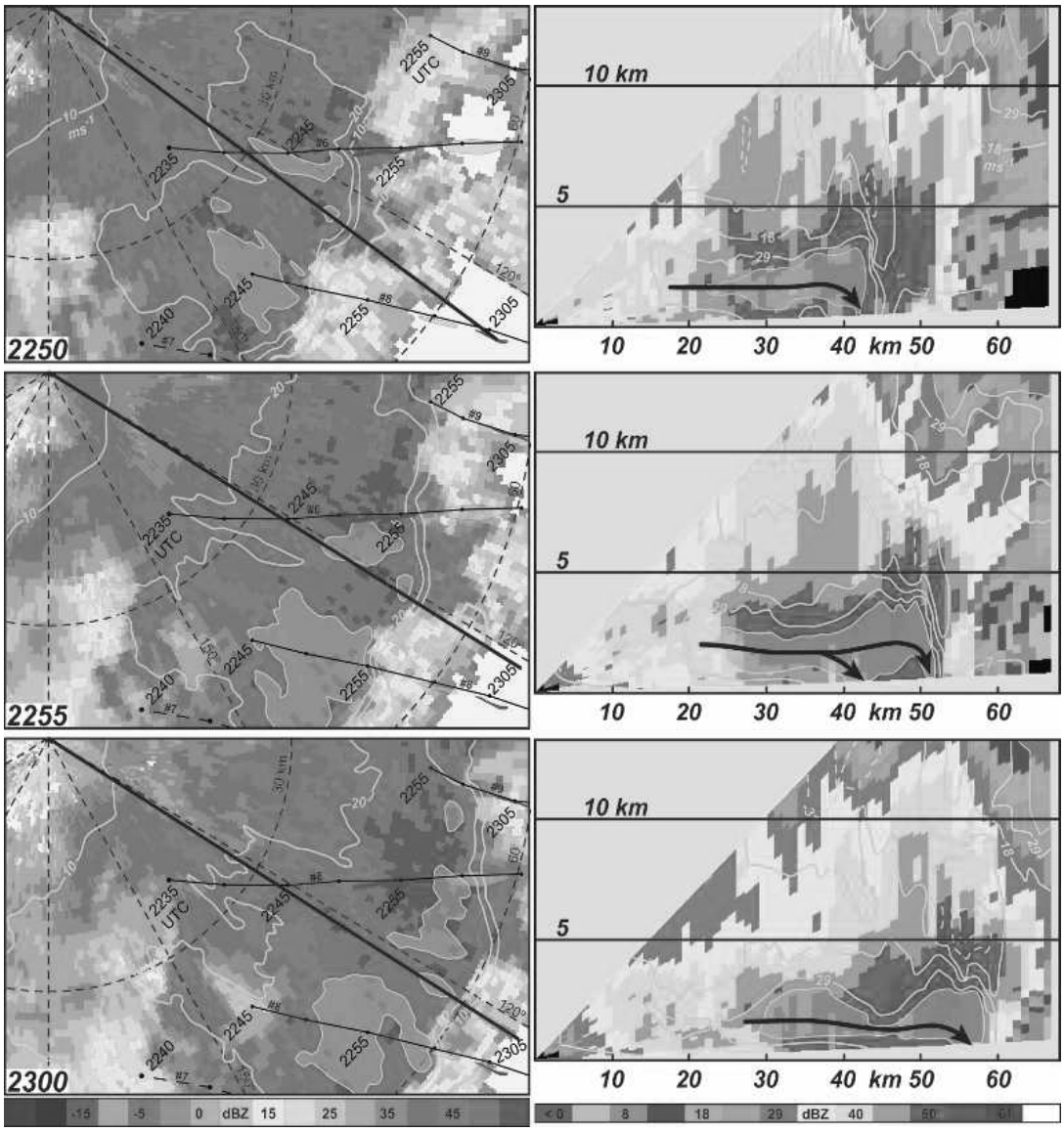

Figure 2.7 Continued: KLSX radar reflectivity (dBZ) and ground-relative radial velocity (m s^{-1}) data in plan view (0.5°), and vertical cross sections from 2230 to 2300 UTC, every 5 min. Radial velocities are contoured with solid dashed contours representing flow away from (toward) the radar. Radial velocities are contoured every 10 m s^{-1} (values greater than 30 m s^{-1} are shaded) in plan view and every 11 m s^{-1} (values greater than 40 m s^{-1} are shaded) in the vertical cross sections. Within the plan view plots, the thick black line represents the location of the vertical cross section at the respective times. Rear in-flow jet is denoted by the black arrow and labels (from

CHAPTER III

OVERVIEW OF THE BAMEX PROGRAM

This chapter provides a short description of the BAMEX field study, a description of the instruments deployed and used for the present study, and a brief description of the characteristics of the experimental domain around the deployment site in Ft. Dodge, IA.

3.1 BAMEX Overview

BAMEX used highly mobile platforms to examine the life cycles of mesoscale convective systems. This project represented a combination of two related programs to investigate (a) bow echoes, principally those which produce damaging surface winds and last at least 4 hours and (b) larger convective systems which produce long-lived mesoscale convective vortices (MCVs). MCVs can focus new convection and play a key role in multi-day convective events affecting a swath sometimes more than 1000 km in length with potential severe weather and flood events. The main objectives regarding bow echoes were to understand and improve prediction of the mesoscale and convective cell-scale processes that produce severe winds. For MCV producing systems the objectives were to understand MCV formation within MCSs, the role of MCVs in initiating and modulating convection, the feedback of convection onto MCV intensity, and to improve the overall predictability of the vortex-convection coupled system.

The BAMEX project facilities consisted of three aircraft, two equipped with a Doppler radar with fore/aft scanning capability to measure internal flows within the convective and stratiform regions of the MCS. The third aircraft was equipped with dropsondes to measure thermodynamic and wind profiles within and around bow echoes and long-lived MCSs. In addition, a mobile array of ground-based observing systems (GBOS) were used to augment airborne radar coverage, document the thermodynamic structure of the PBL, including existing boundaries, probe the surface cold pool, and measure surface horizontal pressure and wind variations within bow echoes and MCS's. The mobile units consisted of the UAH Mobile Integrated Profiling System (MIPS), as well as two NCAR Mobile GLASS units (MGLASS), and the UAH Mobile Probe. The

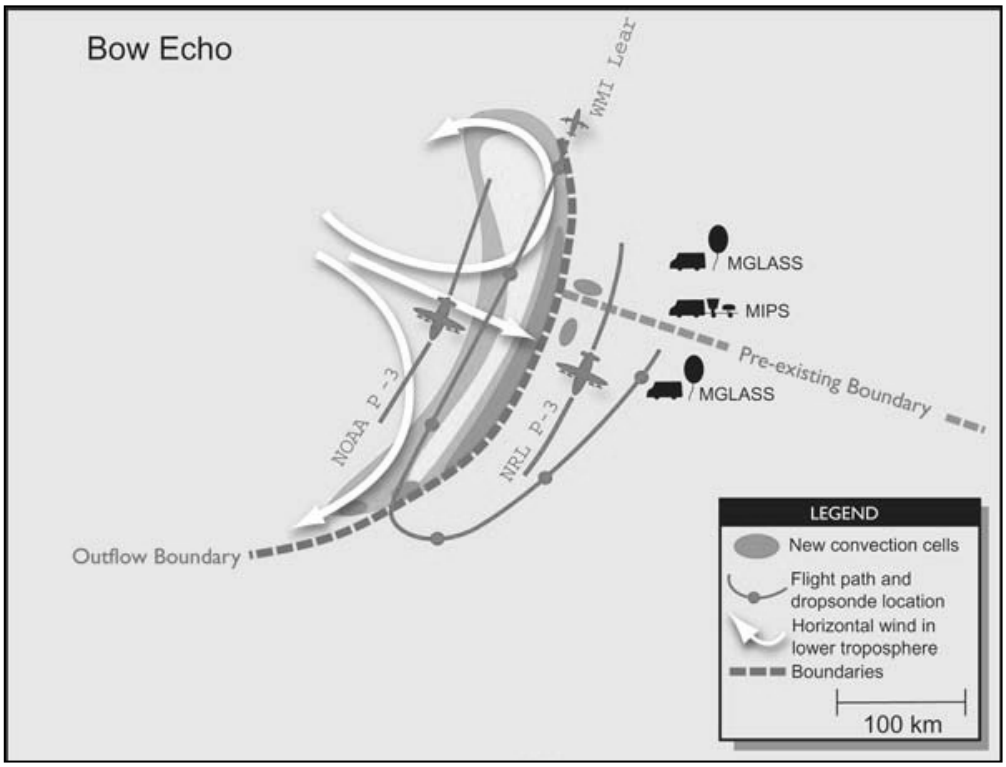

Figure 3.1 Schematic deployment for Bow Echo Case during BAMEX
(from Davis et al., 2004)

combination of aircraft and ground-based measurements was very important for understanding the coupling between boundary-layer and free-tropospheric circulations within bow echoes and MCSs, and, in particular, how the rear-inflow penetrates to the surface in nocturnal severe wind cases.

The basic strategy during BAMEX was to deploy the GBOS several hours prior to the arrival of the bow echo or MCV system. The experimental design was to position the MIPS near the apex of the bow echo, and the MGLASS units were to the right and left of the MIPS position (Figure 3.1). Soundings were released every 1.5 h from the MGLASS units as well as the unit at the MIPS location. The aircraft would reach the location as the system was approaching the GBOS location. The NOAA P3 sampled the trailing stratiform region, and the NRL P3 sampled the leading convective region. Each aircraft was positioned to maximize dual Doppler areal coverage. The Learjet flew over the region and released dropsondes around and within the system.

3.2 Instrumentation

This case study utilizes data from several different ground based remote sensing instruments located on the UAH Mobile Integrated Profiling System, as well as the NCAR Mobile GLASS Units. Data collected from the Des Moines WSR-88D are also analyzed, along with data from the NCAR ELDORA Airborne Doppler Radar on the NRL-P3 aircraft.

3.2.1 The MIPS

The University of Alabama in Huntsville (UAH) has developed a mobile multi-sensor unit termed the Mobile Integrated Profiling System (MIPS). During this study the

MIPS was equipped with a sodar, ceilometer, electric field mill, surface station, microwave profiling radiometer (MPR), and a 915 MHz Doppler wind profiler. The MIPS system also included an NCAR mobile sounding unit, as well as a disdrometer borrowed from NASA/GSFC. For this study all instruments except for the sodar were used. The characteristics of each instrument are discussed in the following paragraphs.

The ceilometer is a model CT25K manufactured by Vaisala. It is a monostatic system with an InGaAs pulsed diode laser that transmits at 905 nm wavelength with peak power of 16 W. The range of coverage is 0 to 7.62 km, with a 30.5 m gate spacing and an integration time of 15 seconds. Ceilometers operate on the principle that particles in the atmosphere, including aerosols, cloud droplets, and precipitation, scatter incident radiation. The ceilometer transmits a pulse of laser energy and then measures the amplitude of backscatter energy. The ceilometer provides vertical profiles of the range-normalized backscatter, from which information can be inferred about relative aerosol concentration, cloud base height, cloud thickness (thin clouds only), and precipitation. The ceilometer is capable of detecting up to three cloud layers, depending on the thickness of those layers and the amount of extinction encountered. Ceilometer backscatter is used in this paper to help infer boundary layer structures before and after the passage of the bow echo system.

The electric field mill (EFM) is a device used to determine the magnitude of the vertical component of the electric field. The device consists of two metallic coaxial disks of the same radius separated by a fixed distance. The axis of these disks is pointed in the direction of the field component to be investigated. The lower disk is radially segmented and fixed in position. The rotating upper disk is similarly segmented but has alternate

segments removed. As that disk rotates the electric field flux to the lower segments undergoes continual change. This changing flux between the stator and rotator induces a voltage between the plates (Uman, 1989). Knowledge of this voltage and the distance between the disks permits the determination of the electric field component. This in turn allows for the detection of the E-field magnitude. The range of detection is approximately a 10 km radius around the field mill location (Walt Petersen 2005, personal communication).

Data was also collected from a surface station located on a rack attached to the roof of the MIPS van. Table 3.1 shows the variables measured by the surface station, the height above ground, the instrument used to make the measurement, and the range and accuracy of the instrument. Measurements were recorded at one second intervals.

Table 3.1 Characteristics of MIPS Surface Station

VARIABLE	**HEIGHT**	**INSTRUMENT**	**RANGE**	**ACCURACY**
Temperature (T)	3 m	Vaisala HMP45C	-35˚ to 50˚ C	<± 0.3˚ C (0˚ to 40˚ C)
Relative Humidity (RH)	3 m	Vaisala HMP45C	.8 to 100%	± 2% (0 to 90% RH) ± 3% (90 to 100% RH)
Wind Speed (u)	3.6 m	RM Young 5103	0 to 60 m/s	± 0.3 m/s (1.0 m/s threshold
Wind Direction (θ)	3.6 m	RM Young 5103	360˚	± 3˚ (0.9 m/s threshold)
Barometric Pressure (P)	3.6 m	Vaisala PTB-101b	600 to 1060 hPa	± 0.5 hPa
Precipitation	.1 m	Texas Instruments TE525	0 to 700mm/ hr	±1% to 25 mm/hr 0 to -2.5% at 25-50mm/hr 0 to -3.5% at 50-75mm/hr

The microwave profiling radiometer (MPR) determines profiles of temperature, water vapor and liquid water (at more limited vertical resolution) up to 10 km AGL at time intervals of about one minute. The 12 channel radiometer measures atmospheric emissions around the water vapor absorption band (5 channels, 22-30 GHz) and the oxygen absorption band (7 channels, 51-59 GHz). The measured brightness temperatures are converted to temperature and water vapor using neural network techniques described in Solheim et al (1998). The system has a mirror that cycles through a tip cycle of selectable elevation angles to calibrate the water vapor measurements. The vertical resolution is inversely proportional to height; thus the atmosphere is sampled at best resolution below several kilometers, particularly within and just above the boundary layer. The system also includes an infrared pyranometer that measures cloud base temperature down to -60˚ C. For uniform cloud layers, this capability extends the cloud base coverage of the ceilometer (7.5 km) to -60˚ C for typical late spring to early summer temperature profiles. For temperature profiling, radiation intensity is measured at points along the low-frequency side (51-59 GHz) of the oxygen absorption band centered near 60 GHz. By scanning downward in frequency from the center, where the opacity is greatest, low level temperature information is estimated. Higher temperature levels are obtained by stepping down in frequency from the peak in the oxygen band. Water vapor profiles are obtained in a similar fashion using the water vapor absorption band near 22 GHz. In this case, the radiometer tunes the 22-30 GHZ range to determine water vapor profiles. Limited resolution cloud liquid water profiles are obtained by taking advantage of the asymmetry in liquid water absorption centered near 60 GHz. Cloud water, if present, contributes more to the 60-75 GHz frequency side than to the 45-60 GHz low

frequency side. The system also includes surface meteorological sensors that measure in situ temperature, relative humidity and pressure. To improve measurements of water vapor and cloud water density profiles, cloud base temperature (and hence altitude) information is obtained with an infrared pyranometer. (Recall that the ceilometer measures cloud base altitude also).

The 915 MHz Doppler wind profiler transmits an electromagnetic beam and measures the Doppler shifted frequency of the backscatter wave caused by irregularities in the index of refraction of the air (Bragg scatter) or precipitation (Rayleigh scatter). The 915 MHz antenna is an electrically steerable micropatch phased array, formatted by four 0.9 m and 0.9 m antenna panels. The current system has five fixed beams, one at zenith, and four beams 23 deg from zenith in orthogonal directions. With the 9˚ beam width, the sample volume width is approximate 15% the value of range (Williams et al. 1995). Thus, at a height of 4 km, the width of the sample volume is ~600 m. The accuracy of retrieved one-hour consensus winds is about 1 m s^{-1} in speed and 10 deg in direction under normal conditions (Knupp 2004). The microwave frequency is also sensitive to all liquid and ice-phase hydrometeors, including raindrops, snow and ice crystals. In the precipitation environment, a strong signal is usually obtained throughout the depth of the cloud system. A return signal is also produced by Bragg scattering due to spatial irregularities of refractive index caused by turbulent motions where vertical gradients in the refractivity index are present (Rogers et al. 1993). The minimum detectable Z (reflectivity factor) is about 11 dBZ at 8 km. The 915 MHz profiler collects Doppler spectra, calculates the spectral moments (return power or reflectivity factor Z, vertical particle motion W, and spectral width σ_v), determines wind profiles at 2-60 min

intervals, acquires vertically-pointing data at 40-60 s time resolution (every other beam is vertical) and 105 m vertical resolution. Table 3.2 summarizes the parameters used during the BAMEX field project.

Table 3.2 Characteristics of the 915 MHz Doppler Profiler

Frequency	915 MHz
Wavelength	32.8 cm
Peak Power	500 W
Pulse Width	0.7 μs
Beamwidth	9°
Nyquist Velocity	20 m/s
Dwell Time per Beam	30 sec
Gate Spacing	105 m
Number of Spectral Points	256

Accurate measurements of drop-size distributions are fundamental to estimation of vertical air motion within a storm system. Drop-size distributions above the surface (in clouds) are difficult to observe directly. These measurements are typically obtained from small sample volume probes mounted on aircraft. Unlike scanning radars, UHF (915 MHz) wind profilers sample in the vertical direction within a relatively small spatial domain, allowing them to resolve small-scale variations in vertical air motion (via Bragg scatter) and precipitation (Rayleigh scatter) patterns, thus avoiding many of the range-dependent errors inherent in traditional scanning radar estimates of rainfall. The combination of UHF profilers and disdrometers represents a powerful combination capable of providing a profile of drop size distributions given that UHF profilers are able

to detect air motion (Tokay et al. 1999). During BAMEX the MIPS was equipped with a Joss-Waldvogel disdrometer which was able to determine the drop size distribution which can be used with the 915 MHz Profiler to determine the vertical air motions within the bow echo system. Table 3.3 shows the specifications for the disdrometer used during BAMEX (Distromet LTD 2005, http://www.distromet.com/1_index_e.htm)

Table 3.3 Joss-Waldvogel Disdrometer Specifications

Range of drop diameter	0.5 mm to 5 mm
Sampling area	50 cm^2
Accuracy	+/- 5% of measured drop diameter
Resolution	127 size classes distributed more or less exponentially over the range of drop diameters
Operating temperature range	0 to 40 degree Celsius for processor 0 to 50 degree Celsius for sensor
Dimensions of the sensor	10 cm x 10 cm x 17 cm high

3.2.2 NCAR M-GLASS Sounding Units

The NCAR M-GLASS facility is a completely self-contained unit that can be carried by van or truck. The basic system contains all the hardware required to make up to four simultaneous atmospheric soundings. The high mobility of this system allows deployment to a specific site to make a sounding, and if required move to another site for the next sounding. The first sounding can be active and in the air while the vehicle is mobile without affecting sounding quality. Sounding site station elevation values are typically taken from a GPS unit located with the vehicle.

The sondes used by the MGLASS units are the Vaisala RS-80-15 model. The rawinsonde package includes a 403 MHz band transmitter, a GPS receiver, and pressure, temperature, and relative humidity sensors. Table 3.4 lists the specifications for the devices in the rawinsonde package. Both the thermodynamic and navigation signals are transmitted roughly every 1.5 seconds to the MGLASS data system to be processed and archived. The data was processed by NCAR to refine the data into a high quality data set (NCAR 2004, http://www.atd.ucar.edu/rtf/facilities/class/class.html).

Table 3.4 MGLASS Rawinsonde Specifications

Manufacturer - type	Vaisala RS 80-15 GH
Ascent Rate	4 m/s avg
Pressure Measurement	BAROCAP Capacitive aneroid
Range	3 to 1060 mb
Accuracy	0.5 mb
Sensor Resolution	0.1 mb
Temperature Measurement	THERMOCAP Capacitive bead
Range	-90°C to 60°C
Accuracy	0.2 C
Sensor Resolution	0.1 C
Relative Humidity Measurement	HUMICAP thin film capacitor
Range	0 - 100% Relative Humidity
Accuracy	2.0% Relative Humidity
Wind and Position Measurement	MWG201
Wind Accuracy	0.5 m/s
Averaging Time	0.5 seconds

3.2.3 NCAR Electra Doppler Radar (ELDORA)

The ELDORA radar is mounted on the Naval Research Lab (NRL) P3 aircraft and can sample storm motions over a domain extending 30-60 km out from the flight track. This system operates in the X-band (3.2-cm wavelength) region, and consists of two Doppler radars. The research flight speed of the P-3 aircraft is approximately 130 m/s.

At this flight speed the scientific requirement for samples every 300-500 m dictates an antenna rotation rate of approximately 24 RPM. The peak powers of the radars are between 35 and 50 kW, and the radars have a beamwidth and antenna gain of 1.8 degrees and 40 dB, respectively. The radar transmits two beams that scan over two cones, one pointed 18 degrees forward and the other pointed 18 degrees aft of a plane perpendicular to the aircraft heading (Figure 3.2). This technique allows the radar to collect pseudo dual-doppler information as the aircraft flies past or through storms. This is accomplished by analyzing the fore and aft looks from ELDORA to yield two wind components for each location in the atmosphere. Applying conservation of mass, a 3-dimensional airflow can be retrieved (Jorgensen et al. 1996). The ELDORA derived parameters include radar reflectivity factor, radial velocity, spectral width, and normalized coherent power. During a standard flight the data from both the fore and the

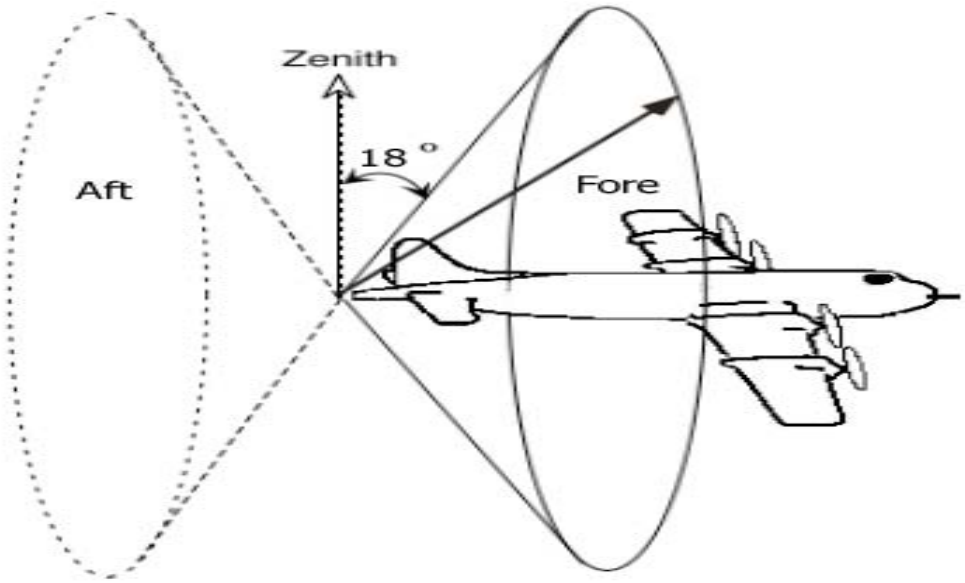

Figure 3.2 Scanning geometry of the ELDORA Doppler radar. The antenna scans are 18° forward and aft from the aircraft's track (Jorgensen et al. 1996).

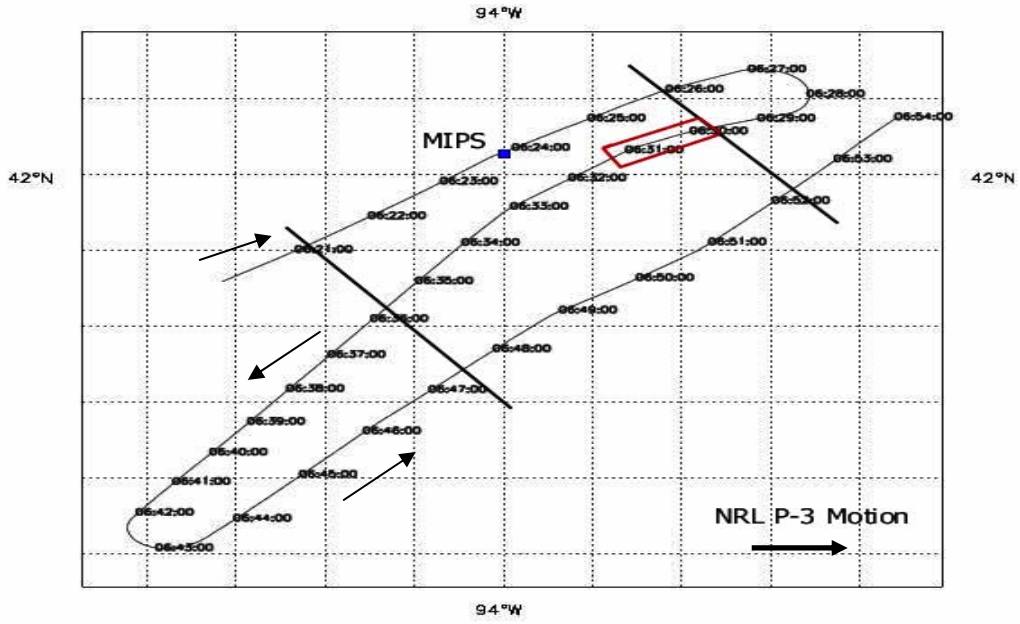

Figure 3.3 Track of the NRL P-3 Aircraft. Leg 1 begins at the top; leg 2 is next, followed by leg 3. The area in red is a location where the aircraft was not close enough to the system for a valid dual Doppler comparison. The area used in this case study is located between the solid black lines.

aft radars are tagged with the aircraft position information for subsequent detailed psueudo dual-Doppler processing (NCAR 2004, http://www.atd.ucar.edu/rsf/eldora/eldora.html).

A rigorous process is required to synthesize the ELDORA data. The data are first corrected for aircraft roll, pitch, air speed, and height above ground for each individual leg. For this case, three legs were selected, one prior to bow echo passage over the MIPS, and two after passage over the MIPS Figure 3.3 shows these three legs relative to the MIPS location. The Doppler data were then edited using the SoloII software. This step included ground clutter removal, velocity dealiasing, and removal of 2nd trip signals.

The third processing step involves two separate programs developed by NCAR personnel. These programs are termed REORDER (a program for gridding radar data) and CEDRIC (Custom Editing and Display of Reduced Information in Cartesian Space).

After these programs are executed plots of various fields, such as radar reflectivity, radial velocity, and dual Doppler winds are created. This data is then checked for consistency intercomparison with other data sets produced by the MIPS. The program REORDER transforms radar data from radar space to Cartesian space so that various analyses can be preformed. REORDER processes the fore and aft radar data separately so that errors are minimized. For this analysis the grid was centered over the latitude (42.43˚ W) and longitude (-94.20˚ N) of the MIPS. The grid size was determined by the length of the legs near the MIPS. The domain extent was 78 km in the west-east direction, 90 km in the north-south direction and 16 km in the vertical. The grid spacing was 0.75 (dX) X 0.75 (dY) X 0.50 (dZ) km respectively. The radii of influence values used were 0.75 km in the horizontal and 0.5 km in the vertical. For each leg the reference time was set to the middle of the time series for that leg. Advection of the system was added by using the Des Monies WSR-88D radar to determine the storm motion vector from 308˚ at 16.5 m s^{-1}. A Cressman weighting scheme was used in the interpolation. The weight function (W) is expressed as

$$W = \frac{R^2 - r^2}{R^2 + r^2},$$

$$R^2 = dX^2 + dY^2 + dZ^2,$$

where R is the radius of influence, and r^2 is the square of the distance between a radar gate sample and the grid point (Oye et al., 1995). After this program was executed two files were created which were read into CEDRIC, integrated, and displayed.

CEDRIC is deigned to analyze gridded single and multiple Doppler radar volumes. CEDRIC options include numerical mathematical operators, filtering, divergence calculations, and dual Doppler synthesis. After processing the data CEDRIC

produces a wide range of graphical outputs for further analysis and interpretation (Miller et al., 1998). For this case study the fore and aft radial velocity data were used to synthesis horizontal wind vectors and reference grid points. Vertical motion was obtained by integrating the horizontal divergence field using the amelastic approximation and applying top and bottom boundary conditions that are a fraction of the divergence at those points. To better allow for a synthesis of this data with the fixed MIPS system the coordinate system for each leg was rotated by 135.5˚ to align with true north. The next step was to fill and patch several holes in the data from areas where the plane had turned sharply to avoid intense cells, updrafts, or downdrafts within the system. This was done by performing a two-dimensional, linear, local-least-square method of patching missing data. After this process the data was filtered to remove outliers by performing a Leise three-dimensional filter, and then a Leise two-dimensional filtering. Finally vertical motion was determined from integration of the anelastic mass continuity equation using a variational approach to satisfy bottom and top boundary conditions.

3.2.4 Nation Lightning Detection Network (NLDN)

The NLDN has over 100 ground-based remote sensors throughout the United States, including 59 Lightning Position and Tracking System (LPATS) sensors. Each sensor is based on time-of-arrival (TOA) information, which determines lightning locations by measuring the time of lighting radio pulses from network antenna surrounding the lightning strike. For this study, the detected NLDN cloud-to-ground (CG) flashes for the MCS were determined by calculating the total number of CG flashes within a 10 km x 10 km box around the MIPS location. From this a total count of positive and negative flashes was calculated.

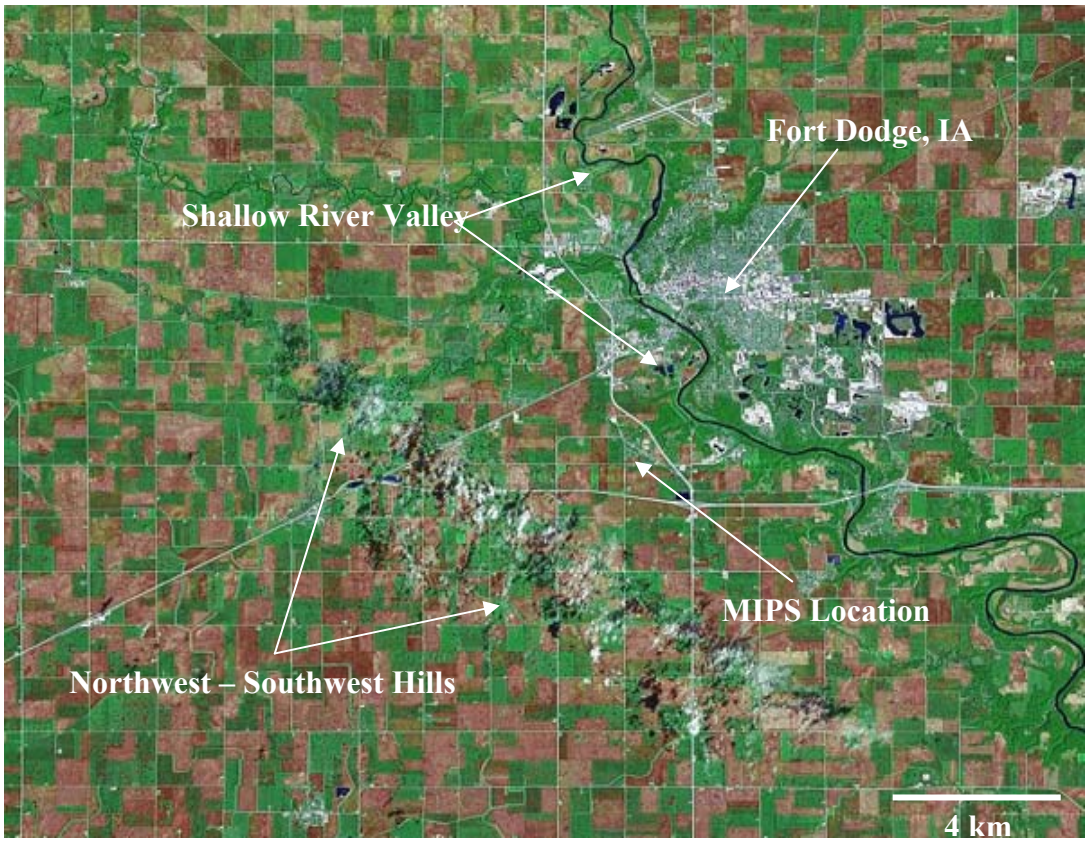

Figure 3.4 Satellite view of the domain area. Fort Dodge is located in the upper right. Other locations are marked on the map.

3.3 Characteristics of the Experimental Domain

The experimental domain, shown in Figure 3.4, is located in the Fort Dodge, Iowa area. The town of Fort Dodge was located the east of the MIPS location. The elevation of the domain varies only slightly from east to west and from north to south, with the average elevation about 540 m above mean sea level (MSL). A shallow river valley runs from the northwest to the southeast northeast of the MIPS location. The depth of this valley is approximately 30-40 m below the MIPS elevation. A line of hills, with the ridge tops averaging about 20 m above the MIPS elevation is located to the west and southwest

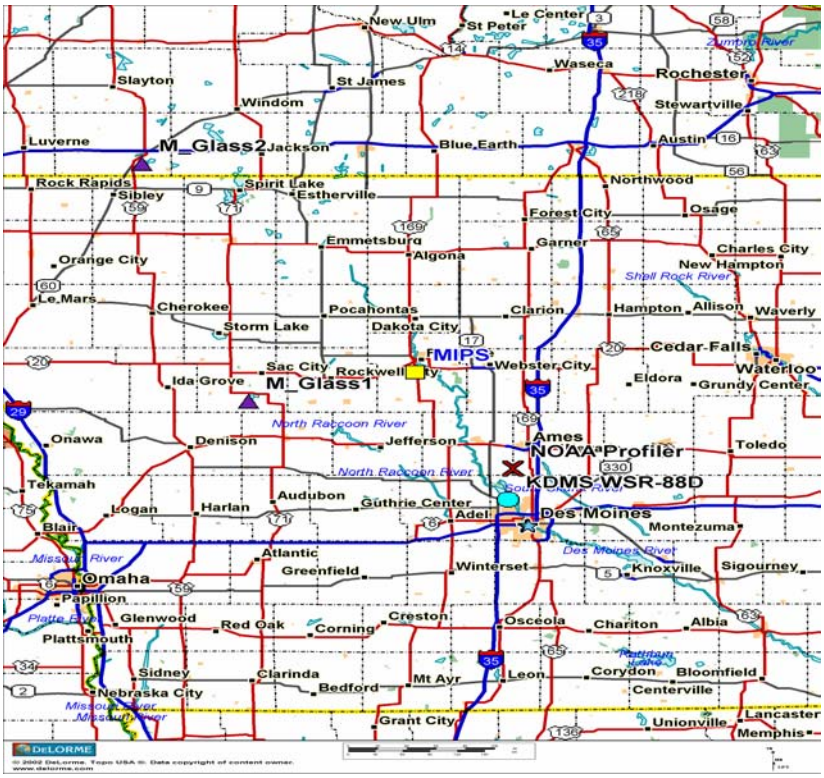

Figure 3.5: Overview of the locations of the Ground Based Instruments used in the case study of the June 24 2003 Bow Echo Case.

of the MIPS. The remainder of the terrain in the vicinity of this case study was flat agricultural land with few structures or trees.

The MIPS was located at an azimuth of 325˚ and a range of approximately 86 km from the Des Monies WSR-88D radar. The MGLASS1 unit was deployed 76 km to the west-southwest of the MIPS, and MGLASS2 was deployed 176 km to the northwest (Figure 3.5).

Surface data included a relatively dense network consisting of Automated Surface Observing Systems (ASOS) as well as sites from the Iowa Department of Transportation, and Iowa Mesonet. Two Suominet sites were located in the domain, with one in Slater, IA collocated with the 404 MHz profiler, and one located in Omaha, NE. These Suominet

sites use Global Positioning Satellites (GPS) to measure precipitable water vapor (PWV) through the atmospheric column in real-time across the region.

CHAPTER IV

MESOSCALE SETTING

4.1 Synoptic Overview

The 24 June bow echo case occurred over Iowa, Minnesota, Illinois, and Michigan. This mesoscale convective system (MCS) started out as a group of small intense cells over northeastern Nebraska near 0100 UTC, and developed into a bow echo system by 0500 UTC. The MCS continued to intensify as it moved eastward across Northern Iowa into Minnesota.

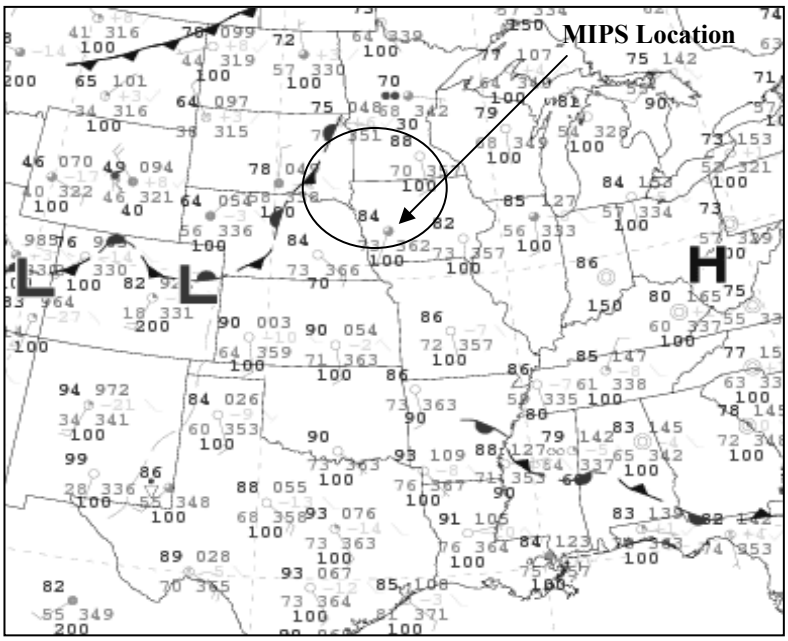

Figure 4.1 Surface plot for 0000 UTC on 24 June 2003

Figure 4.1 shows the synoptic scale surface patterns at 0000 UTC on the 24 June. A stationary front was draped across South Dakota, Nebraska, and into Colorado. The initial convective cells formed along and ahead of this stationary boundary. The contrast across the front was appreciable, with surface dew points in the upper 50's, surface temperatures in the 70's, and winds from the north on the west side, while on the east side the dew points were in the lower 70's, with temperatures in the lower 80's. The winds averaged 5 m s^{-1} from the south-southeast on the south side of the front, while on the north side they were light and variable.

Figure 4.2 shows the 500 mb flow, temperature, and height for this case. As noted by Johns (1993) and others, bow echo formation is most likely to occur with a westerly 500 mb flow, temperatures of -10 ˚C, and 500 mb wind speeds at least 11m s^{-1}. In this case the bow echo formed in a region with westerly winds, and

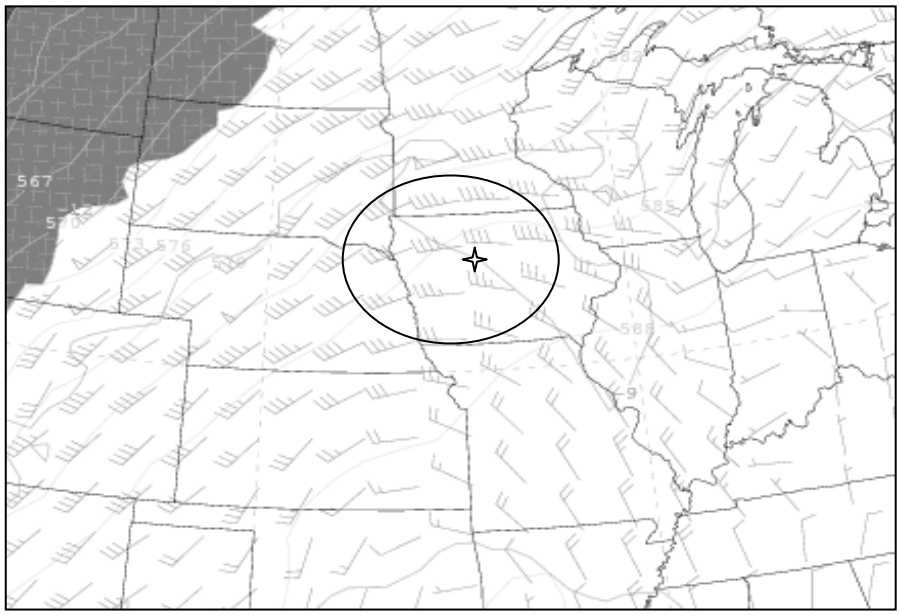

Figure 4.2 Analysis 0000 Z RUC analyses of 500 mb wind (kts), temperature (˚C), and height (mb) at 0000 Z 24 June. The region of interest is contained within the elliptical area. The MIPS location is denoted by the star.

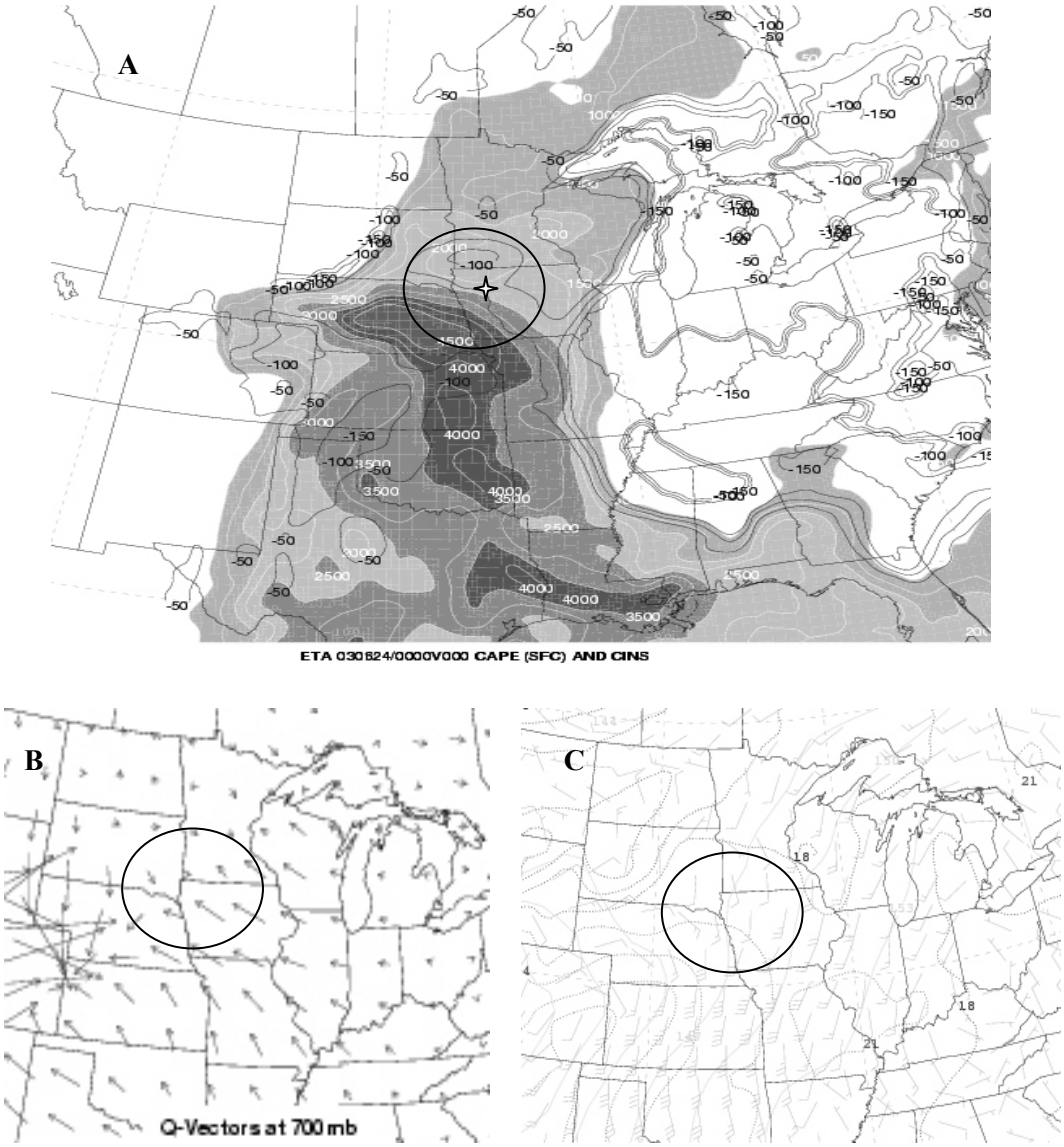

Figure 4.3 (a) RUC 00Z Analysis of CAPE from 0000 UTC on 24 June. (b) RUC Analysis of Q-Vectors at 700 mb for 0000 UTC on 24 June. (c) The 850 mb heights, wind, and temperature for 0000 UTC on 24 June.

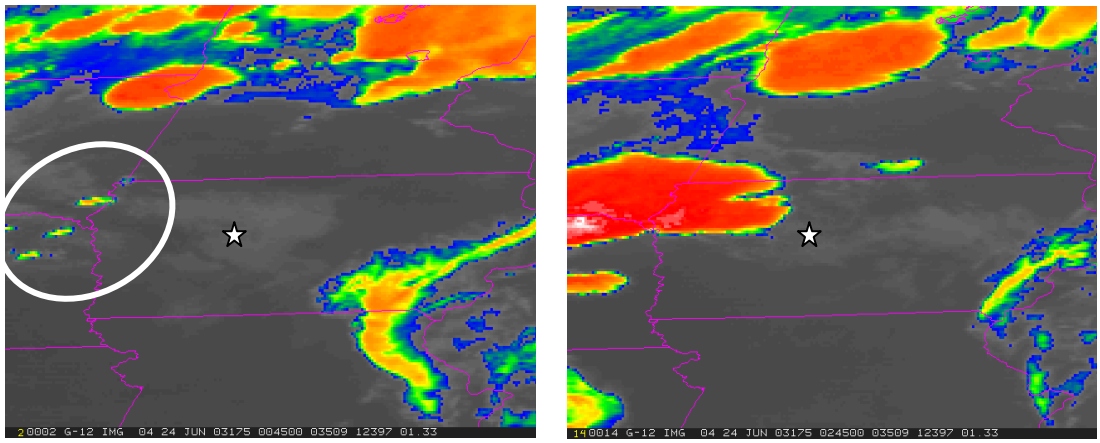

Figure 4.4: GOES IR images from 0045 and 0245 UTC for 24 June 2003. The Circular area is the location of initiation. Within 2 hours convection had organized into a large cluster of convective cells. MIPS is located at the star.

a 500 mb temperature of -9.5° C. The 500 mb wind speeds were approximately 21 m s^{-1}. The 700 mb Q-vectors (Figure 4.3) show prominent convergence over northwestern Iowa, eastern Nebraska, eastern South Dakota, and southern Minnesota. Such convergence is related to the strongest rising motion near the stationary front (Carlson, 1998). As the initial convection was forming along the stationary front, the 700 mb relative humidities were in the 90-95% range in that area. This abundant middle level water vapor supported the deep convection that occurred with the MCS.

Stability is a crucial parameter to the structure and evolution of MCS's and other convective weather systems. Past studies have found that most warm season bow echo systems are associated with a lifted index of -8 or less. In this case the lifted index values were around -7. Higher lifted indices of -4 to -6 were located to the southeast when the system formed. As the MCS moved eastward, it encountered this greater stability and weakened. The convective available potential energy (CAPE) analysis (Figure 4.3a) shows highest values of about 4500 J kg^{-1} just south of the region of convective initiation. The CAPE values in the area of interest at 0000 UTC were near 2000-2500 J kg^{-1}. Johns

(1993) stated that long-lived bow echoes were associated with an average CAPE of 4500 J kg^{-1}. In this case the average CAPE value at 0000 UTC was near 2500 J kg^{-1}, which was shown by this analysis as well as from MGLASS soundings ahead of the system. This less than optimal CAPE may have limited the MCS lifetime. The nocturnal boundary layer (NBL), which is vitally important to stability and bow echoes will be discussed in detail in chapter 5.

At 850 hPa southerly winds of 5-10 m s^{-1} existed over the domain. An east-west temperature gradient, with warmer air to the east, may have been a factor in the low-level stabilization and MCS weakening. According to Johns and Hurt (1987) warm air advection (WAA) occurred within 320 km in all bow echo cases studied. The warm air advection was occurring from the south and west, and in this case analyzed at 950 hPa.

4.2 Mesoscale Surface Analyses

On the mesoscale several important features of interest were noted during the time preceding the bow echo as well as during the passage. Figure 4.5 shows the surface conditions for 0000 UTC and 0600 UTC on June 24 for the greater Iowa region. As convective initiation was occurring (Figure 4.4) in the southeast corner of South Dakota, the temperatures and dewpoints in the region were in the range of 30-31˚ C and 20-23˚ C, respectively. To the south of the initiation region, dewpoint values were higher, with some stations recording values of 25˚ C near the Missouri and Iowa border. There was also a north-south gradient over Iowa in dewpoint due to a heat burst event on the previous night over the domain. The winds were generally southerly, (180˚) averaging 5 m s^{-1} across the domain. However near the initiation point winds were out of the

southeast, as well as in the sites in Nebraska. An area of convergence over the southeast corner of South Dakota corresponded to the location of the initial convection after 0000 UTC.

Figure 4.6 shows the same region 6 hours later when the bow echo system was near the location of the ground based units. At this time special soundings revealed a well developed nocturnal boundary layer over central Iowa. Over western Iowa temperatures ahead of the MCS were in the range of 25-27˚ C. The advection of warm moist air continued over the region, as shown by the stronger southerly to southeasterly winds across Iowa. This advection was noted in section 4.1 in the 850 mb charts as well as the synoptic scale surface charts. Dew points had risen slightly to values closer to 22-25˚ C across the region. Behind the MCS temperatures and dew points are much lower due to the rain and cold pool associated with the bow echo. Winds speeds increased to about 8 m s^{-1} from the south across the region at 0600 UTC.

An analysis of pressure and equivalent potential temperature (θ_e) fields is presented in 4.7 for 0000 UTC and 0600 UTC. At 0000 UTC θ_e advection was occurring over western Iowa. There also appeared to be a subtle boundary located over northern Iowa as a result of the heat burst event on the previous day. Convective initiation occurred within the northern gradient of θ_e values between 350-354 K. The air to the east had similar values of 350-354 K, while the air to the south had much higher values between 366-368 K. At 0600 UTC the values of θ_e had not changed ahead of the system, but within the cold outflow, θ_e values had decreased to values of 334-346 K. Along the leading edge there was a sharp contrast in θ_e from 350 K to 340 K within a 80 km range.

This is expected since downdrafts within the MCS would transport lower θ_e values to the surface.

The pressure field analysis at 0000 UTC (Figure 4.6a) reveals an increase from west to east, ranging from 1004 mb to 1010 mb on the eastern boarder of Iowa. Figure 4.6b shows the pressure contours six hours later over the same domain. The pressure has increased across the entire region, and was especially high behind the MCS. In Ft. Dodge, IA the pressure ahead of the MCS increased from 1008 mb at 0000 UTC to 1010 mb at 0600 UTC as the MCS approached. As the MCS passed the MIPS position it encountered lower θ_e values which aided in the decay of the southern portion of the system. This section of the MCS continued away from the stationary boundary that initiated convection. However to the north in Minnesota the northern MCS strengthened shown by lower pressures and high values of θ_e.

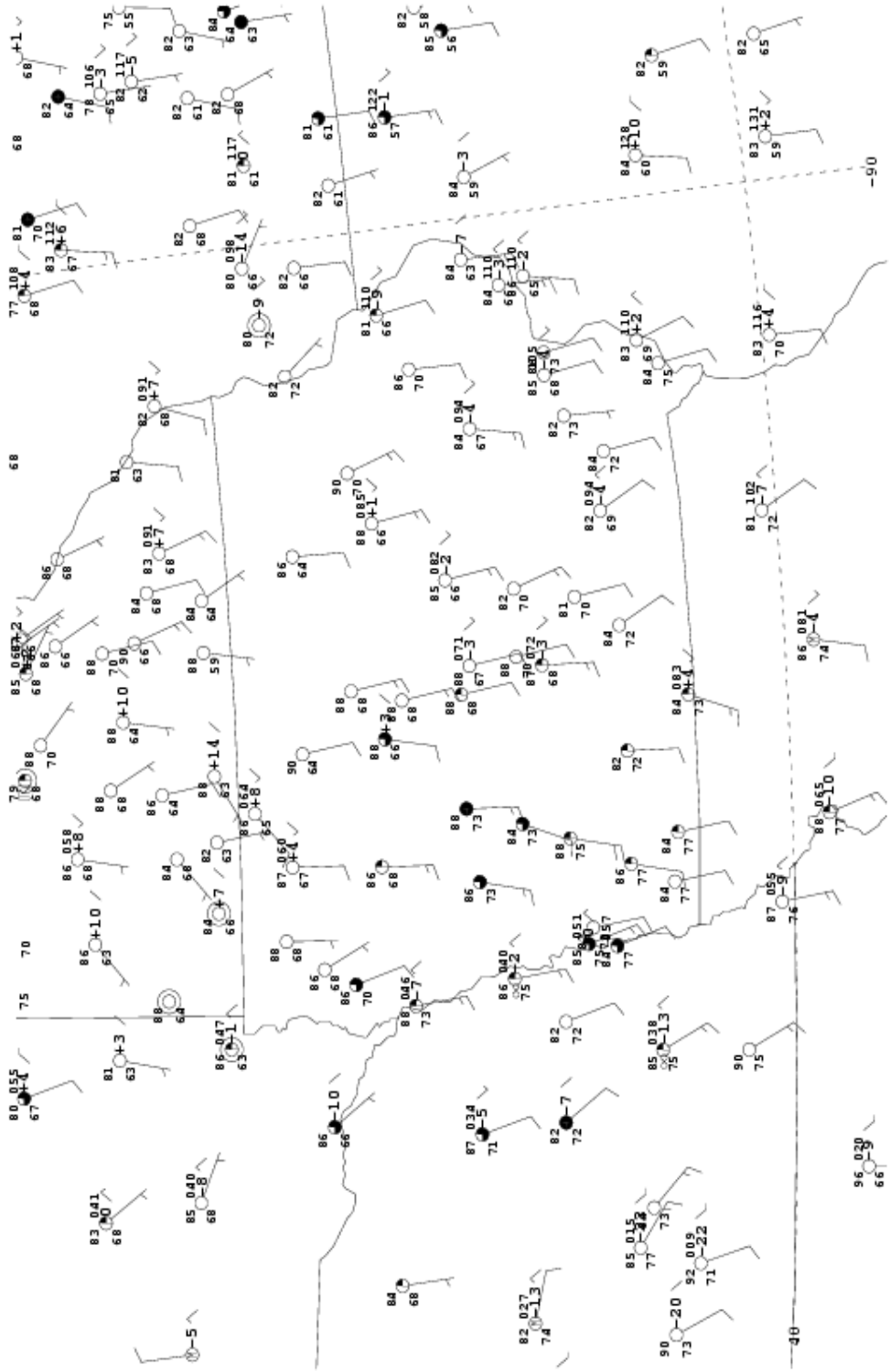

Figure 4.5 shows the surface conditions over the domain for at 0000 UTC on 24 June 2003.

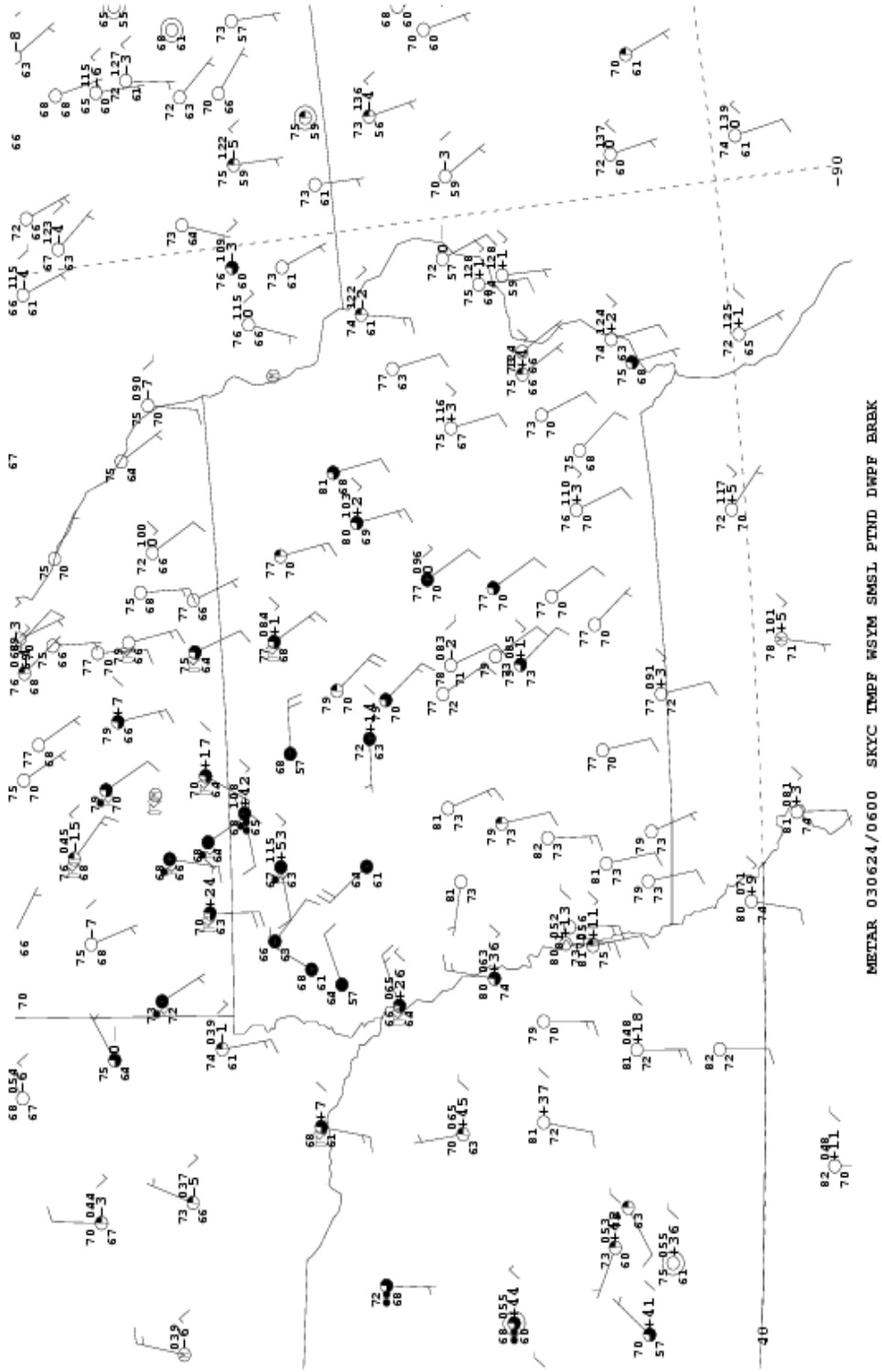

Figure 4.6 shows the surface conditions over the domain for at 0600 UTC on 24 June 2003. Note the change in wind direction from southerly to southeasterly during this 6 hour period.

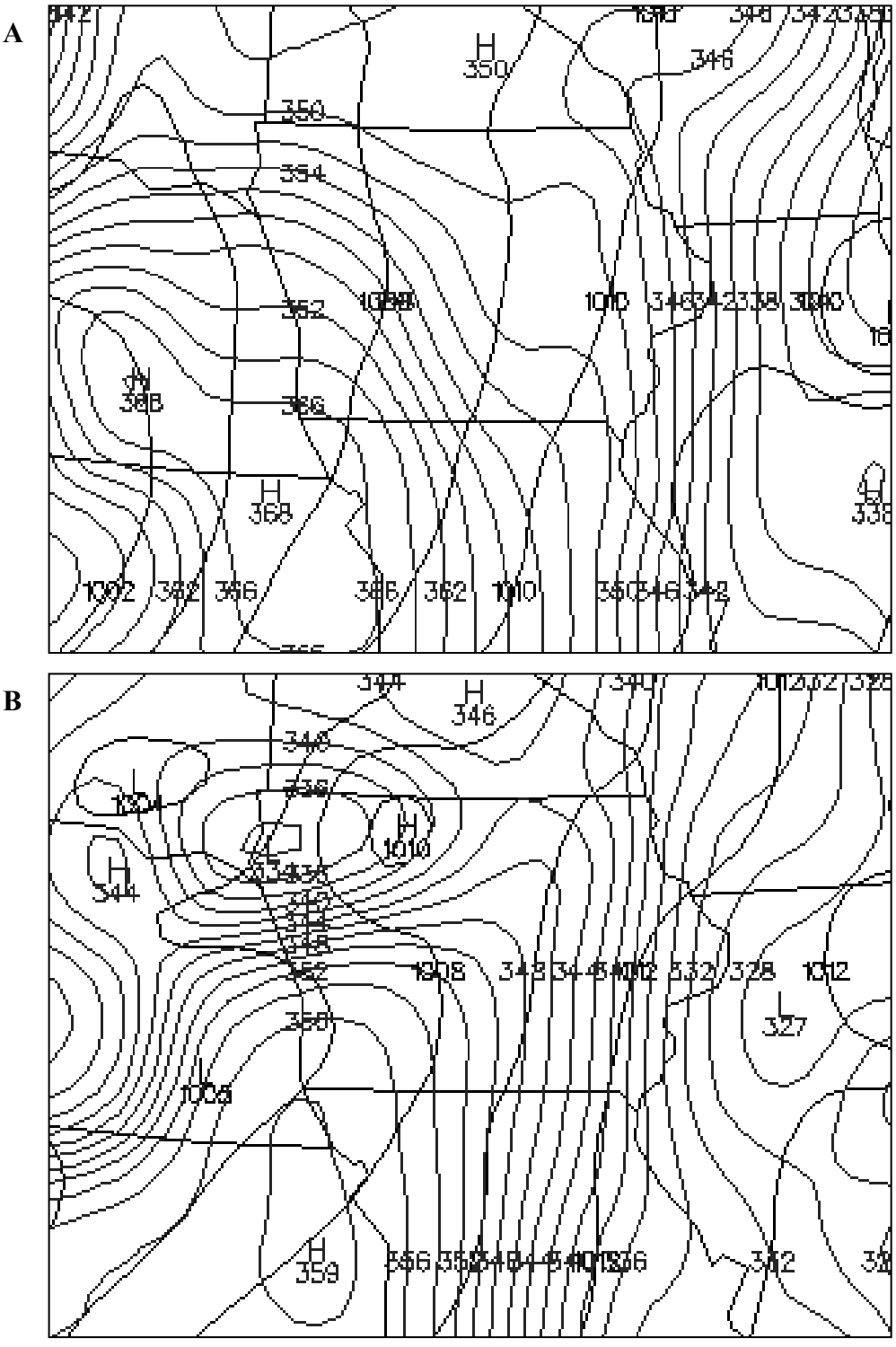

Figure 4.7: Contours of pressure (black) and equivalent potential temperature (gray) for the domain of interest. Intervals are 2 mb for pressure and 2 K for θ_e. The top panel (a) is and analysis at 0000 UTC, the bottom panel (b) is an analysis at 0600 UTC.

4.3 Special Soundings

For this case a total of 8 soundings were released by the two MGLASS units and MIPS. MGLASS1 was located 76 km west of the MIPS location, so for the remainder of this study the MGLASS1 soundings will serve as representative soundings of the pre-storm environment over the MIPS location. This assumption was validated using thermodynamic MPR soundings, Des Monies 88D Doppler radar, and wind profiles from the MIPS 915 MHz profiler. The time/space difference is approximately one hour of storm movement (50 km) between the MIPS and MGLASS1 location. However similar conditions persisted over both sites during this case study.

4.3.1 Composite Sounding

Figure 4.8 displays a skew-T plot from MGLASS1 at 0450 UTC. This sounding was launched about two hours before arrival of the MCS over the MIPS and one hour before passage over the MGLASS1 location. Because the MGLASS sounding terminated at 300 hPa, soundings from NWS sites in Aberdeen, SD Omaha, NE, as well as the 915 MHz profiler and the Slater, IA 404 MHz profiler were used to complete the sounding to 100 hPa. A shallow mixed layer extends from the surface to 925 hPa. Above this, a conditionally unstable layer is capped by a stable layer (inversion) centered near 810 hPa. Relatively dry air exists between 600 and 550 hPa. The MCS anvil cloud base is apparent near 400 hPa, and precipitation evaporation is suggested by the moist layer from anvil base to about 470 hPa. The surface-based LCL, it is located near 905 hPa, as annotated in the sounding. The LFC

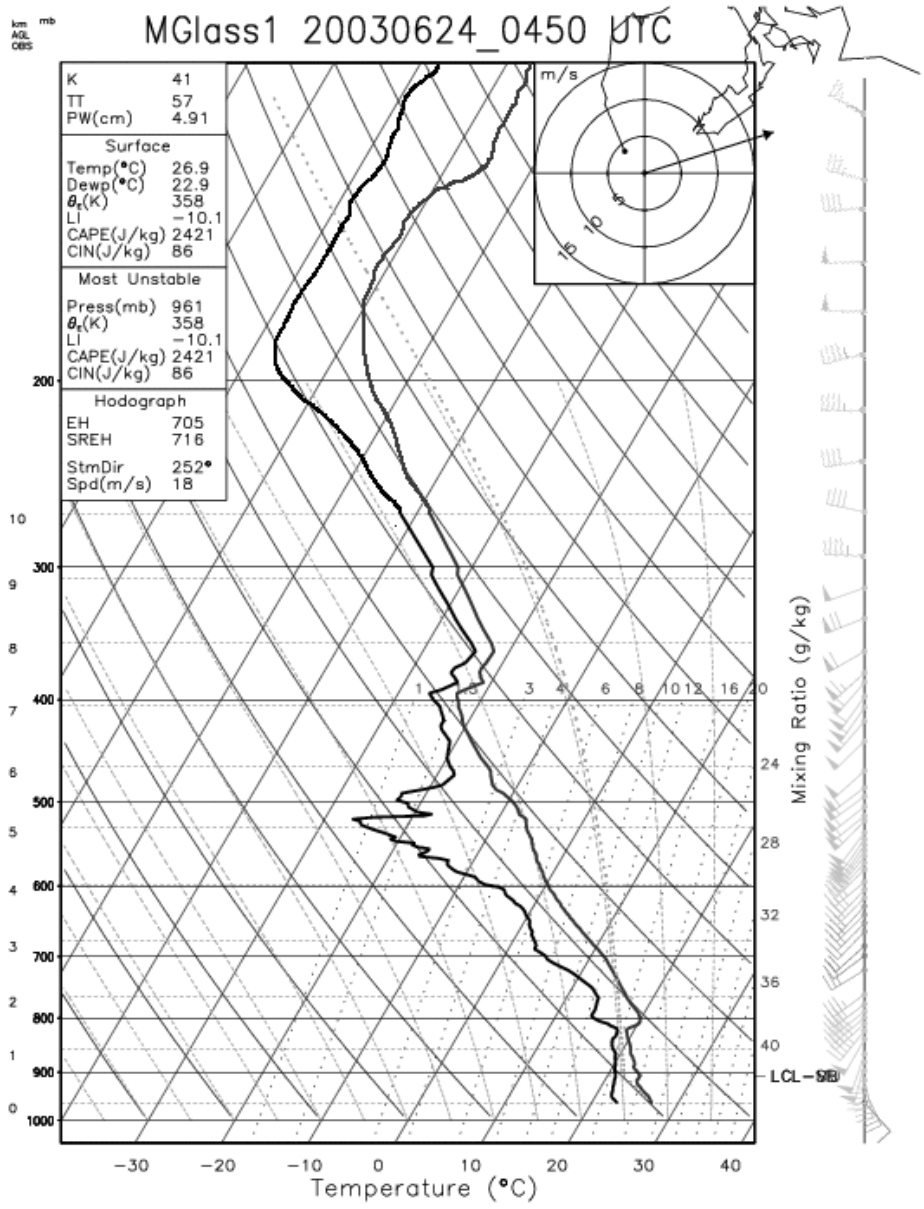

Figure 4.8 Skew-T sounding plot from the MGLASS 1 location at 0450 UTC on 24 June. This sounding was release 76 km from the MIPS location. The CAPE value was 2421 J kg-1, with a surface lifted index of -10.1, indicating an unstable air mass at this time.

is near 740 hPa, and it indicates that a parcel lifted from the surface would be negatively buoyant over the lowest 2.2 km AGL. The CAPE value from this composite sounding is 2421 J kg^{-1}, a value that matches with surrounding NWS soundings and the MIPS MPR. If anvil warming contamination was not present the CAPE value would be larger, in the range of 2800 – 3000 J kg^{-1}. In comparison Johns (1993) found that the average CAPE value for bow echo systems was about 4500 J kg^{-1}. In this case the CAPE value is appreciably less than the optimal 4500 J kg^{-1}. Many numerical simulations of bow echoes, such as Wesiman et al. (1992) and Przybylinski (1995) have used initial CAPE values near 2400 J kg^{-1}, much less than the optimal value of 4500 J kg^{-1} found by Johns (1993). The lifted index for a surface-based parcel is appreciable at about -10 °C. Veering and speed shear is most significant below the jet at 850-900 hPa (600-1000 m AGL). Middle tropospheric flow is more uniform southwesterly near 25-30 m s^{-1}.

4.4. MIPS 915 MHz Profiler Analysis

The inversion layer shown in the MGLASS1 sounding is also visible as enhanced return power (SNR) from the 915 MHz profiler, shown in time-height section format in Figure 4.9. At 0530 UTC, layers of enhanced SNR are located near 1.5 and 3.5 km. Enhanced uniform SNR over the lowest 1 km was produced by Rayleigh scatter from insects. The layer at 2.0 km corresponds to the inversion near 800 hPa (MGLASS1 sounding) and was produced by Bragg scatter. This layer moved upward to 2.5-3.0 km by 0540, suggesting that the environment changed rapidly in advance of the bow echo. By 0615 UTC, a deeper layer of enhanced SNR (indicative of shallow convective

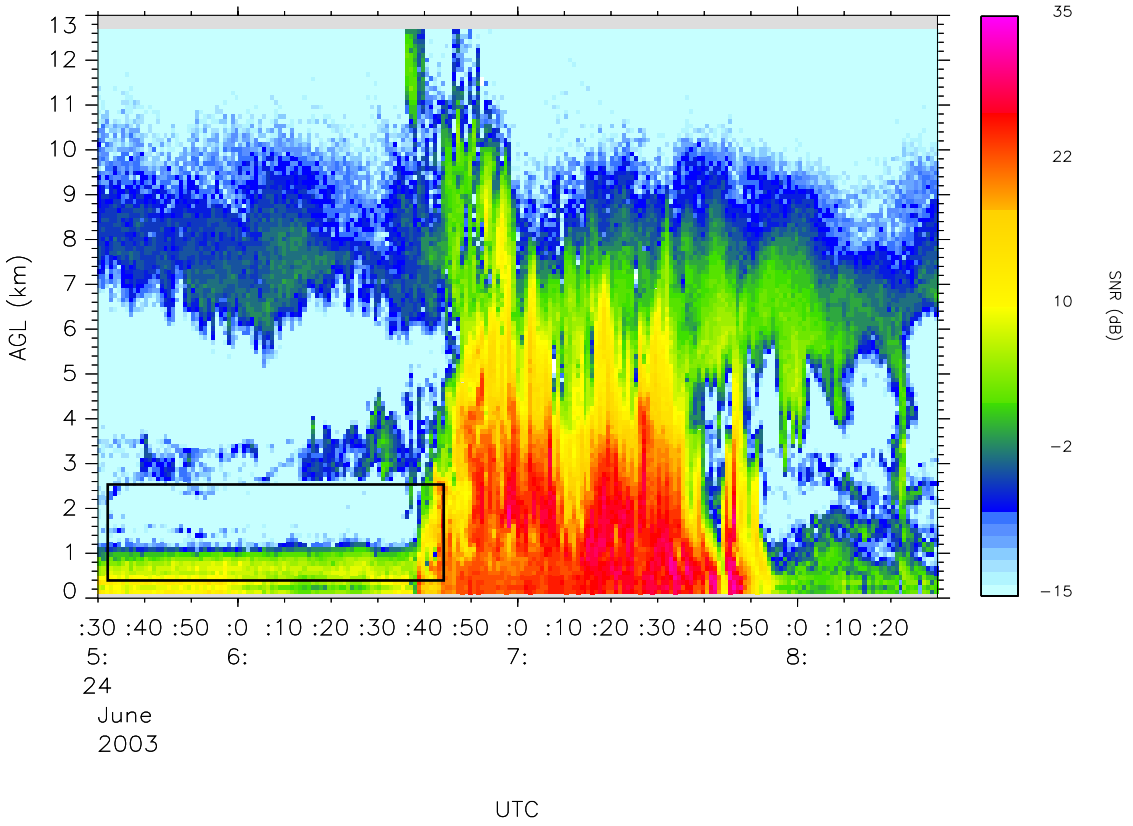

Figure 4.9 MIPS 915 MHz Profiler SNR time height series. Notice the inversion layer denoted in the square area. Between 0600 UTC and 0640 UTC this layer oscillated upward and downward. This layer is also visible in the MGLASS sounding.

structures) had developed within the 2.5-4.0 km layer, suggesting lifting and associated destabilization immediately in advance of the bow echo.

4.5 Slater, Iowa 404 MHz Profiler

The Slater 404 MHz Wind profiler is a relatively low-power, highly sensitive clear-air radar, which operates at a wavelength of 74 centimeters. The radar detects fluctuations in the atmospheric density (refractive index), caused by turbulent mixing of volumes of air with slightly different temperature and moisture content. The resulting fluctuations of the index of refraction are used as a tracer of the mean wind in the clear air. Although referred to as clear-air radars, this wind profiler is capable

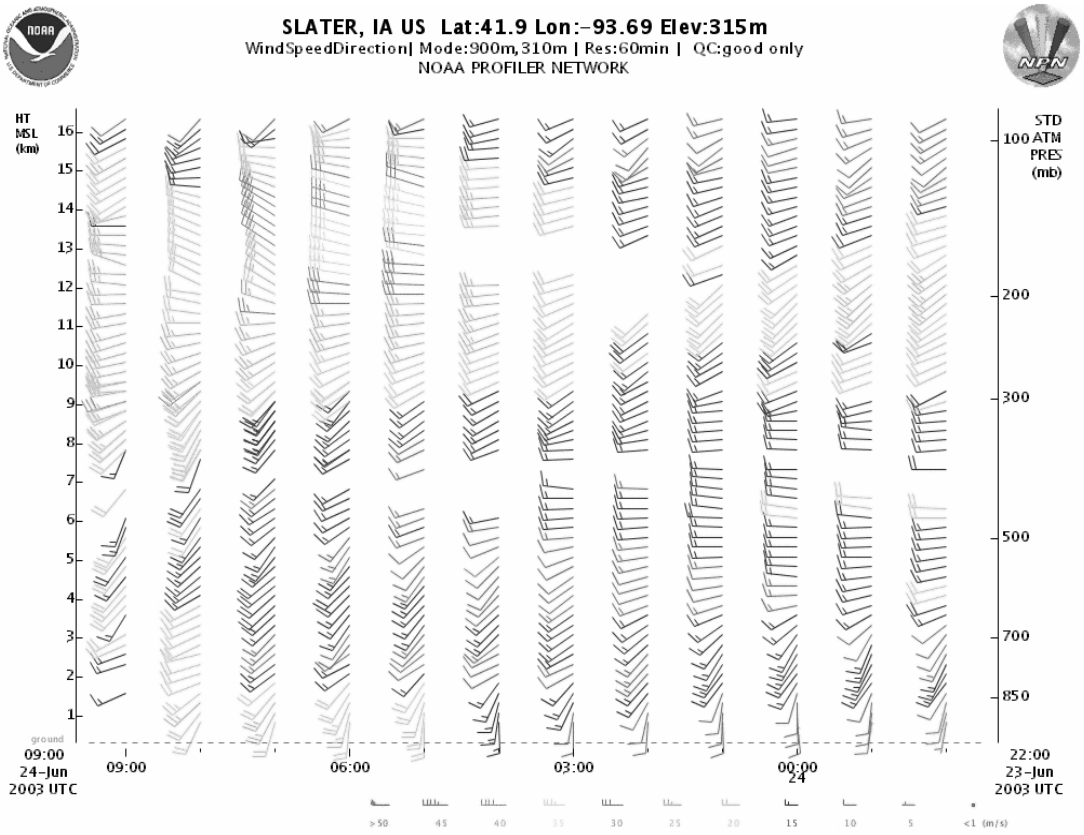

Figure 4.10 The Slater, IA 404 MHz Wind Profiler Plot. Time proceeds from right to left staring at 0000 UTC on 24 June and ending on 0900 UTC on 24 June. The profiler is located 86 km south of the MIPS location A full barb represents 10 m s^{-1}.

of operating in the presence of clouds and precipitation. The Slater Profiler is important to this study because the measurement height exceeds that of the MIPS 915 MHz profiler. The 404 MHz profilers can reach heights of 16.0 km in clear air, while the 915 MHz profiler can reach heights of 3.0 km in clear air mode. Figure 4.10 shows a time height series from the Slater 404 MHz profiler. Time increases from right to left. The plot start time is 0000 UTC on 24 June and end time is 0900 UTC on the same day. Features shown in the wind profile are similar to those from the MGLASS1 sounding. However, while the sounding is a one time measurement, the profiler shows the entire evolution of the wind field as the bow echo approached and passed the profiler site. Low level winds

(0.5 – 1.0 km) increased from 10-15 m s^{-1} at 0000 UTC to 20–30 m s^{-1} (similar to the MGLASS1 and MIPS 915 MHz wind profiles) as the bow echo approached the profiler site at 0700 UTC. There also is a slight veering of the wind over time starting at southerly, and ending southwesterly. Winds also increased with time in the upper levels as the MCS anvil influenced the profiler wind measurements.

Chapter V

THE PRE-STORM NOCTURNAL BOUNDARY LAYER

5.1 Nocturnal Boundary Layer (NBL) Properties

Detailed characteristics of the nocturnal boundary layer (NBL) have not been considered in previous studies of nocturnal squall lines, bow echoes, MCS's because of the difficulty in obtaining relevant measurements. However many studies, such as Johns and Hirt (1986), have analyzed both daytime and nighttime MCS and bow echo systems, but have made no distinction between how the NBL and CBL (convective boundary layer) affect these systems. The NBL has many different characteristics than the CBL, and must be considered. The 24 June case occurred during the late night hours well after the NBL had become established over the domain. Stull (1988) states that the NBL is difficult to describe and model, and that it is very complex in nature. There are many different types of NBL structures which make it difficult to classify what type occurs on any given night. For this case several parameters are analyzed to better understand the NBL and how it relates to bow echo development, growth, and decay.

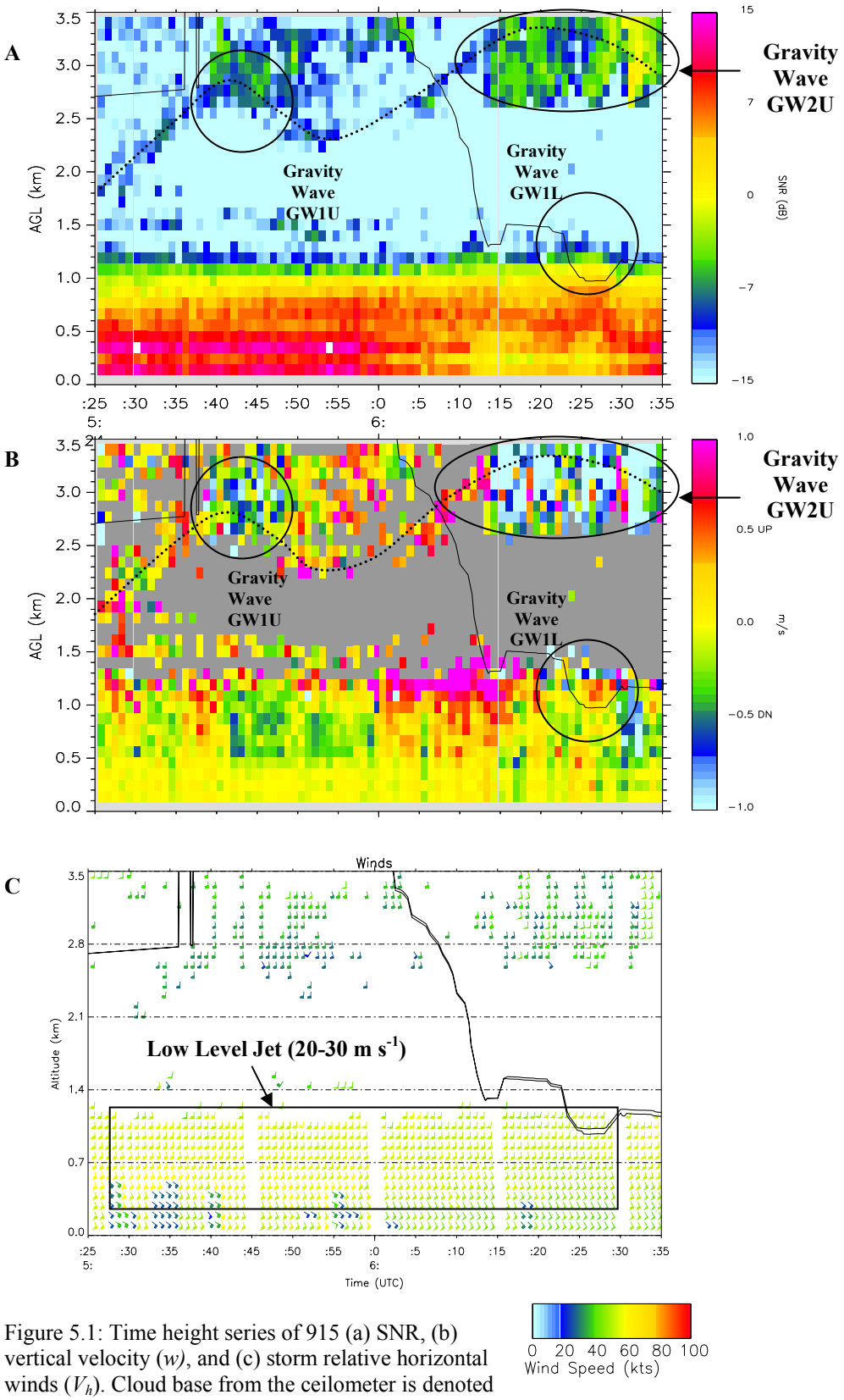

Figure 5.1: Time height series of 915 (a) SNR, (b) vertical velocity (*w)*, and (c) storm relative horizontal winds (V_h). Cloud base from the ceilometer is denoted by the solid line. The oscillating inversion layer is shown by the dashed line in each panel.

5.2 MIPS Measurements of Gravity Waves in the Pre-Storm NBL

An overview of the pre-storm low-level environment is presented in Figure 5.1 which displays a time series of 915 MHz SNR, W, and V_h from 0525 – 0635 UTC. The cloud base variation (solid line, determined by the ceilometer) is superimposed on each panel. The dashed in panels (a) and (b) denotes the top of the elevated inversion layer within 2 - 3 km AGL layer which exhibits two oscillations prior to the bow echo passage. Vertical motion values measured by the 915 are ±1.0 m s^{-1} near 1-2 km AGL in wave GW1L and around ±0.5 m s^{-1} within the 2.5 - 3.5 km layer for wave GW1U. Waves GW1U and GW1L produced surface pressure perturbations of 0.3 - 0.7 hPa, and 1.3 - 1.9 hPa, respectively (Figure 5.2). Other surface parameters did not vary during the passage of either wave. Another gravity wave (GW2U) is suggested near 3 km above GW1L, but its structure is masked by shallow convection that formed ahead of the line These waves are sustained by stable layers located at 900 and 820 mb according to the MGLASS sounding. Within wave GW1U, a period of downward motion (~ 1.0 m s^{-1}) between 0540 and 0600 UTC was followed by a 20 minute period of upward motion up to ~1.0 m s^{-1}.

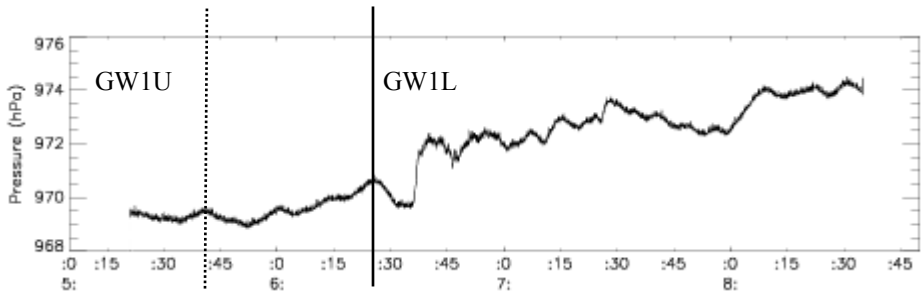

Figure 5.2: Pressure time series from the MIPS surface station. Gravity wave GW1U is denoted by the dashed line, while gravity wave GW1L is denoted by the solid line. There is also an increasing trend in the pressure in the time series.

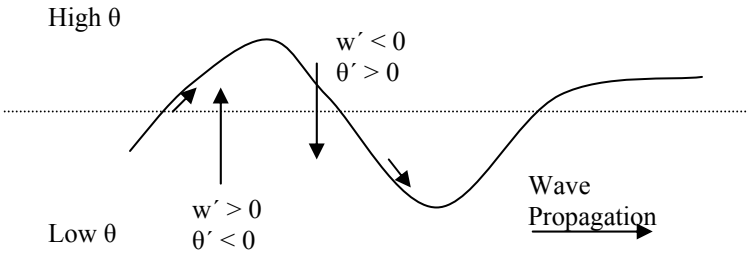

Figure 5.3 Schematic of gravity wave propagation effects on the inversion layer. Notice how the updraft and downdraft both yield negative values for the perturbation of heat flux.

In reference to the conceptual model in Fig. 5.3, a gravity wave propagating along an inversion layer would bring warmer air to upper levels ahead of it, followed by cooler dryer air behind it. Figure 5.4, taken from Fovell et al. (2005), shows a proposed mechanism for wave propagation. Panel (a) shows a typical squall line cross section with the storm relative air flowing up and over the cold pool. Panel (b) shows a shallow cloud deck formed by the low frequency gravity waves. Panels (c) and (d) show the high frequency waves that are trapped under the forward anvil. These waves trigger the formation of buoyant parcels, which in turn may develop into daughter clouds. This proposed mechanism is seen by the 915 profiler for this case (Figure 5.1a). GW2U is an excellent example of this mechanism. Several deep subsidence waves pass under the anvil during the time series, which allow the NBL depth to rise and fall, shown by the oscillation in the figure, as well as cloud development within the wave.

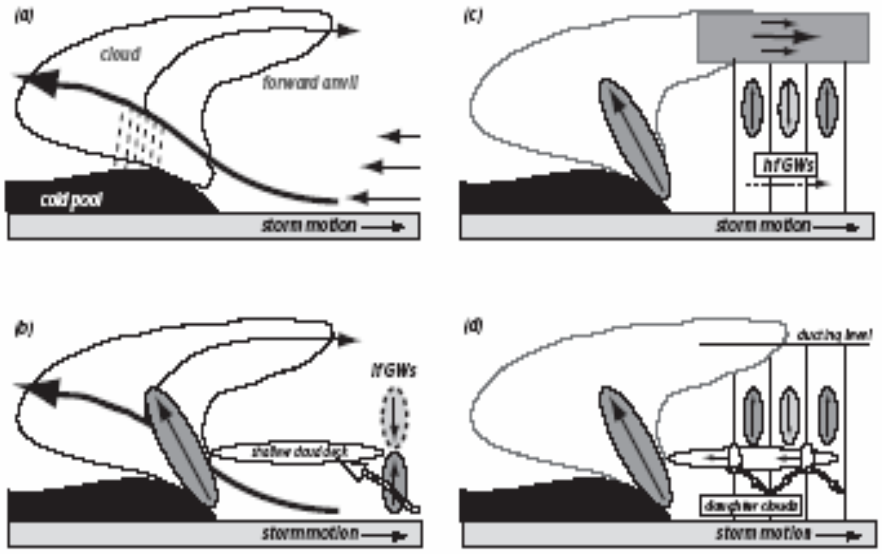

Figure 5.4: Proposed mechanism for discrete propagation. Shallow cloud deck in panel b depicts the moist tongue, panel d depicts the results of deep subsidence gravity wave propagation through the NBL (Fovell et al. 2005).

5.3 Mean Quantities

To better understand the NBL and its interaction with the bow echo, profiles of potential temperature (θ), mixing ratio (r_v), equivalent potential temperature (θ_e) and the u and v wind components are presented. These parameters were derived from 915 profiler and MPR data between 0530 and 0640 UTC, 24 June 2003. Vertical motion was estimated from the vertical beam measurement of radial velocity (W). However the other parameters cannot be found directly from measurements of the MPR and 915. In calculating these parameters, 21 levels were used from the surface to 3.5 km AGL. These levels, based on the height levels at which the MPR retrievals are done, were broken into the following heights: 0.1 spacing from the surface to 1 km, and 0.25 spacing from 1km to 3.5 km. Calculation of fluxes requires temporal matching of the 915 and MPR data. This was accomplished by averaging the 915 gates to match the MPR spacing, and then

averaging both data sets to the same time periods. The MPR and 915 sample times differed by only a few seconds at each data point. The dwell time for the 915 was 30 sec, while the retrieval time for the MPR was 1 minute. Time matching was achieved by averaging the 915 data over 1 minute intervals to match the retrieval time of the MPR. The lowest sampling level was somewhat problematic, as the first gate on the 915 is at .15 km, while the MPR first level is just above the surface. In the contour plots the data below .15 km was interpolated from the data above it. Vertical profile plots use data between .15 km and 3.5 km.

5.3.1 Potential Temperature

The potential temperature (θ) was determined from

$$\theta = T\left(\frac{p_0}{p}\right)^{R_d/cp}, \qquad (5.1)$$

where p_0 is 1000 mb, R_d is the gas constant for dry air, and c_p is the specific heat at constant pressure.

The temperature at each level was measured by the MPR with 1 minute resolution. The surface pressure was measured by the MPR, and the pressure at each level was determined hydrostatically using the formula

$$p_2 = p_1 * \exp^{(-g/r(Tv2+Tv1/2))*(z_2-z_1)}, \qquad (5.2)$$

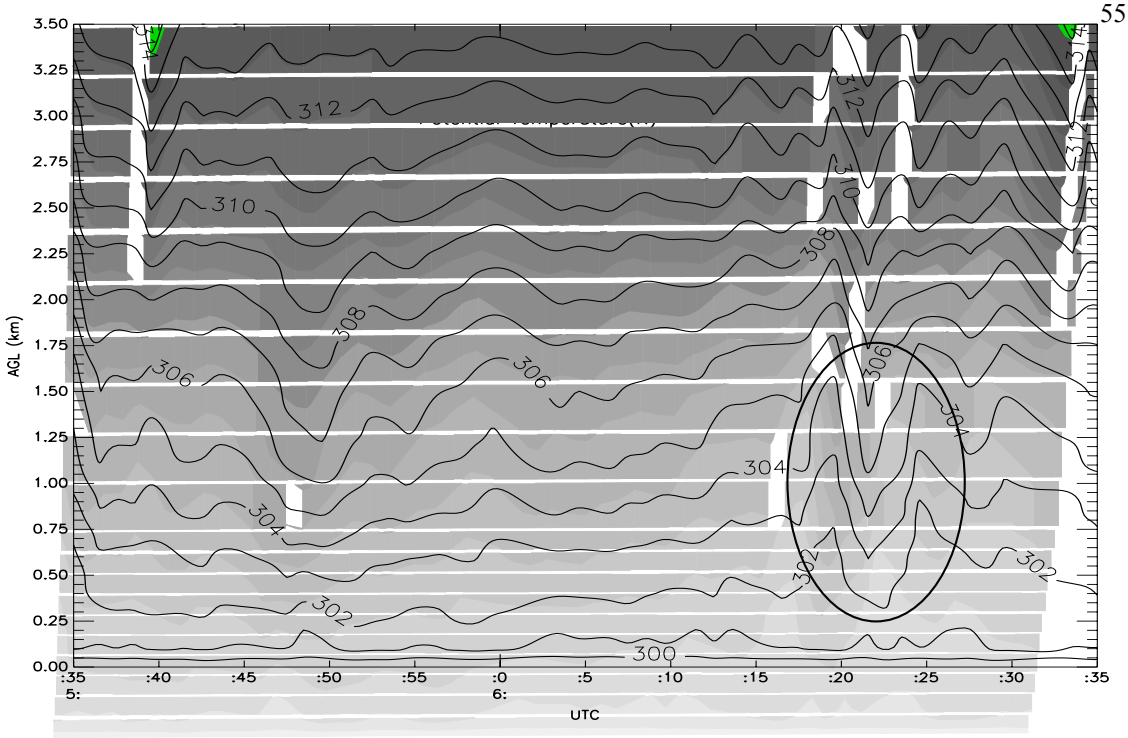

Figure 5.5: Potential Temperature (10 min average) contour from the MPR.
Gravity wave GW1L denoted by the circular area

where p_1 and p_2 are the lower and upper pressures at each level, T_{v1} and T_{v2} are the virtual temperatures at each level, and z_2 and z_1 are the height of each level.

Figure 5.5 shows a time-height section of θ from the surface to 3.5 km, where θ is plotted after applying a 10-minute running average. Large temperature fluctuations are analyzed near 0.9 km between 0625 and 0635 UTC. This feature is related to a gravity wave that was measured by the 915, ceilometer, and 88D radar (GW1L in Figure 5.1). Another weaker wave is also indicated at 0545 UTC propagating along the top of the inversion (3.0 km) (GW1U). The θ value near the surface remained nearly constant as the bow approached. However, in the remainder of the NBL θ increased with time starting at 0550 UTC until the arrival of the gust front at 0640 UTC (end of time series). The average increase is about 1.5 K within the 0 to 3.0 km AGL between 0600 UTC and 0635 UTC. Several θ oscillations

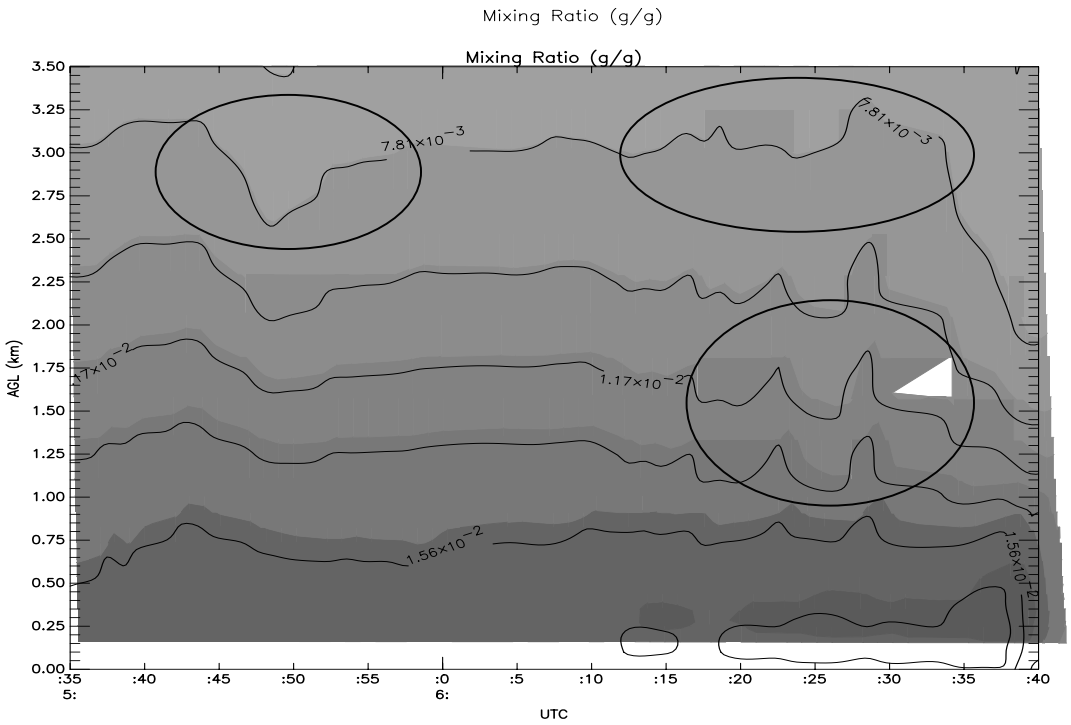

Figure 5.6 Mixing ratio calculated from the MPR. Data has been averaged over 10 minute periods. Gravity wave GW1L is denoted in the lower circular area. Waves GW1U and GW2U are denoted in the upper circular areas (From Figure 5.1)

between 2.0 and 3.5 km, are thought to be produced by waves (GW1U & GW2U) propagating within the inversion layer centered near 3.0 km.

5.3.2 Mixing Ratio

The MPR water vapor density (ρ_v) values are transformed vapor pressure (e) and then to mixing ratio (r_v) using the following formulas:

$$e = \rho_v R_v T \tag{5.3}$$

$$r_v = \varepsilon \frac{e}{p - e} \tag{5.4}$$

$$r_{v2} = \varepsilon \frac{(\rho_v * 461.5 * T_2)}{P_2} \tag{5.5}$$

where R_v is the gas constant for water vapor, T_2 is the temperature retrieved from the MPR, p_2 is the pressure calculated from Eq. 5.2, and $\varepsilon = .622$. The analysis in Figure 5.6, reveals that the mixing ratio changes little from the beginning to the end of the time series except for an important increase of about 2 kg kg^{-1} below about 0.5 km. Several oscillations are shown after 0610 UTC as the bow echo approached the MIPS. The gravity wave GW1L appears around 0623 UTC as a prominent oscillation in r_v. This result is consistent with the conceptual model of a wave transporting conserved variables (assuming no condensation) throughout the atmospheric column. This same signature is seen several times along the upper inversion layer.

5.3.3 Equivalent potential temperature (θ_e)

The value of θ_e was determined from

$$\theta_e = \theta \exp^{(2.675 r / T_L)}, \qquad (5.6)$$

where r is the mixing ratio determined by the MPR, θ is the potential temperature, and T_L is the temperature at the LCL. After finding each value at all points, θ_e was calculated. Figure 5.7 shows a time-height section of θ_e from the surface to 3.5 km. θ_e has been calculated over 10 minute running averages. Large fluctuations are analyzed near 0.9 km between 0625-0635 UTC. This feature is related to a gravity wave GW1L that was measured by the 915, ceilometer, and 88D radar. Another weaker wave (GW1U) was also analyzed at 0545 UTC propagating along the top of the inversion (3.0 km) layer measured by the 915. This wave had a weak flux in θ_e associated with its propagation along this layer.

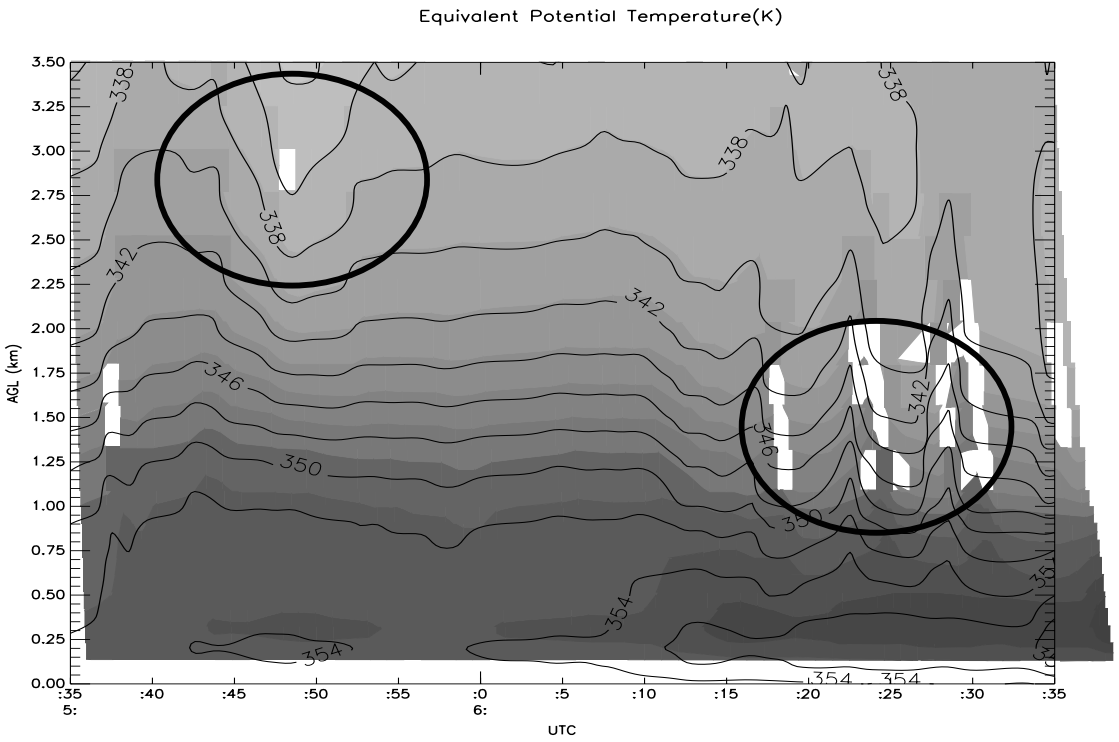

Figure 5.7 Equivalent potential temperature calculated over 10 minute intervals from the MPR. Note that gravity wave GW1U as well as GW1L have large spikes in θ_e.

Gravity wave GW2U had no associated fluctuation in θ_e. The lack of a fluctuation with this feature can be explained only by the wave being much smaller in size compared to the wave along the upper inversion layer. This wave was not able to pull a substantial amount of air upward or downward as it propagated along the NBL top.

5.3.4 NBL Height

The NBL height for this case is difficult to determine precisely, but it is an important parameter in regard to its interaction with the bow echo. That the inversion layer rose with time (Figure 5.1a) may be attributed to wave phenomena, such as bores, that would act to pull it upwards with time. This mean ascent caused the NBL depth to change over time. Mullendore (2005) stated that these low frequency gravity waves are convectively formed and travel in the lower troposphere, and follow high

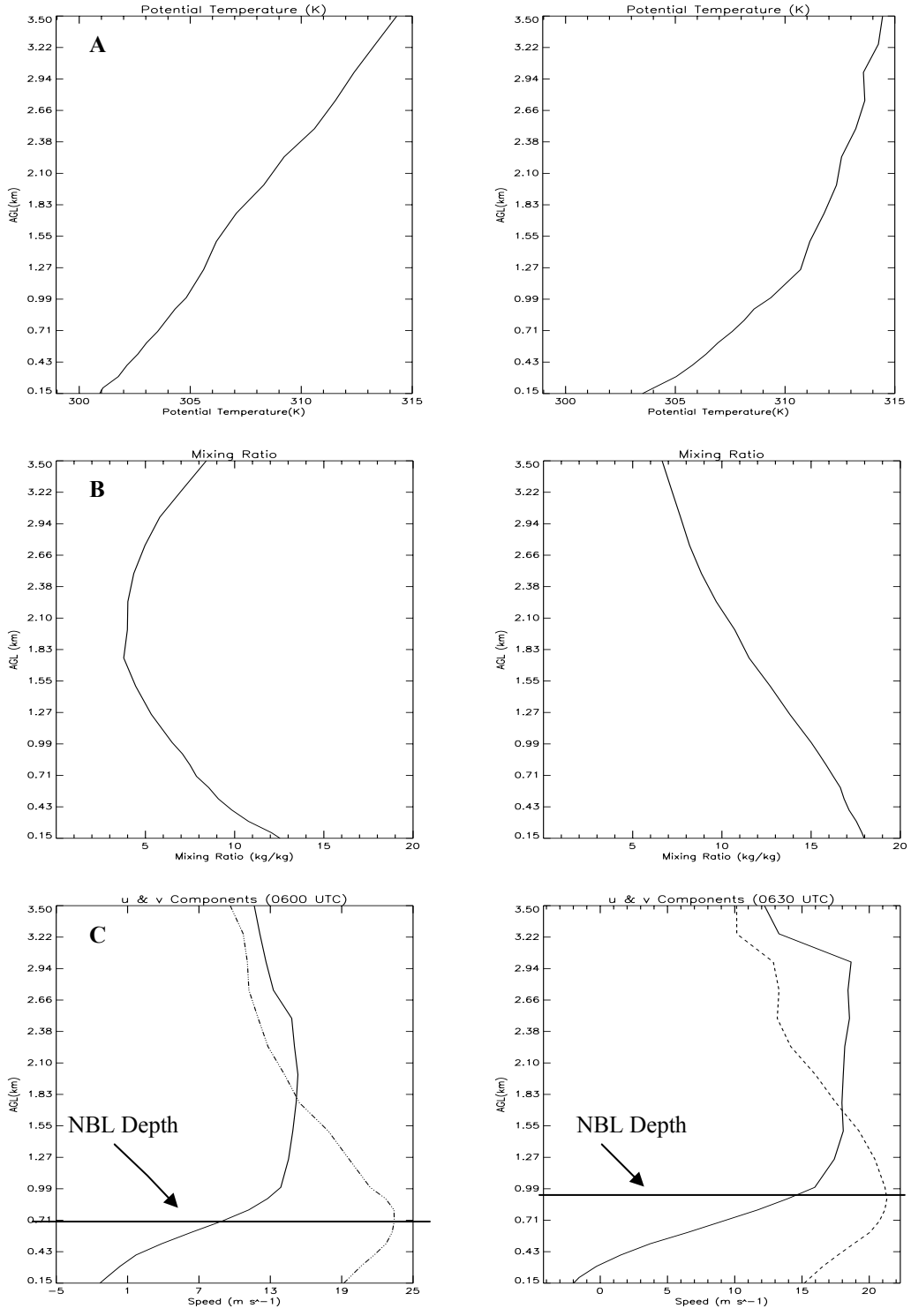

Figure 5.8 30 Minute vertical profiles of (a) θ, (b) r_v, and (c) u & v. The panels on the left are averaged from 0530 to 0600 UTC and the panels on the right are averaged from 0600 UTC to 0630 UTC. From these plots the NBL depth (h) appears to be near 700 m during the first period, and near 860 m during the second time period. The u component is dashed, v is solid.

frequency waves labeled troposphere deep subsidence waves. These waves allow for the air mass ahead of a given system to be more convectively favorable because of the cool moist tongue that is created by their passage. In this case wave GW1U and GW2U are good examples of deep subsidence waves, because of their long period, and GW1L is a good example of the lower tropospheric waves (short period). Figure 5.8 shows 30 minute averaged vertical profiles of θ, r_v, u, v for 0600 UTC and 0630 UTC. By analyzing these parameters the NBL depth can be approximated where these values go from a zero slope to a positive or negative slope. From these parameters it is clear that the NBL depth at 0600 UTC is approximately 700 m AGL. Stull also states that by analyzing the total wind speed, as well as the height of the jet one can define the NBL depth. This depth can be found by analyzing where the slope of the u & v components goes from positive to negative in nature. Analyzing the u component in Figure 5.5c it is clear that the NBL depth is near 700 m at 0600 UTC and moves to 860 m by 0630 UTC. This result is consistent with other parameters analyzed above.

Chapter VI

STORM SCALE ANALYSIS

6.1 Overview

To further the understanding of bow echoes the internal structure is analyzed using the MIPS and airborne Doppler radar data. On 24 June 2003 the MIPS acquired an excellent data set on a surging bow echo near the time of maximum radial velocity (exceeding 25 m s^{-1}) measured from the DMX WSR-88D. During the bow echo passage several updrafts on the order of 5 – 10 m s^{-1} as well as downdrafts on the order of 5 – 8 m s^{-1} accompanied the strong surface wind gusts. This chapter will examine each of the MIPS instruments as well as the ELDORA airborne Doppler radar to gain valuable insight into the internal structures and processes occurring within this bow echo system.

6.1.1 GOES Infrared Sequence

Figure 6.1 shows a series of GOES-12 infrared images (4 km resolution) from approximately the time of convective initiation until one hour after the passage of the system over the MIPS. The IR values range from 300 K (denoted by black and gray), to 200 K (denoted by white). Approximately five hours prior to the passage over the MIPS, the MCS formed over Nebraska and South Dakota. This is clearly shown at 0045 UTC

as a small cluster of cells forming over southern South Dakota and Northern Nebraska. During this period a west-east band of clouds covered most of central Iowa in advance of the MCS (Figure 6.1). Clear skies existed over northern IA and southern Minnesota, where surface air was drier and more stable. During the next hour the number of cells and the area had increased considerably. By 0245 UTC, when the MCS started to assume squall line properties, the cloud tops had cooled to minimum values of ~200 K over Nebraska. Intensification and expansion continued during the next two hours as the MCS moved into NW Iowa. Between 0445 and 0545 UTC the leading edge of the MCS assumed bow shape (Figure 6.2) at a location about 20 km west of the MIPS. As the bow echo passed over the MIPS around 0645 UTC, the coldest cloud tops of 240 K were recorded, and the strongest radial velocity values (40 m s^{-1}) were measured by the DMX radar. Finally, after the passage over the MIPS the cloud top temperatures increased as the MCS weakened. Around this time the cloud shield on the southern and southeastern edge lost definition. Cloud tops remained cold over Minnesota where deep convection persisted and moved eastward.

6.1.2 Des Moines WSR-88D

Figure 6.2 presents a sequence of radar reflectivity images from the DMX WSR-88D for a two hour period around the time of passage over the MIPS. This figure shows a gravity wave, the evolution of the bow echo prior to and after the arrival over the MIPS, and an outflow boundary that surged ahead of the southern portion of the MCS. During

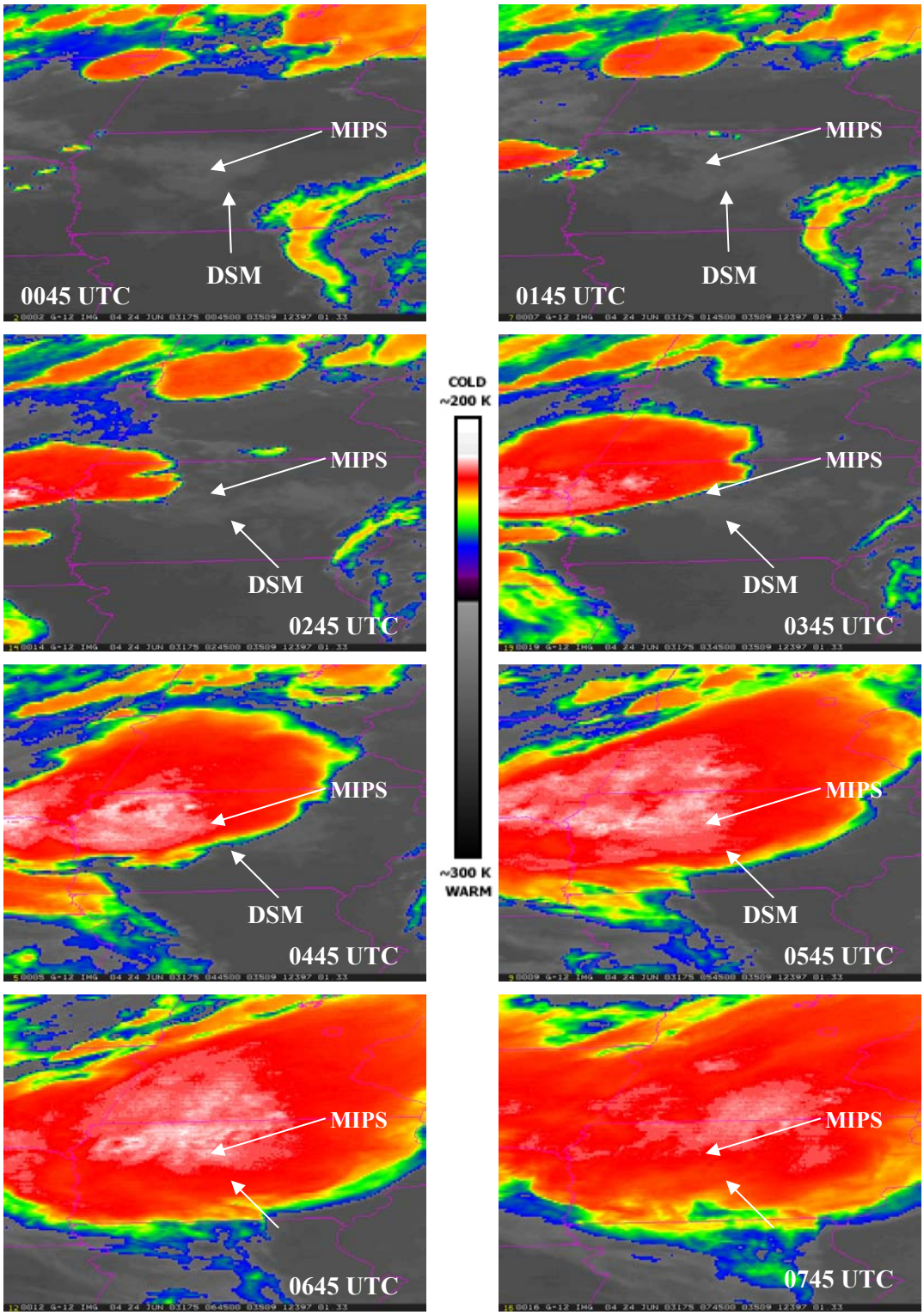

Figure 6.1 GOES-12 4-km resolution infrared images from 0045 – 0745 UTC. The locations of the cities of Fort Dodge, IA (FOD), and Des Moines, IA (DSM), as well as the MIPS location have been superimposed. Starting from the top right the cells initiate over South Dakota and mature as they move to the south and east over across Iowa. The coldest cloud tops pass over the MIPS location between 0545 and 0745 UTC.

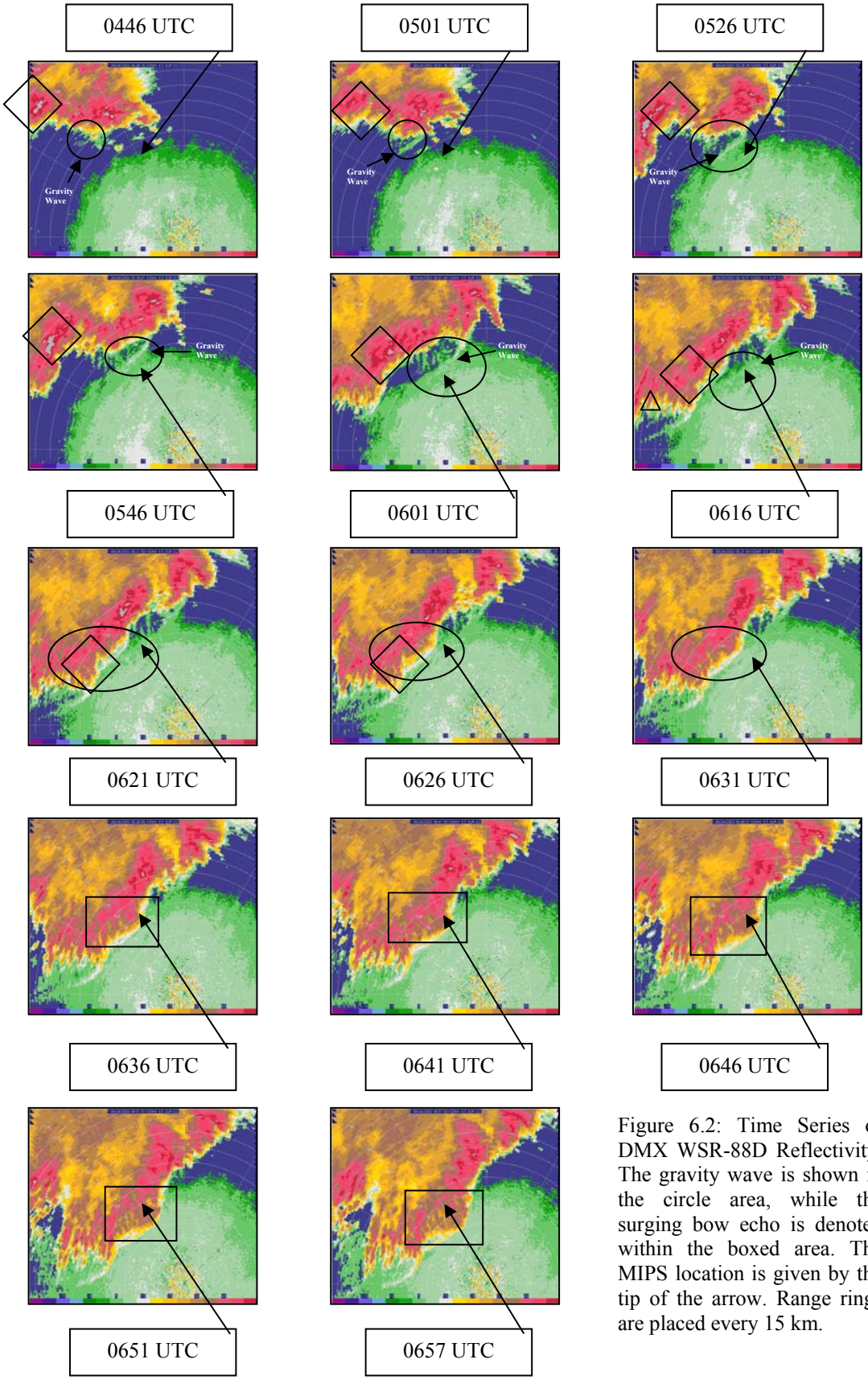

Figure 6.2: Time Series of DMX WSR-88D Reflectivity. The gravity wave is shown in the circle area, while the surging bow echo is denoted within the boxed area. The MIPS location is given by the tip of the arrow. Range rings are placed every 15 km.

this period, the mesoscale organization of the MCS changed significantly from an orientation of west to east at 0446 UTC (in line with the previous east-west band of stratocumulus clouds), to southwest to northeast by 0646 UTC. The initial bulge in the bow echo appeared around 0616 UTC and became prominent by 0641 UTC, near the time of passage over the MIPS. At 0446 UTC a fine line (identified as gravity wave GW1L) emerged from the southern portion of the leading west-east squall line. This gravity wave is denoted in the circular area. As the gravity wave moved away from the MCS it dissipated and was no longer measurable at 0630 UTC. At 0621 a gust front emerged from the leading edge of precipitation, and accelerated ahead of the system. The gust front was sampled by the MIPS 17 min later at 0638, and is marked by a fine line in the 915 SNR (Figure 5.13), and a narrow updraft in the 915 W field. As the MCS neared the MIPS location the leading edge formed a bow echo whose apex passed close to the MIPS location. During this transition (~ 20 minutes), approaching radial velocity magnitudes measured by the DMX radar approached 40 m s^{-1}, the highest values measured during the bow echo passage. This bow formation is shown in the boxed area in Figure 6.2. Soon after the passage over the MIPS the MCS weakened and by 0800 UTC only a few isolated cells remain. However, the gust front continued to initiate small cells as it moved towards the southeast.

As this gust front advanced to the east a series of waves aligned south-north formed in the wake of the gust front. These waves appear to propagate from south to north, and not west to east as the gust front does over the time period from 0546 to 0657. The interpretation of this is that these waves were produced by the deep convection and were then ducted by the strong inversion at the top of the cold air.

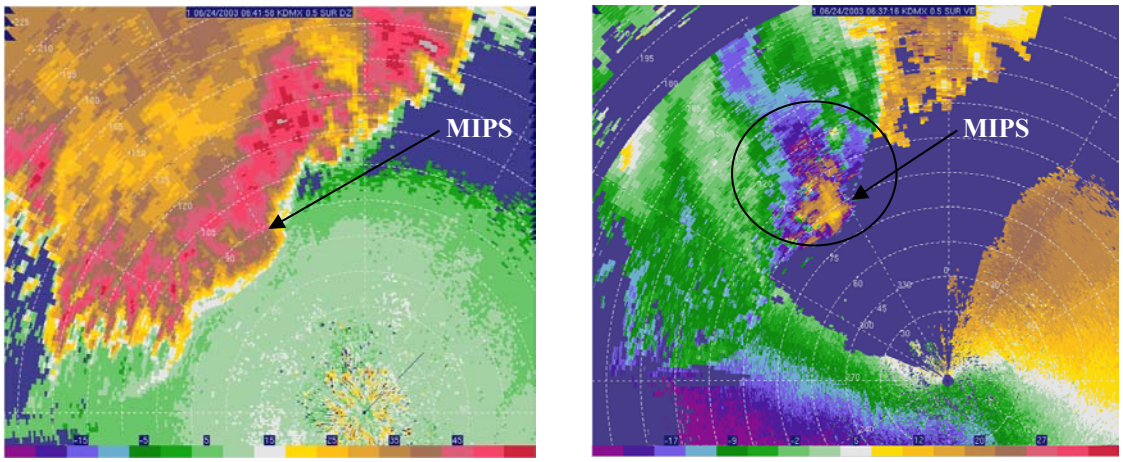

Figure 6.3: 0640 UTC Z and V_r from the Des Moines WSR-88D radar during maximum reflectivity and velocity over the MIPS location. Max velocity is approximately 36 m s^{-1} at the 0.5˚ elevation.

The formation of the bow echo appears to be related to the eastward propagation of an intense convective feature that was present along the western domain of Figure 6.2a. At 0445 UTC the squall line was forming from several cells that were beginning to evolve into a squall line over the domain. As this evolution was occurring, a strong cell to the rear of the system (identify by the diamond in Figure 6.2) propagated at a higher rate (25 m s^{-1}) the overall line. As this cell approached the leading edge of the MCS the bow echo surged towards the east and the maximum Vr values were recorded. This convective impulse that propagated through the system may have been a large amplitude gravity wave produced by intense convection that encountered the stable outflow.

Figure 6.3 shows the distribution of Z and V_r near the time of maximum Vr over the MIPS at 0.5˚ elevation angle. The area of strong wind (900 km^2) is small compared to the area of the MCS. Details of the airflow around this time are provided by the analysis of the ELDORA Doppler radar data, presented in Section 6.2.

6.1.3 MIPS Surface Station Time Series

Figure 6.4 shows a time series of the surface parameters measured by the MIPS. The solid and dashed lines indicate the passage times of the gravity wave and gust front respectively. The gust front was accompanied by sudden drops in both temperature and dewpoint, large changes in wind speed and direction, and a rapid increase (2 hPa) in pressure. The minimum in both T and T_d at 0710 UTC marks the core of the MCS cold pool. The wind speed (panel b) decreased 30 minutes prior to the gust front passage and was near a minimum value at the time of the gravity wave passage. The peak wind gust of 24 m s^{-1} was recorded eight minutes (5 km) after the gust front passage at 0646 UTC. Other distinct wind gusts at 0659 (16 m s^{-1}) and 0707 (13 m s^{-1}) correspond to downdrafts inferred from by the 915 Profiler at 0659 and 0707 UTC. Gravity waves within the cold outflow air are marked by pressure oscillations (Figure 6.4d), and in some cases wind shifts at 0800 and 0830 UTC. These waves correspond to the Z features measured by the DMX radar. Accumulated total precipitation (Figure 6.4e) totaled to only 13 mm over a one-hour period. The peak rainfall rain rate reached 44 mm hr^{-1} at the leading edge, and tapered to lower values after 0700 due to an absence of stratiform precipitation.

6.2 Kinematics Determined From Airborne Doppler - ELDORA Analysis

From 0200 UTC until 0923 UTC the NRL P-3 flew several short legs along the leading edge of the MCS. For this case study three legs around the time of passage over the MIPS location were analyzed. These legs are shown in Figure 3.3, and occurred between 0620-0626 UTC, 0630-0636 UTC, and 0646-0652 UTC. The respective analysis times are near the mid-point of each time interval: 0623, 0633, and 0650 UTC.

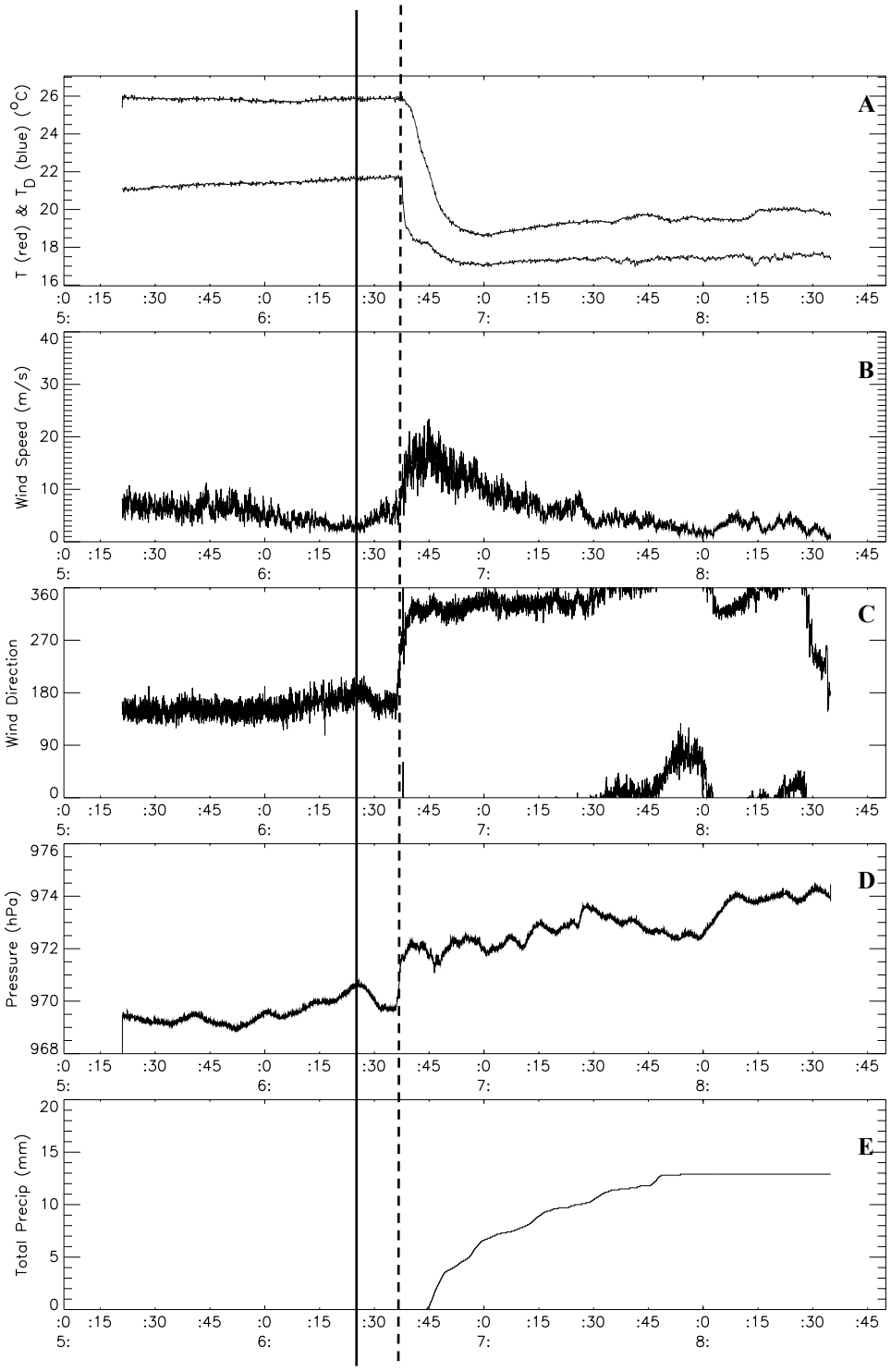

Figure 6.4: MIPS surface station plot. Data was recorded during 1-sec intervals, and has been quality controlled. The panels above are the time series plots for the following parameters (a) Temperature (˚C) & Dewpoint, (b) wind speed (m s^{-1}), (c) Wind Direction, (d) Pressure (hPa), and (e) total precipitation (mm).

For each leg a dual Doppler output was examined at 1, 5, and 10 km AGL. In addition to horizontal sections, vertical sections were examined over the MIPS location for all three legs. In all figures the MIPS is located at the origin (0, 0) in the Cartesian coordinate system.

6.2.1 Leg 1 (0620-0626 UTC)

During the initial leg the leading edge of the MCS was located 15 km west of the MIPS location. During this period the MCS was continuing to mature, but had not begun to show signs of an emerging apex near the MIPS system. However, there was evidence of a bow signature appearing 15 km to the southwest shown by the 1 and 10 km vertical sections in Figure 6.5. Figure 6.5 shows horizontal sections of Z at 1 km, 5km, and 10 km from the ELDORA fore radar, with the storm relative dual Doppler winds (V_h, m s^{-1}) overlaid. For each level the Z and velocity data (V_r, m s^{-1}) are contoured. During this period the convective line was propagating from 308° at 16.7 m s^{-1} determined from the Des Moines 88D radar. The reference time used to complete the synthesis was 0623 UTC determined by the midpoint of this individual leg. The leading edge of the MCS had produced wind damage across northwestern Iowa prior to this time, but no reports were recorded from 20 minutes prior to this leg to the conclusion of this event in Iowa. Figure 6.5a shows that the MCS at this time had a peak reflectivity value of 49 dBZ at 1 km, and a peak storm relative velocity value of 34 m s^{-1} (at 1 km).

During this period the convective line was approximately 10-15 km wide at Z=1km. Individual cells riding along the line produced higher values of both reflectivity and velocity values. V_r values ranged from <-35 m s^{-1} on the southern end of the domain, to

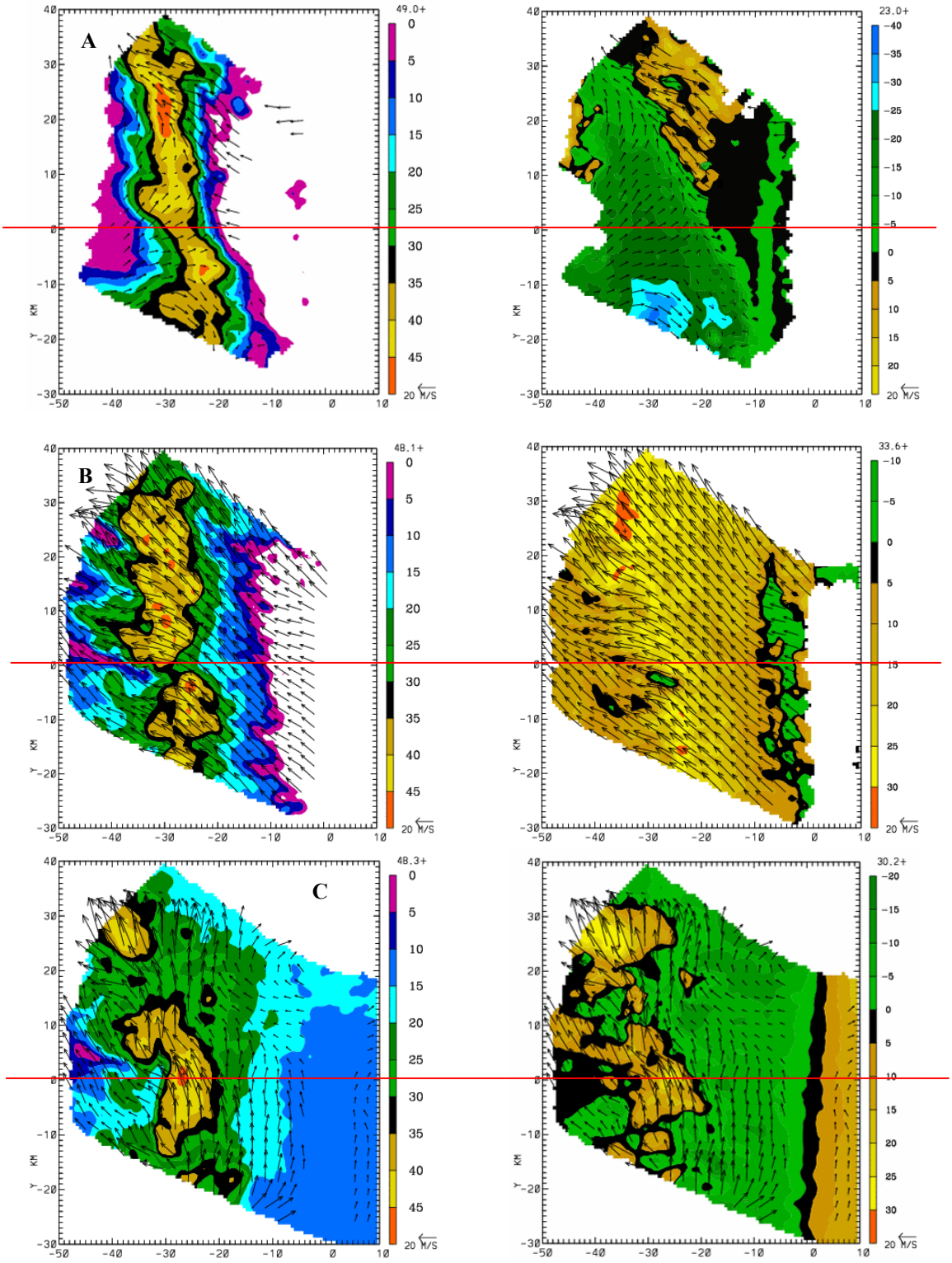

Figure 6.5: Eldora reflectivity and velocity scans for leg 1 over the MIPS system. Dual Doppler storm relative winds have been overlaid and are in units of m s^{-1}. (a) Z= 1 km, (b) Z = 5 km, and (c) Z = 10 km (AGL). Peak reflectivity at this time is 49 dBZ at 1km, and peak velocity values are 34 m s^{-1} at 5 km. The red line denotes vertical cross section.

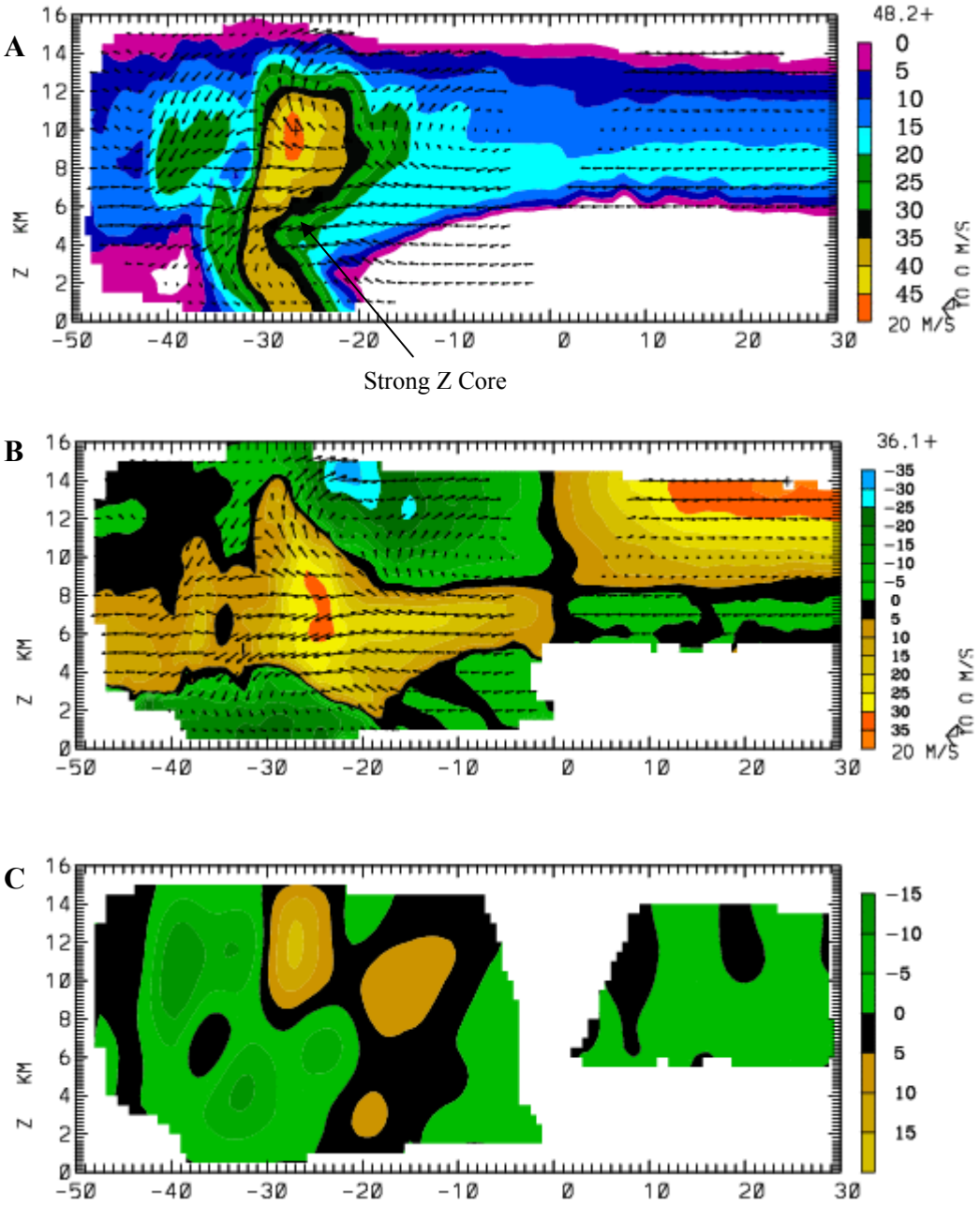

Figure 6.6: Vertical cross section from leg 1 of velocity data from the Eldora fore radar. The MIPS is located at the 0 point on the x-axis. (a) reflectivity (z), (b) Velocity (V_r), and (c) Vertical motion (w, m s^{-1}) . Dual Doppler winds (V_h) are overlaid in units of m s^{-1}. Axis units are in km.

-20 m s^{-1} on the northern end. Across the center of the domain values were near -5 to -10 m s^{-1}. Storm relative winds (V_h) show that the flow was front-to-rear (easterly) on the northern side with values of 20 m s^{-1}, while on the southern end horizontal winds were rear-to-front (westerly) with values approaching 15 m s^{-1}. Reflectivity values were approximately 10 dB higher on the northern end compared to the center of the line, and 15-20 dB higher when compared to the southern end where velocities were dominated by outbound motions. At 5 km and 10 km AGL, the V_h values increase and become dominated by southeasterly front to rear flow at 5 km. At 10 km the relative flow is weaker and primarily divergent, especially around convective cores. The strongest cell at this level was located near (-27, 0). In these areas values tend to be higher and motions tend to be into the system. The relative horizontal flow is stronger at 5 km with values nearing 30 m s^{-1} from 120° across the entire line. Airflow is more variable around active deep convection. At 10 km the relative flow is southerly and stronger with values near 5 m s^{-1}, with the convective regions being much higher in magnitude.

Figure 6.6 shows vertical cross sections of (a) Z, (b) V_r, and (c) vertical motion (w) for leg 1 over the MIPS. In panels (a) and (b) the dual Doppler storm relative winds (V_h) are overlaid. The cross section is taken east to west over the MIPS location at x = 0. This cross section location is denoted by the red line in the horizontal planes in Figure 6.5.

Relatively large values of Z extend from the surface to 10 km, with a peak intensity of 48 dBZ at 11 km. A low-level updraft is located near x = -22 along the leading edge of the system. This updraft exhibits maximum of 16 m s-1 near 12 km AGL. Figure 6.6 a shows storm-relative front-to-rear flow over a deep layer from 2 to 8 km AGL. A portion of this flow appears to feed a downdraft of 5-10 m s-1 whose top is

near 4 km along the upshear flank of the reflectivity core. This downdraft is likely associated with strong surface winds measured 15 minutes later by the MIPS. The MIPS was sampling the anvil at high levels and the low level jet at low levels (Figure 6.9 & 6.11) at this time. Reflectivity values of 15-20 dBZ within the anvil were similar in both instruments. Strong relative flow into the bow echo reflectivity core approaches values of 36 m s^{-1}. Values were also high throughout the core from just above the surface to 12 km.

Relatively weak storm-relative flow is present near x = -20, suggesting that the outflow surge was in an early stage of development. However, to the south of this cross section an apex had formed (Fig. 6.5a) is association with strong outflow (rear to front) measured by the ELDORA and the WSR-88D radars. There is also a maximum centered at x = -30 which was elevated from the surface.

6.2.2 Leg 2 (0630-0636 UTC)

During the second leg several other maneuvers were performed to avoid turbulent and convective areas. Because of this curved flight track horizontal resolution in the dual Doppler winds was degraded and required interpolation to fill large holes in the derived wind field. For this leg the advection value used was 304˚ at 17.6 m s^{-1}, and the reference time used was 0633 UTC. After plotting and analyzing the data it was decided to limit the area of interpolation and to leave the larger holes as is so that the errors would not be great in number.

Referring back to the WSR-88D time series (Figure 6.2) there now is a surging portion of the line, and an apex has formed just to the south and west of the MIPS

location. Reflectivity factor values have decreased to about 40 dBZ, about 10 dB less than 10 minutes previous. The MIPS is now closer to the leading edge of the MCS and is sampling shallow convection just ahead of the system. A gust front is surging ahead of the main bow echo core which is beginning to disrupt the flow into the core of the system, leading to a decrease in intensity of the bow echo.

A well-defined bow echo with an apex 10 km south of the MIPS location is shown in Figure 6.7. A large area of ground-relative outflow speeds between 25 and 35 m s-1 is shown. Reflectivity values in this area decreased rapidly as the apex accelerated ahead of the main convective line. V_h at this level (Figure 6.7a) was southeasterly ahead of the line, and westerly within the system, with values ranging from 5-15 m s^{-1}. A rear inflow notch was located within the southern portion of the strong westerly outflow near y = -15. Within this core of the bow echo the ground relative horizontal wind field was strongest, at about 45 m s^{-1} towards the aircraft (westerly). At this time the gust front was located 15 km to the west of the MIPS and was well-marked by a wind shift and convergence line (denoted within the circular area). The strongest westerly outflow is about 20 km west of the gust front.

At 5 km the system had a different structure, with the velocity data showing that the system was dominated by outbound motions approaching 25 m s^{-1} in the northern portion of the line The storm-relative horizontal wind field remained strong at this level with values approaching 35 m s^{-1} from the southeast in the northern portion, and 20-30 m s^{-1} near the apex located close to (x,y = (-10,-15). Z values within the bow echo decreased appreciably from values observed 10 min earlier.

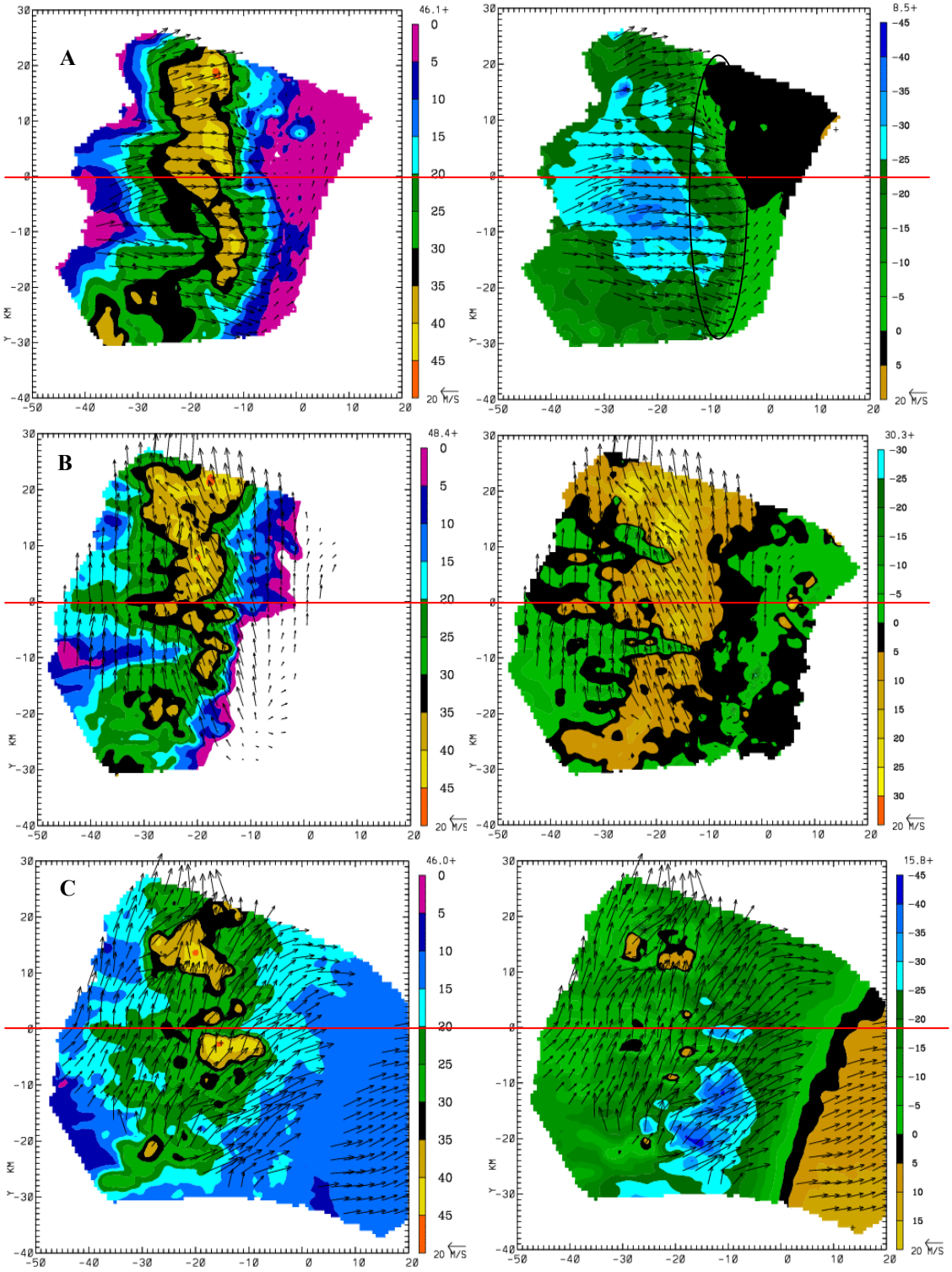

Figure 6.7: Eldora reflectivity and velocity scans for leg2 over the MIPS system. Dual doppler storm relative winds have been overlaid and are in units of m s^{-1}. (a) Z= 1 km, (b) Z = 5 km, and (c) Z = 10 km (AGL). Peak reflectivity at this time is 48 dBZ at 1km, and peak velocity values are -45 m s^{-1} at 1 km.

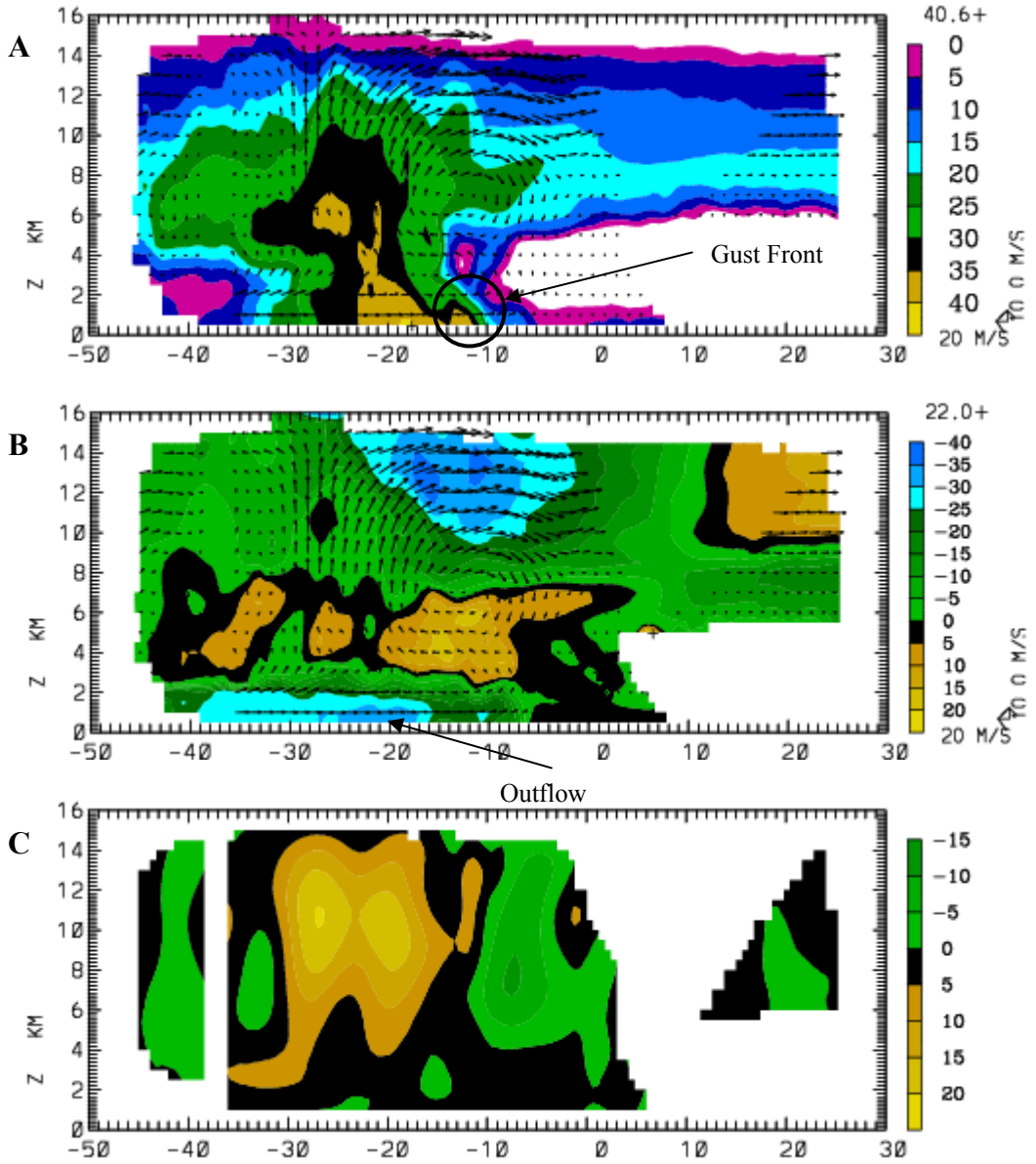

Figure 6.8: Vertical cross section from leg 2 of velocity data from the Eldora fore radar. The MIPS is located at the 0 point on the x-axis. (a) reflectivity (z), (b) Velocity (V_r), and (c) Vertical motion (w, m s^{-1}) . Dual doppler winds (V_h) are overlaid in units of m s^{-1}. Axis units are in km.

At 10 km the bow echo exhibits greater uniformity in Z and horizontal flow of about -20 m s^{-1}, from the south to southwest. However, the winds were slightly higher over the northern portions of the line where deep convection was more vigorous. Reflectivity values at 10 km were low compared to the previous leg, showing the system was beginning to decay from the earlier leg analyzed. The highest reflectivity value recorded was 37 dBZ over the northern cells along the convective line.

Figure 6.8 shows the vertical cross sections of (a) Z, (b) V_r, and (c) vertical motion (w) for leg 2. The dual Doppler winds show that the main updraft has been cut off from its surface feed as the gust front raced away from the core. The anvil winds have decreased slightly in both the 915 and ELDORA analysis. Closer inspection of Figure 6.8c reveals a that w has increased in strength and coverage, even though the main core has lost intensity and definition

From Figure 6.8 there are several key factors to mention; (a) At this time a distinct gust front has begun to surge ahead of the low-level Z core (denoted by the gust front arrow in figure 6.8a). (b) 10 km south of the MIPS location there were stronger winds, a more distinct and intense gust front is located at the apex of the bow, (c) the main updraft above the Z core is about 15 km wide (east-west) and exists at levels above 4-6 km. Peak values are about 20 m s^{-1}. (d) the low-level downdraft present 10 minutes earlier is very weak (0-5 m s^{-1}) and centered on the upshear side of the low-level Z core. Strongest outflow winds (approaching $V_r > 25$ m s^{-1}) are below and just to the west of the Z core. This is labeled as outflow in figure 6.8b. (e) a shallow low-level updraft accompanies the gust front. (f) peak Z is about 40 dBZ at the lowest level (1 km).

6.2.3 Leg 3 (0646 – 0652 UTC)

The final leg occurred while the bow echo was in the decaying stage. The 16 minute gap between leg 2 and 3 is due to the fact that the NRL-P3 flew 4.5 km further to the south of the domain of interest. For this leg the advection value used was 300˚ at 18.6 m s^{-1}, and the reference time used was 0650 UTC. Figure 6.6 shows reflectivity and velocity data for this leg at 1, 5, and 10 km.

Lower values of Z and Vr at 1 km substantiate a decline in intensity of the bow echo. The highest value of reflectivity at 1 km AGL is 47 dBZ in a small cell on the northern-most portion of the line, where weakening was less substantial In section 6.1.2 it was stated that the northern portion of the MCS continued to grow and mature as it progressed into Minnesota and extreme northern Iowa. This cell represented the southern extent of that stronger portion of the line. Removing that cell from the analysis which the highest reflectivity value at approximately 40 dBZ at 1 km. This portion of the line was the remnant of the surging apex that passed over the MIPS. At this time the system was still surging and producing V_r values less than 30 m s^{-1} around the MIPS. The horizontal wind field is primarily westerly at 15 – 20 m s^{-1}, with some variations around individual cells. The rear inflow has been cut off, and is no longer visible in the velocity, reflectivity or profiler data.

At 5 km Z values within the bow are more uniform in nature. The storm relative flow is also relatively uniform from the southeast at around 30 m s^{-1} as in earlier times. At 10 km a Z core is located 6 km north of the MIPS with and associated divergent flow. The northern portion had some higher reflectivity values, but at this time the intensity of all deep convection had decreased. Compared to earlier times the wind field was uniform

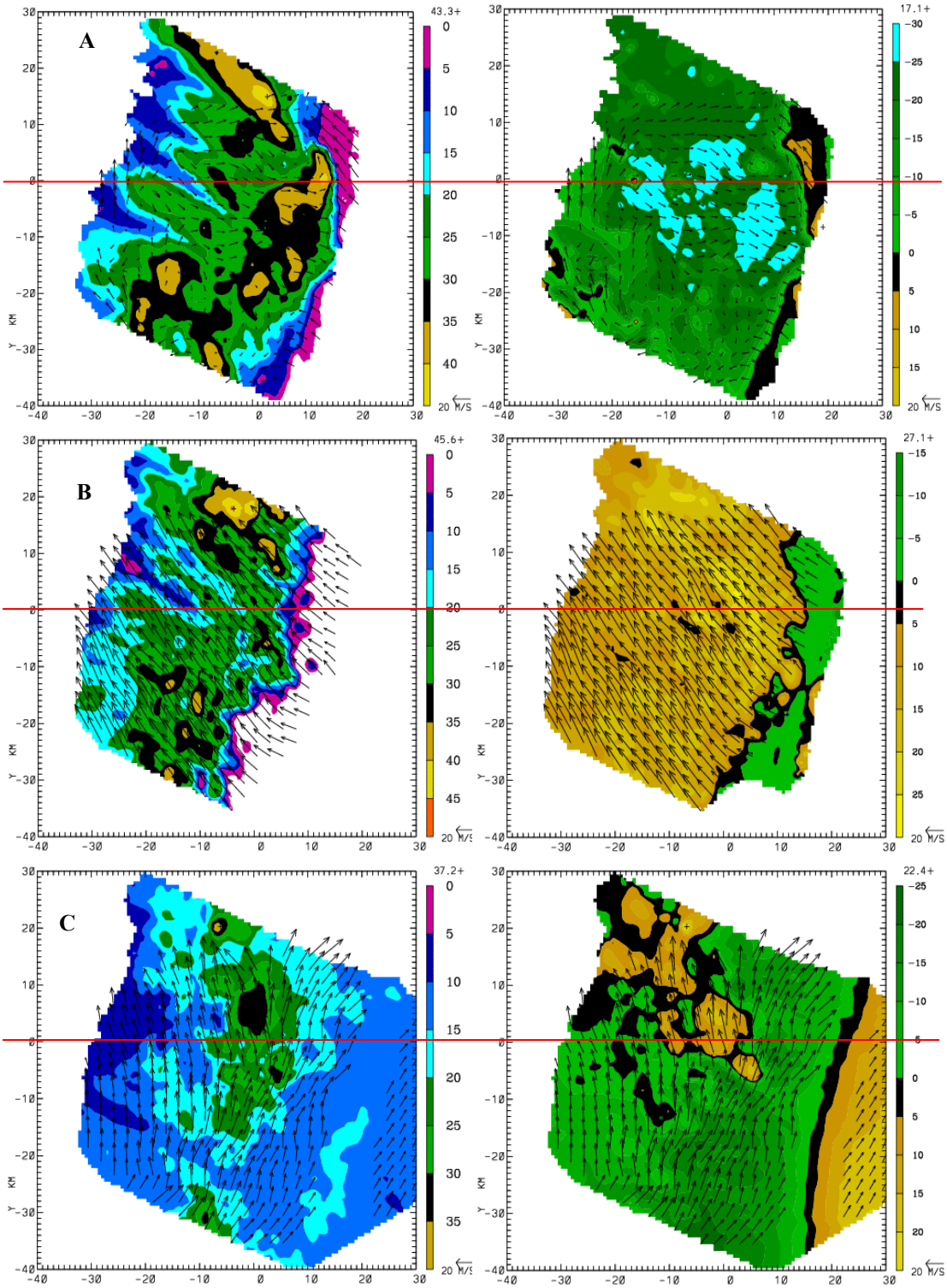

Figure 6.9: Eldora reflectivity and velocity scans for leg1 over the MIPS system. Dual doppler storm relative winds have been overlaid and are in units of m s^{-1}. (a) Z= 1 km, (b) Z = 5 km, and (c) Z = 10 km (AGL). Peak reflectivity at this time is 45 dBZ at 5km, and peak velocity values are -28 m s^{-1} at 1 km.

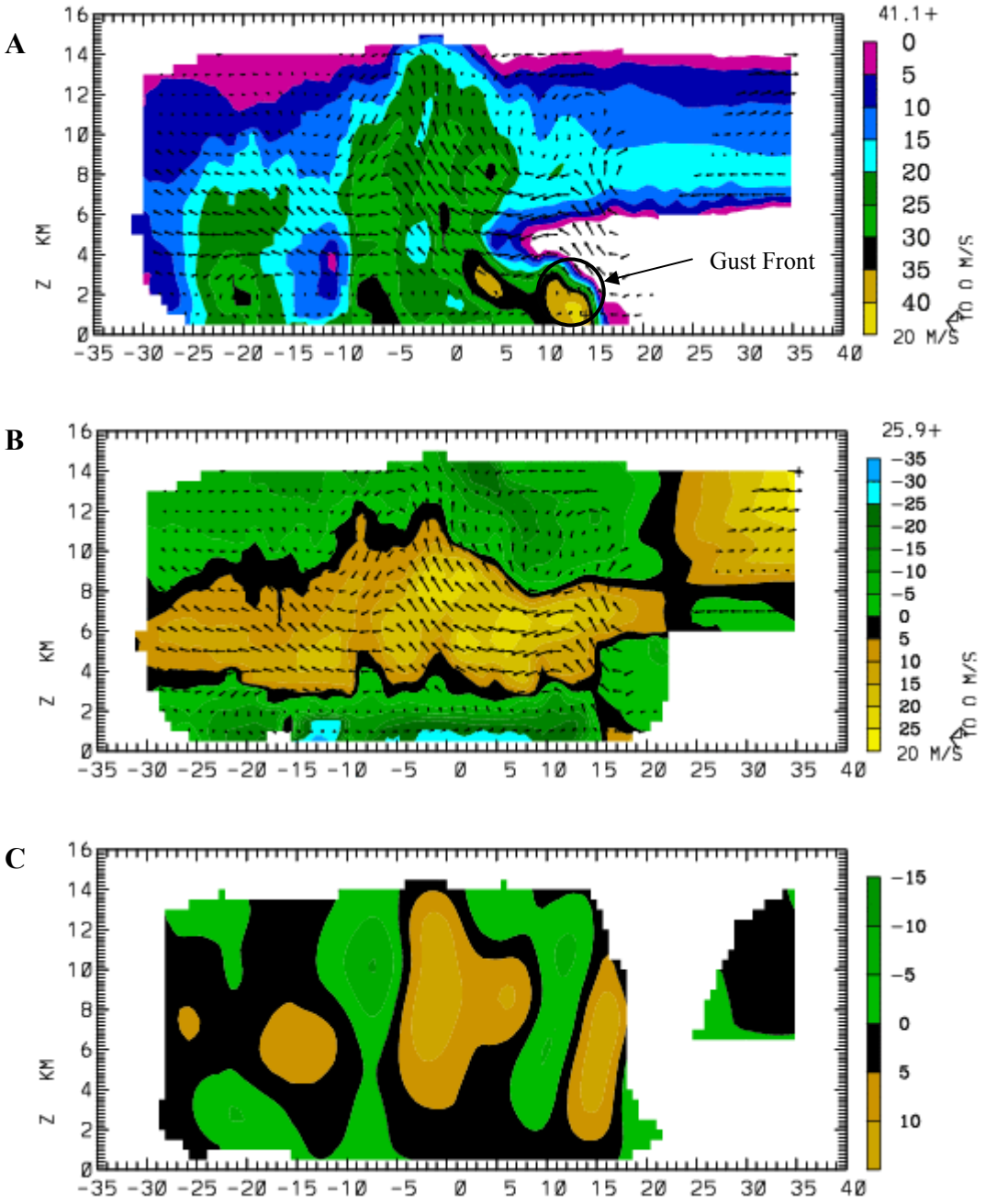

Figure 6.10: Vertical cross section from leg 3 of velocity data from the Eldora fore radar. The MIPS is located at the 0 point on the x-axis. (a) reflectivity (z), (b) Velocity (V_r), and (c) Vertical motion (w, m s^{-1}) . Dual Doppler winds (V_h) are overlaid in units of m s^{-1}. Axis units are in km.

from the south to southwest at 15 – 25 m s^{-1}, with the exception of more variable flow near the Z core just north of the MIPS. Figure 6.10 shows the vertical cross sections of (a) Z, (b) V_r, and (c) vertical motion (w) for leg 3. All parameters are now much weaker than pervious legs. During this leg the bow underwent a transformation into the decaying stage as the gust front raced out ahead of the system. This is shown in the circular area and is centered near x = 13 km, well ahead of the main core which is centered at or about x = -2 km. The maximum reflectivity during this leg of 41 dBZ was recorded by ELDORA within the gust front (Figure 6.10 (a)). During this period the MCS was undergoing rapid decay as evident from the Des Moines 88D radar, as well as the MIPS and ELDORA systems. Velocity data shows continuing strong flow that pushed the gust front further ahead of the of the bow echo.

Some key aspects of leg 3 include the following: (a) The core updraft, with a base near 4 km, has weakened to 10-15 m s^{-1}, and is no longer rooted to the surface. (b) The updraft along the gust front is stronger and deeper. The gust front circulation (denoted within the circular area) is the most prominent feature at this time. (c) A very weak downdraft is located at low levels on the upshear flank of the rapidly weakening reflectivity core. (d) The horizontal flow at 1 km is weaker and less that 30 m s-1 throughout the system. (e) The flow is front to rear within a deep layer (2 – 10 km AGL) and very weak below 2 km to the surface.

The ELDORA analysis for this case shows three main stages of bow echo evolution. Leg 1 is representative of the maturing stage; leg 2 of the bowing, apex stage; and leg 3 represents the decaying stage of the system. Reviewing and comparing each leg shows that the horizontal wind fields at the 5 km level changed very little with values

remaining between 30 – 35 m s^{-1} out of the southeast. However, between legs 1 and 2, and legs 2 and 3, the V_h signature changes rapidly from being dominated by inbound flow, to outbound flow, then back to the same inbound flow as measured in leg 1. The values are also very similar between legs 1 and 3, but very dissimilar when compared to leg 2 during the onset of the apex and surge to the east. At the 1 km level there are very few similarities in either the reflectivity or V_r data. The wind fields are all from similar directions (westerly), however there are little to no similarities in speed, which is to be expected. At 10 km it is clear that the system was near the peak in intensity during leg 1 because of the high reflectivity values being recorded at that level. During leg 2 and leg 3 the highest reflective values decreased greatly from 49 dBZ during leg 1 to 25 dBZ during leg 3. As the system began to surge, the deep upward motions were cut of, which sent the MCS into the decaying stage.

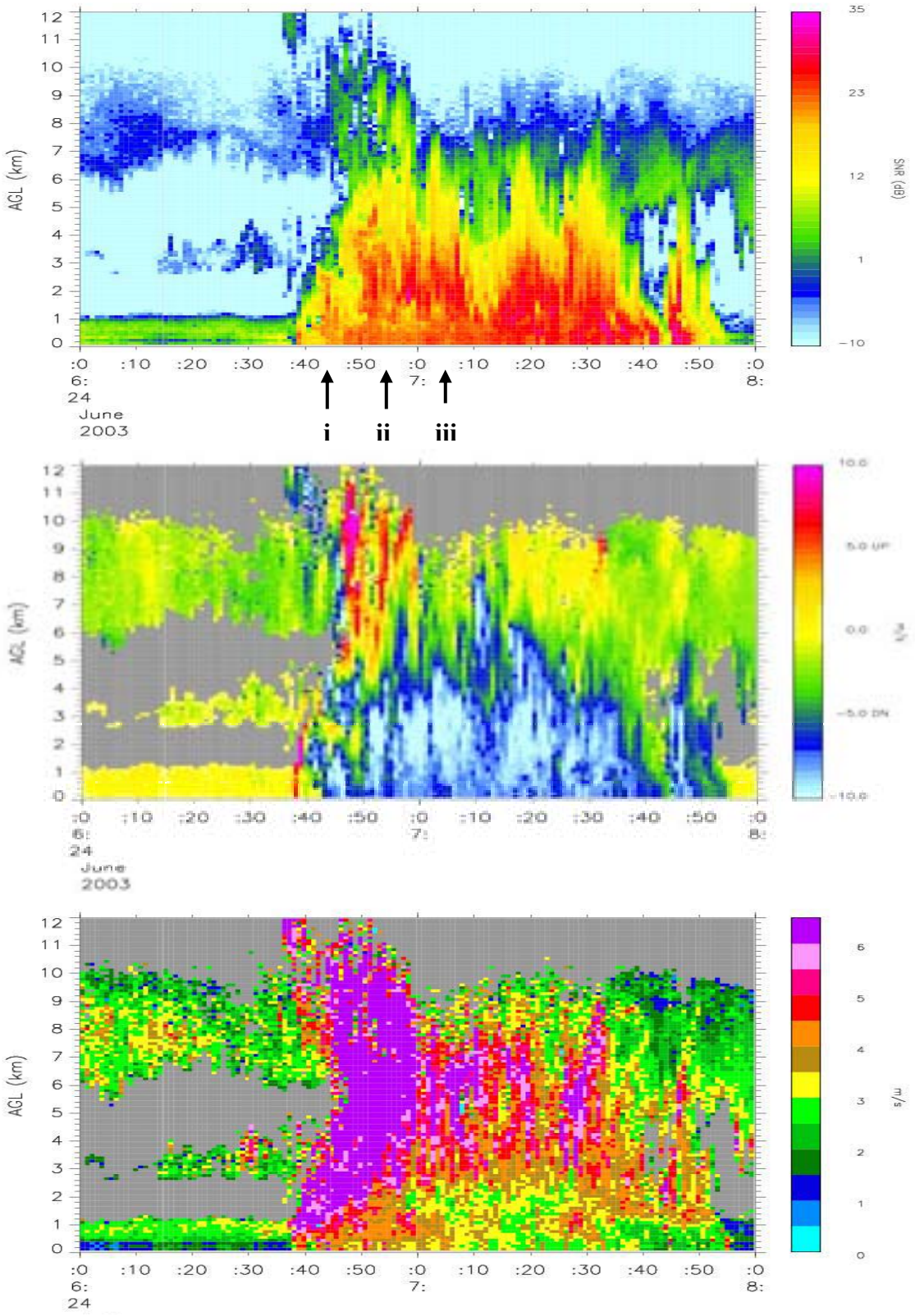

Figure 6.11 915 MHz Profiler time-height cross sections of (a) SNR, (b) Doppler velocity, and (c) spectral width for 24 June 2003.

6.3 MIPS Analysis

6.3.1 915 MHz Profiler

The MIPS 915 MHz Profiler provides a detailed time-dependent depiction of the bow echo vertical structure. The MIPS sampled approximately 1.25 h of continuous precipitation from 0640 to 0755 UTC. Figure 6.9 suggests primarily convective rain with little evidence of a well-formed brightband (BB) or stratiform rain within the MCS. The rear of the system presented a mixed convective-stratiform structure, even though no BB was detected. Figure 6.11 (a) reveals a convective structure throughout most of this period, as hydrometers extended to 6 km or above throughout the time series. The most intense periods of deep convection, i.e. where the hydrometers extended to the highest altitude, are denoted by i (0646 UTC), ii (0659 UTC), and iii (0707 UTC). Consequently, these areas of deep convection correspond to peak wind gusts at the surface, as well as high rain rates shown by the disdrometer and tipping bucket rain gage. Spectral width values (Figure 6.11 (c)) ranged between 5-8 m s^{-1} on the onset between 0645-0700 UTC, showing that the system was turbulent in nature with mixing occurring through the depth of the system, particularly between 0640 and 0700. After 0700 UTC the mixing and turbulence continued above 2-3 km, with spectral width values remaining near 5-7 m s^{-1}. Below this level values were much lower averaging near 2-3 m s^{-1}. The echo tops extend above 12 km between 0645-0700 UTC, while remaining near 10 km for the remainder of the time period.

The 915 MHz profiler vertical particle motion W, where $W = w + V_T$, is shown in Figure 6.11 (b). W values for the MCS reveal a prominence of updrafts at upper levels near the front of the MCS. These values are in the range of 8-12 m s^{-1} at 0645 UTC with

the highest values occurring near 6-12 km. With an updraft duration of 14 min, the implied updraft width is estimated from the updraft duration, multiplied by the bow echo speed. This calculation yields 14 min * 60 s/min * 18 m/s = 15 km, which agrees quite well with the updraft width from the Eldora analysis (vertical sections of w). A narrow region of W values between 8-10 m s^{-1} was sampled within the 0-2 km AGL layer near 0640 UTC as the gust front passed over the MIPS location.

The ceilometer time height section (Figure 6.12) reveals additional cloud and precipitation features. A decrease in low-level aerosol backscatter was measured after passage of the MCS. Such a decrease was associated with drier, potentially cooler air that originated above the pre-storm boundary layer.

The ceilometer also provides information on rain characteristics. In the 915 plots there were three distinct times of deep convection at 0646, 0659, and 0707 UTC. These periods show up as periods of reduced height coverage (due to greater extinction), as well as an increase in the backscatter value at lower levels, implying a greater

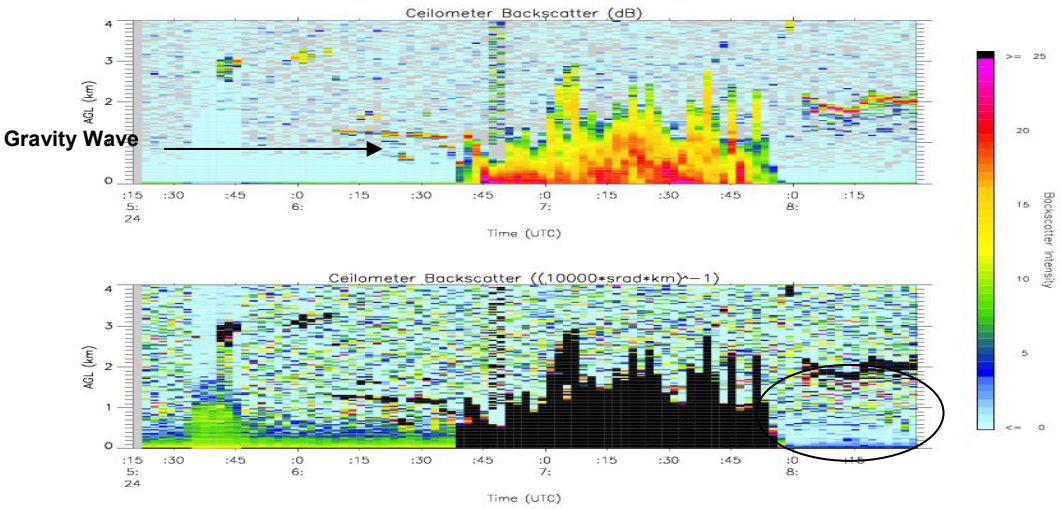

Figure 6.12: Time Height Series of MIPS Ceilometer. The top panel is ceilometer backscatter in units of dB. The bottom panel is backscatter in units of power. Heavy rain is denoted by the black color. The area in the circle shows how the atmosphere became more pristine after the passage of the bow.

extinction produced by heavy rain. Extinction in rain will become greater as the rain intensity increases which is shown in the three mentioned periods. During the first period (0646 UTC) the ceilometer recorded a maximum value of 25 dB, which is the highest value recorded for this MCS. The 915 recorded a value of 26 dB (SNR) for this same time period and height AGL. Extinction (or attenuation) of the ceilometer signal is also most substantial at this time. This implies heaviest rain (lowest visibility) at this time, in agreement with the disdrometer data presented in Section 6.3.3. The second distinct time of deep convection followed a similar pattern. However the third period was somewhat different shown by a higher cloud base measurement, suggesting cloud erosion by convective scale downdrafts.

6.3.2 High Resolution 915 MHz Winds

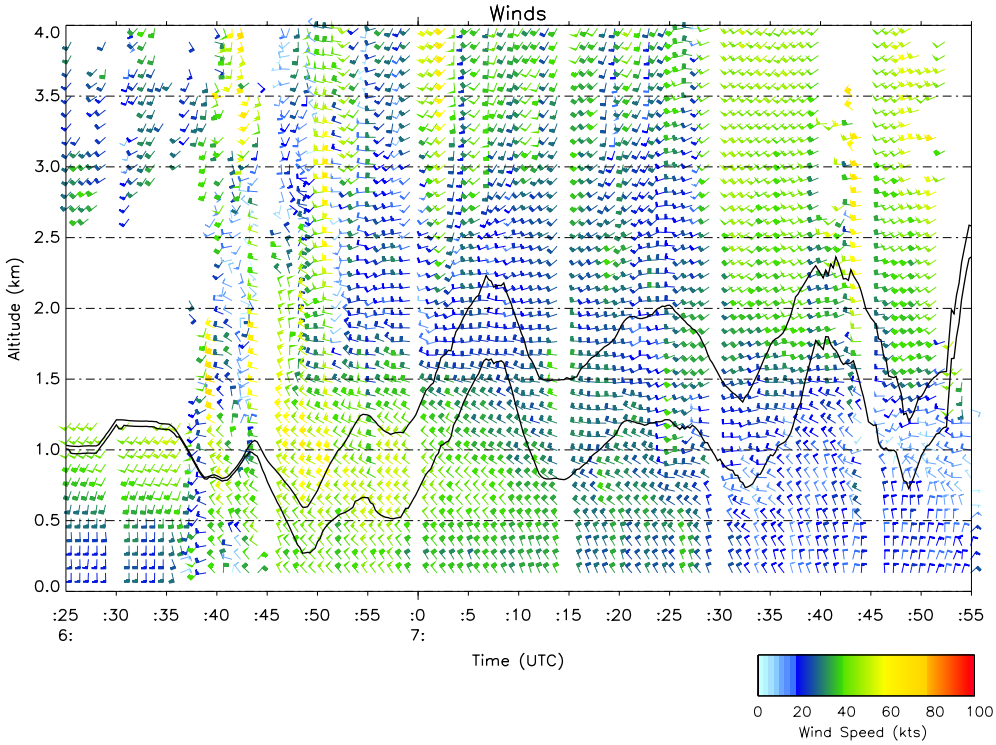

Figure 6.13: 915 MHz profiler high resolution ground relative winds. The gust front passage occurred at 0636 UTC and bow echo passage at the MIPS at 0645. Cloud base heights are shown by the black lines.

A time vs. height section of horizontal flow derived from the 915 MHz profiler is shown in Figure 6.13. The high resolution winds have been unfolded and are plotted as ground relative. The ceilometer cloud base heights are shown as black lines. The figure reveals two prominent features: (1) Strong southwesterly midlevel flow of 25 m s^{-1} was sampled at the back of the system. (2) The most significant wind change was confined to the lowest 2 km, where strong southerly winds (and the southerly jet near 1 km AGL) were replaced by weaker northerly flow (~7 m s^{-1}). Throughout the remainder of the MCS winds changed little over the time section.

6.3.3 Drop Size Distribution (DSD)

Raindrop size distribution data were acquired by a Joss-Waldvogel disdrometer calibrated prior to BAMEX. The disdrometer was co-located with two Texas Electronics tipping bucket rain gages. This disdrometer is capable of determining 20 size intervals of raindrop diameters ranging from 0.3 to 5.0 mm according to the magnitude of the raindrop impact. The number of counts in each of the 20 channels is recorded during a 1-min averaging period. Ulbrich (1983) showed that rain DSD could be approximated well by a modified gamma drop size distribution of the form

$$N(D) = N_o D^{\mu} \exp(-\Lambda D),$$

where N(D) is the number of drops per unit volume per unit size interval. The parameters $N_0, \Lambda,$ and μ represent the intercept, slope, and shape parameter. Figure 6.14 shows the rain drop size distribution for this system plotted logarithmically on a time vs. size plane. During the onset of the system the drop sizes ranged between 1-3 mm with a

maximum concentration of 2.8 near 1.7 mm. During the periods of strong winds defined in Figure 6.11 (a) the concentration and size of the drops increased from the mean values except for the last time period of 0707 UTC. As the system progressed over the MIPS, the drop sizes continued to decrease, but the concentration of drops increased over the same time period. At 0730, 0743, and 0750 UTC the highest concentration of drops were recorded (3-3.3), with drop sizes ranging between 0.3 and 1 mm. Figure 6.14 (b) shows the rain rate calculated by the disdrometer. The highest rain rates occur with the largest drop size concentrations at 0646, 0659, 0714, 0730, 0743, and 0750 UTC consistent with peak intensities of Z from the 915.

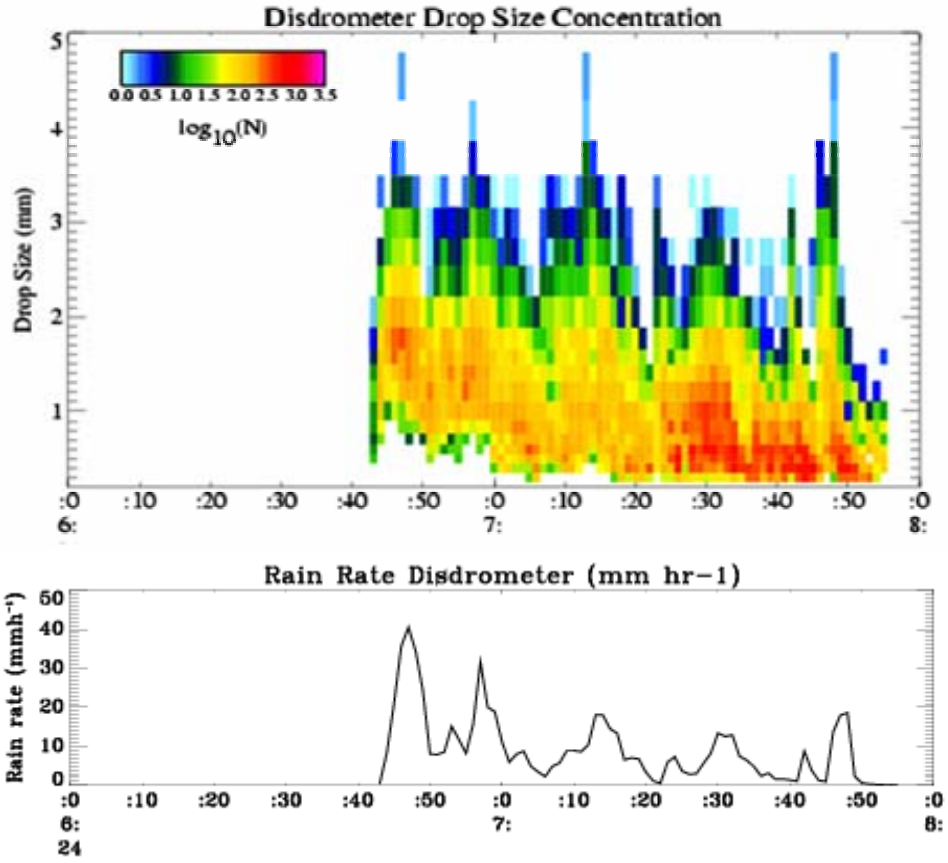

Figure 6.14 Disdrometer drop size concentration and rain rate time series from 0600 – 0800 UTC on 24 June. Note as the concentration of drops get smaller the rain rate decreases.

6.3.4 Derivation of w

The disdrometer data were used to calibrate the 915 MHz profiler to convert SNR values to reflectivity factor values (Z). Figure 6.15 shows the Z and vertical air motion time-height sections. If the terminal fall speed (V_T) for rain is assumed (hail was not observed at the surface) a relationship between Z and V_T can be determined from the disdrometer data. Vertical air motion is calculated from $W = w + V_T$, where W is the measured radial velocity at vertical incidence. Since graupel was present in the upper portion of the system above the freezing level, air motion above this level can not be

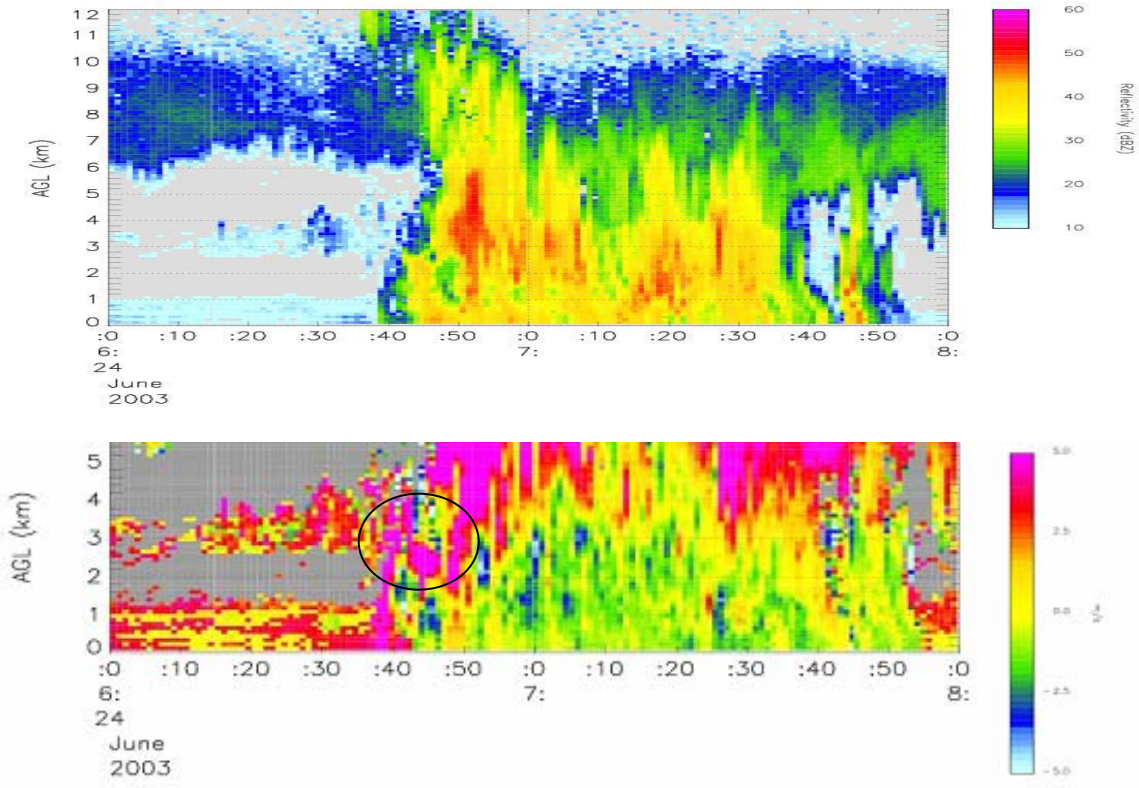

Figure 6.15: 915 MHz reflectivity (top) and air motion (bottom). Air motion was greatest along the gust front and with the initial onset of deep convection. Maximum upward air motion was 13 m s^{-1} along the gust front. Maximum Downward motion was -5 m s^{-1}.

accurately determined (work is on going to solve this problem). Figure 6.15 shows a low-level updraft along the gust front. The figure does however show the derived vertical air motion from the surface to just below the melting layer (5 km). Updrafts were primarily above 3 km and downdrafts dominated at levels below 3 km. The largest value of upward motion is analyzed at 0645 UTC near the front of the bow echo. The highest updraft recorded was 15 m s^{-1}, while the largest downdraft measured was 5 m s^{-1}. These patterns are generally consistent with the Eldora analysis in Fig. 6.10. As for the reflectivity the highest value was 56 dBZ within a deep convection core at 0652 UTC .

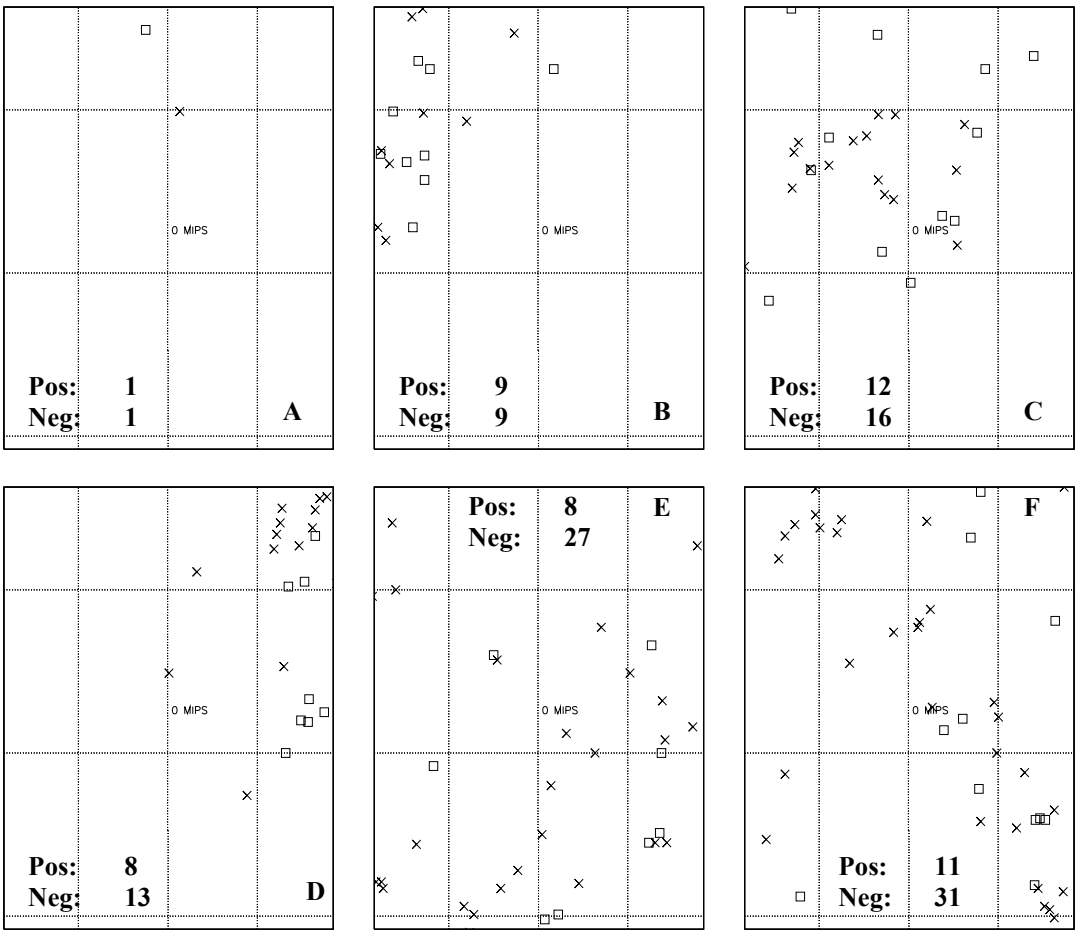

Figure 6.16 NLDN data centered in a 10 km x 10 km domain from a) 0525-0626 UTC b) 0626-0646 UTC c) 0646-0656 UTC d) 0656-0706 UTC e) 0706-0726 UTC f)0726-0816 UTC. Negative strokes are denoted by X's and positive strokes are denoted by 's. The MIPS is located in the center of the domain. Grid spacing centered on the MIPS in 2.5 km E-W and 3.5 km N-S spacing.

The peak rain rate occurs during the peak in the raindrop size at 0646. This rain rate approaches 44 mm h^{-1}, while the raindrop size approaches an average of 2 mm. This does not appear to match up with the values of Z recorded in the vertical section in Figure 6.10 from ELDORA, but if measurements were recorded just 3-4 km to the south, through higher Z, they may appear much different and compare with the ELDORA data.

6.3.5 Lightning and Electrical Behavior

Figure 6.16 shows the location of each cloud to ground (CG) flash within the domain of interest measured by the NLDN (National Lightning Detection Network). Each panel shows CG flash locations for the following time periods: a) 0525-0626 UTC, b) 0626-0646 UTC, c) 0646-0656 UTC, d) 0656-0706 UTC, e) 0706-0726 UTC, and f) 0726-0816 UTC. The negative flashes are denoted by X's and positive flashes are denoted by 's. Two properties are evident: (1) the total CG flashes for this system are relatively low and (2) negative CG flashes exceed positive CG flashes by 2 to 1. As the bow echo approached, the flash rate increased slightly, and continued at a higher rate after the passage. The ELDORA analysis in Figure 6.10 shows a relatively strong residual updraft along with elevated reflectivity factor up to 30 dBZ over the MIPS. This structure would likely sustain significant supercooled water and ice crystals required for charge separation, and hence continued lightning, around this time. After the initial onset the majority of CG flashes recorded were negative.

The electric filed mill (EFM) time series (Figure 6.17) provides additional information on lightning properties based on measurements of the vertical component of the electric field (E_z), sampled at a rate (50 Hz) sufficient to resolve lightning flashes.

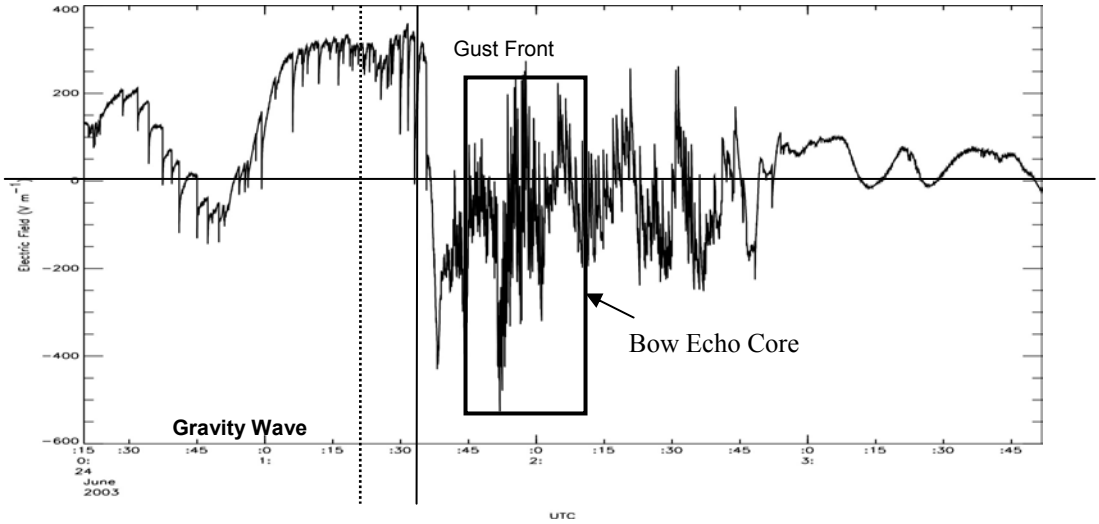

Figure 6.17: MIPS EFM Time Series. The gravity wave passage is denoted by the dashed line and gust front passage by the solid line. The neutral line is the black line across the time height series. Positive charge is above that line, and negative below it.

Local lightning flashes are represented as discontinuities (quasi-vertical lines) in the time series, and appear at frequent intervals, particularly within the bow echo core. Mesoscale features and subtle variations in E_Z are apparent in several locations: a gravity wave passage at 0625, the gust front passage at 0638 UTC and electric field oscillations near the trailing portion, and within the wake, of the receding and weakening bow echo. The total lightning flash count can be determined by coupling this data with the NLDN data.

For this analysis a radius of 10 km around the MIPS EFM and a 3.5 h period from 0515 UTC to 0845 UTC was used. After combining the EFM and NLDN data and removing duplicate flashes, a total of 240 lightning flashes were found during this period. Of these, 98 were cloud to ground (CG) flashes and 142 were inter-cloud (IC) flashes. The EFM does not distinguish between positive or negative flashes, so a comparison of the positive and negative flashes cannot be completed. Figure 6.18 shows the resulting time series of IC and CG flashes. As the system approached IC's flashes dominated.

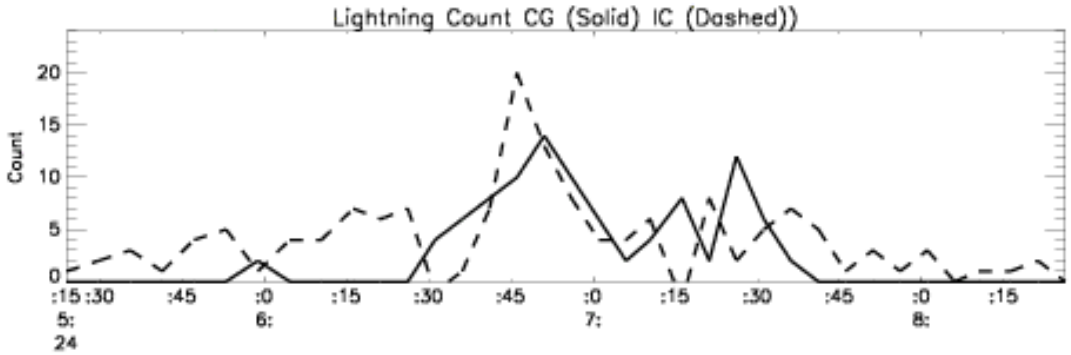

Figure 6.18: Total flash count for the period 0515 UTC – 0845 UTC on 24 June. Data collected from the National Lightning Detection Network and MIPS Electric Field Mill. Cloud-to-Ground (CG) is denoted by the solid line, while Inter-Cloud is denoted by the dashed line.

However just as the system arrived in the domain the CG flashes were comparable in number to the IC flashes. As the MCS passed through the domain the CG dominated for a short period, but the IC quickly return to occurring twice as often as the CG. The total lightning flash rate was relatively low with an average rate of 1.2 flashes per minute. During the peak convective time of (0636-0736 UTC), the flash rate increased to 2.6 flashes per minute over the domain. Past studies of MCS have focused on positive and negative CG flash rates. There has been little work on MCS total flash rates of CG and IC flashes combined. In this case the CG flash rate during deep convection over the region (0636-0736 UTC) was found to be approximately 1.5 flashes per minute. Morgenstern (1991) found that CG flash rates in MCSs to be much higher, with median values of approximately 9.5 flashes per minute during a study of 25 warm season MCSs.

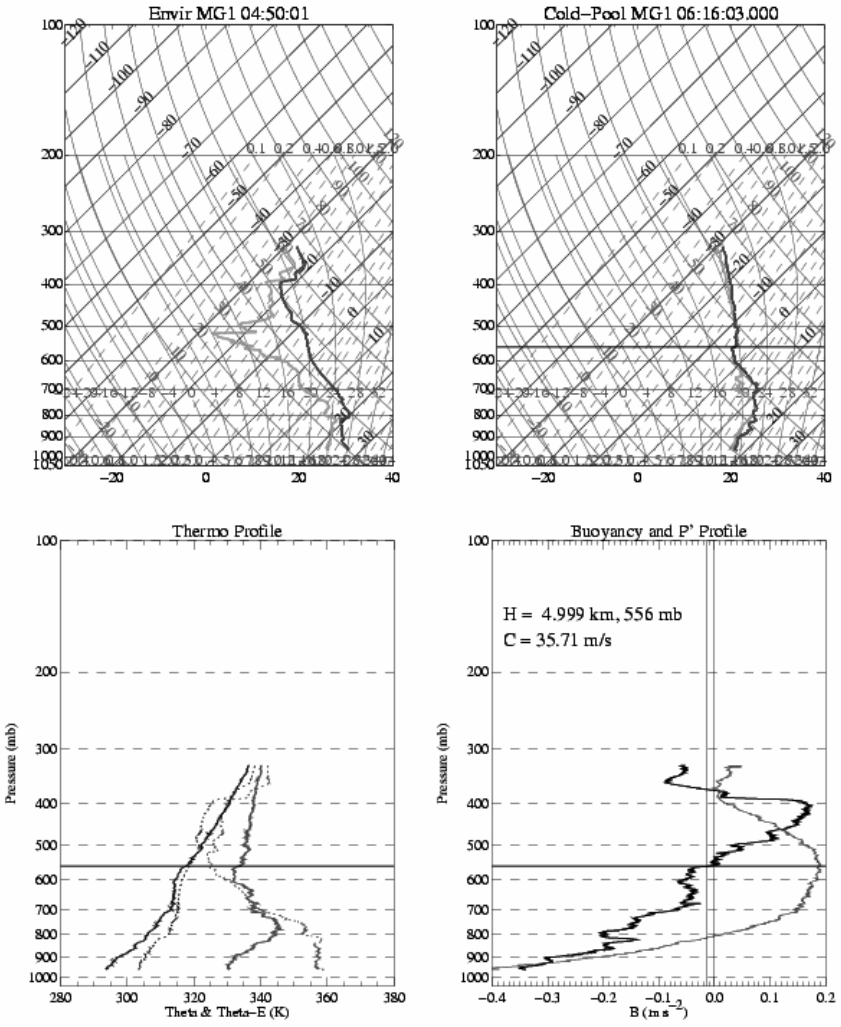

Figure 6.19 Cold Pool Analysis. (a) Environmental sounding released at 0450 UTC, (b) cold-pool sounding released at 0616, (c) thermodynamic profile (solid line is theta, dashed line is theta-e), and (d) the buoyancy profile (dark) and pressure profile (light) for this system.

6.3.6 The Cold Pool

Over the past two decades several idealized numerical modeling studies have shown a relationship between the structure of a mesoscale convective system (MCS) and a non-dimensional parameter relating cold pool strength (C) to environmental wind shear (ΔU). One goal of BAMEX was to measure cold pool parameters. To accomplish this at least two soundings are needed: one in the undisturbed environment ahead of the system, and one in the system's cold pool. For this case a total of four soundings fit these criteria. A pre-storm environmental sounding was released at 0450 UTC from MGLASS1. The cold pool sounding was released at 0616 from the same location as the previous sounding. These two soundings are shown in Figure 6.19.

The environmental sounding was released in an environment that had not been disturbed by convection, but it was released as the NBL was maturing. The cold pool sounding was released in the middle of the convective region near the end of the precipitation (denoted by triangle on Figure 6.3). The trailing stratiform line weakened rapidly after passing the MGLASS1 site. The cold pool sounding also shows the melting layer near 610 mb (4256 m). For this case the buoyancy profile is negative (a net cooling was produced) from the surface to 557 mb.

To understand the cold pool two quantities C (cold pool strength) and ΔU (low-to-mid-level shear) must be analyzed. C is defined by the following formula:

$$C^2 = \frac{2}{\overline{\rho}(z=0)} \int_0^H (\overline{\rho} B) dz \,, \qquad (6.1)$$

where z is height, H is the cold pool depth, ρ is density, and B is buoyancy. The cold pool height from this analysis appears to be near 4.9 km. However the 915 wind observations in Figure 6.13 suggest a cold pool depth of 1.5 km, if one assumes that the

southerly flow marks the top of the cold air. There has been great debate on where the top of the cold pool actually exists, and without further analysis of other cases it is hard to say which is correct. Past studies such as Rotunno et al. (1988) and Weisman et al. (1988) have stated that when $C > \Delta U$ the cells tend to tilt up-shear and when $C < \Delta U$ cells tend to lean down-shear. Model simulations typically produce a trailing stratiform system when $C > \Delta U$. For this case the strength of the system's surface-based cold pool, measured by C, was found to be 35.7 m s^{-1} The low to mid-level (950-600 mb) vertical wind shear in the environment, measured by ΔU, was found to be 9.9 m s^{-1}. In this case, little to no stratiform precipitation occurred with the southern end of the system, only with the northern portion of the MCS. However, there is some suggestion that weakening systems tend to have $C >> \Delta U$, while mature and intensifying tend to have a $C / \Delta U$ ratio closer to 1 (Bryan et al. 2004). In this case the system did decay rapidly after moving through the domain which fits well with the above theory.

CHAPTER VII

DISCUSSION, SUMMARY, & CONCLUSION

7.1 Discussion

A. Overall Scientific Objectives of BAMEX

The study of long-lived convective mesoscale convective systems (MCSs) continues to be a prominent topic in meteorology, because of the effects these system have on local weather anywhere in the continental United States. During the BAMEX planning sessions several goals and questions were formulated. Some of the goals and questions were directed at MCV's and MCS's, while others were directed solely at bow echoes. The 24 June 2003 case study dealt primarily with a bow echo event that emerged from a much larger-scale MCS. The overall goal of this study was to document the evolution of a bow echo event using both airborne and ground-based measurements.

B. Environmental Objectives of BAMEX

Many of the MCSs that occur in the US form and mature in the early evening into the nighttime hours. One major goal of BAMEX was to determine the atmospheric conditions that are conducive to bow echo genesis. Past studies (e.g., Johns and Hirt 1987, Bentley and Mote 1998, Evans and Doswell 2000) have shown a wide range of

synoptic and mesoscale conditions in which MCSs and bow echoes have formed. In this case study some of the past findings were found to match the conditions across this domain. This system formed in an area of 500 mb westerly flow with speeds of 20 m s^{-1}. Past studies have shown this to be an ideal location, but have also stated that the average speed is closer to 11 m s^{-1} on average. This system also formed just south of a diffuse stationary front which was draped from east to west across the domain. CAPE values were found to be near 2800 J kg^{-1}, lower than the average value of 4500 J kg^{-1} which has been found to be an ideal value for formation and longevity. However, a value of 4500 J kg^{-1} would lead to updrafts in the order of 100 m s^{-1} if all of the CAPE is transformed to vertical kinetic energy. In this case the 2800 J kg^{-1} would lead to updrafts on the order of 75 m s^{-1}, still very strong, and far greater than the values of about 20 m s^{-1} recorded by the ELDORA and the 915 profiler. With the lower CAPE value a bow still formed and persisted for approximately 2 hours.

A second goal was to examine the NBL and CBL effects on MCSs and bow echoes more specifically. Many severe bow echoes occur during the nighttime hours in which the stable NBL does not as readily support the generation of intense deep convection and a strong surface cold pool. Bernardet and Cotton (1998) inferred that the interactions between deep convection and the stable boundary layer, produce internal gravity waves which generate severe winds at the surface. This case did occur during the nighttime hours in which the NBL was in the process of maturing. Although severe winds were not reported for this case, the MIPS measured strong wind gusts to 24 m s^{-1}, and the highest winds measured by the ELDORA were 35 m s^{-1} near 1 km AGL during leg 2. In section 5.1 an analysis of mean NBL mean parameters showed several gravity

waves propagating ahead of the system during deep convection. Two of these waves (GW1U & GW2U) appeared to propagate along an inversion layer centered near 3 km, and a third wave GW1L propagated within the NBL stable layer near 700 m. The fundamental properties of the NBL (θ, θ_e, r_v) showed these waves as fluctuations in each parameter during passage over the MIPS location. However, these waves did not change the surface winds, temperature, or dewpoint, but did have pressure oscillations associated with them.

C. System Morphology and Evolution Objectives

A primary goal of BAMEX was to gain a better understanding of the physics of bow echoes, as well as to determine the general applicability of Fujita's (1978) conceptual model of bow echoes. In Fujita's model the bow echo forms from isolated convective cells, transforms into a convective line, evolves to a bowing line with an apex, followed by a comma-shaped echo, and finally to a decaying convective line with residual mesoscale vortices. The bow echo in the present case formed in a broadly similar sense, with initiation of convection over South Dakota and northern Nebraska, and evolution to a convective line over western Iowa. From this point the bow formed along the line, but did not form the common comma head as described by Fujita. The bow in this case was imbedded within a much larger MCS and was not an isolated MCS. A major departure from the Fujita model is that the formation of the bow echo appears to be related to the eastward propagation of an intense convective feature that was present along the western domain (diamond in Figure 6.2a). As the evolution was occurring, a strong cell to the rear of the system propagated at a higher rate (25 m s^{-1}) and as this

feature approached the leading edge of the MCS the bow echo surged towards the east and the maximum V_r values were recorded. This convective impulse may have propagated as a large amplitude gravity wave as it encountered the stable outflow. After forming an apex the system began to decay and loose its convective signatures. This bow echo also did not have a trailing stratiform rain region behind the leading convective line. In most studies of bow echoes such stratiform rain is present, and is thought to contribute to the development of the cold pool and descent of the rear inflow jet. In the present case the rear inflow jet did not descend to the surface. These two factors alone suggest that there is great difficulty in generalizing how a bow echo and how an MCS with develop and mature on any given day. The conceptual model can be followed in a general sense, but when analyzed in more detail, the model has serious problems in dealing with specifics such as the stratiform rain and rear inflow jet.

A second objective dealt with the many questions that have risen concerning the relationship between the system's buoyancy and structure. For this case a analysis of several soundings depicted the development of a cold pool. The analyzed buoyancy profile shows that this system had negative buoyancy (a net cooling was produced) from the surface to 557 mb. Past studies such as Rotunno et al. (1988) and Weisman et al. (1988) have stated that when $C > \Delta U$ the cells tend to lean up shear and when $C < \Delta U$ the cells tend to tilt down shear. Model simulations typically produce a trailing stratiform system when $C > \Delta U$. For this case the strength of the system's surface-based cold pool, measured by C, was found to be 35 m s^{-1}. The low- to mid-level vertical wind shear in the environment, measured by ΔU, was found to be 10 m s^{-1}. In this case, little to no stratiform precipitation occurred. However, Bryan et al. (2004) completed a cold pool

study on all bow echo cases from BAMEX in which two soundings were available. His analysis suggests that weakening systems tend to have C >> ΔU, while mature and intensifying tend to have C / ΔU closer to 1. In this case the system did decay rapidly after moving through the domain, consistent with the theory mentioned above for decaying systems.

In regards to the rear-inflow jet and the cold pool several hypothesis have been considered regarding the physics of the relationship between a strong cold pool and strong surface winds. Figure 2.5 shows two types of internal flow that a bow echo may assume. In this case it was found that the rear-inflow jet did not reach the surface. This was documented by the 915 as well as by ELDORA. Referring back to Figure 6.7, which is the vertical cross section of the ELDORA reflectivity, a comparison can be made with the above figure. There appears to be an elevated rear-inflow jet present in (a) and (b), but not (c). The cold pool is strong, which was discussed in the previous paragraph, and there is a gust front racing ahead of the main line. The rotations shown in Figure 6.1 caused by horizontal vorticity can be seen in the ELDORA wind field as there is positive vorticity ahead of the system, as well as a negative vorticity just behind the front edge of the system near the surface. There is an elevated negative vorticity circulation also present in the rear of the system behind the main core. Leg 1 fits well with this flow field, however legs 2 and 3 do not match up as well as leg 1. This is the case because the system is beginning to decay and loose its convective structure. Also, there is a shallow (1 km) layer of outflow air associated with the bow during leg 2. This layer is not present in leg 1 or leg 3. During leg three the circulation associated with the anvil begins to be the dominate flow with in the MCS, which continues to bring in dryer air into the system.

This air could also lead to further and quicker decay of the MCS. From the analysis possibly when there is a rear inflow jet there will be a deep and strong cold pool associated with the system. It could also be said that when the rear-inflow jet is elevated surface wind damage will be minimal, with the strongest winds along the gust front. However, it is impossible to determine if the cold pool caused the rear-inflow jet to remain elevated, or if the elevated rear-inflow jet caused the cold pool to be large, or if it is a combination of the two.

One final objective that can be addressed with this system deals with the role that pre-existing surface boundaries play in enhancing bow echo severity and longevity. The day prior to this case, 23 June 2003, a large complex of storms formed in southeastern Nebraska and northern Kansas. This system initially was a group of severe super cells that produced record setting hail stones, and tremendous rainfall across the area. The MIPS was setup to the northeast of these storms and recorded a heat burst event for several hours during the night on the 23rd and unto the morning on the 24th. The dry air that was measured at the MIPS site had far reaching effects across the region. Figure 7.1 shows a time series of the suominet plot of precipitable water vapor (PWV) starting at 08 UTC on 23 June and ending at 08 UTC on 24 June. By analyzing the suominet data the dry air produced during the heat burst remains in central and west central Iowa during the entire time series, until 08 UTC on 24 June as the MCS moves through. Values at the suominet site in Omaha, NE recorded a value for PWV of 2.1 cm at 17 UTC on the 23rd. To the east in Des Monies the suominet site there recorded a low value of 2.9 cm at 20 UTC on the 23rd as well. The air remained entrenched across the area, which could have set up a boundary to the north and to the south. On the northern side the boundary may

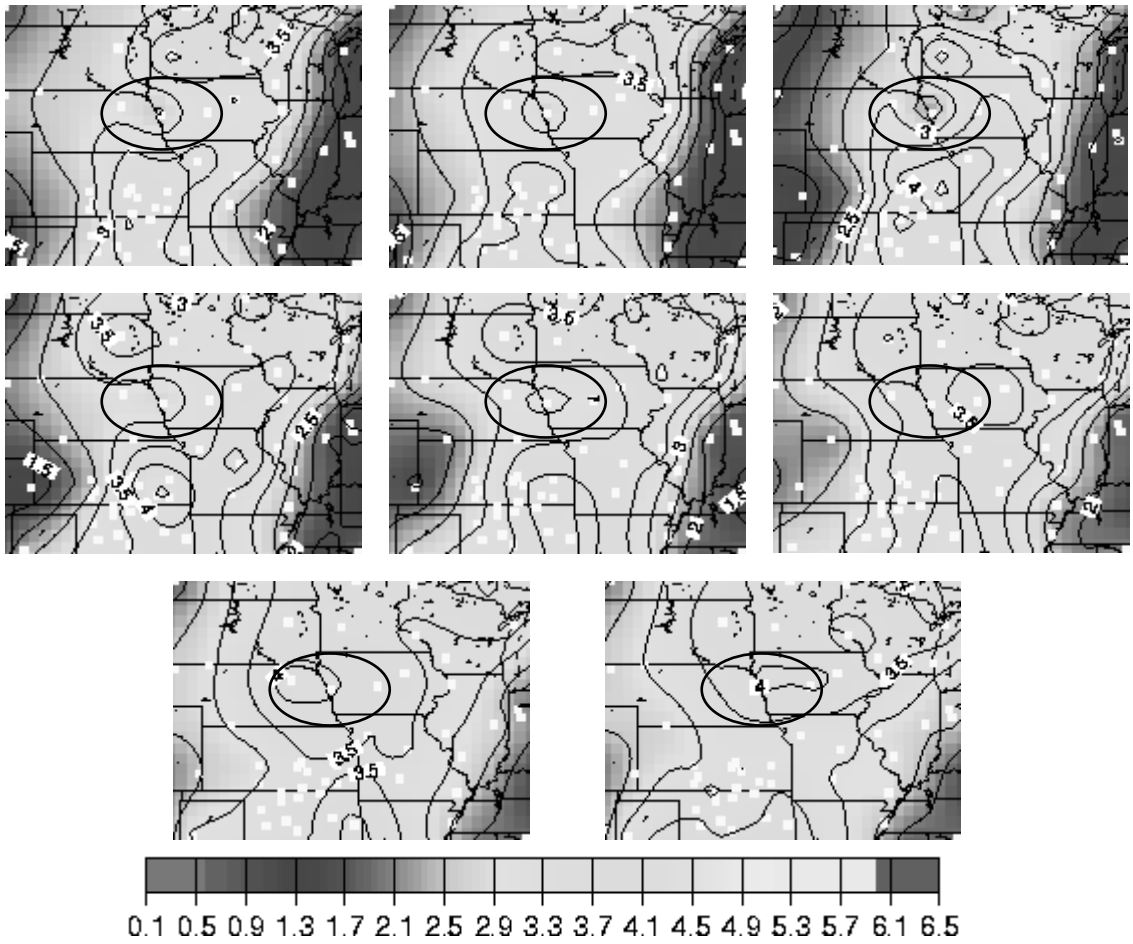

Figure 7.1 Suominet PWV from 08 UTC on 23 June until 08 UTC on 24 June 2003. Dark colors represent dry air, light colors represent high PWV. Each images represents 1-hour and there is 3-hrs between each image. Note the drier air within the circular air which remains until the bow passage through the area.

have led to the initiation and development of the system and at the same time caused the system to decay as it moved into the drier air across Iowa. To the north in Minnesota values of PWV remained above 4 mm for the entire series, which could account for the MCS continuing and maturing in that area long after it had decayed across Iowa.

7.2 Summary

The 24 June 2003 MCS was one of many storms sampled during the BAMEX project across the Midwest. This case was unique in the fact that it did produce a strong radar indicated bow echo, strong winds of 24 m s^{-1} that were just below damage threshold. It was also unique in the fact that it had little to no stratiform rain in the wake, and that it decayed quickly as it moved across central Iowa.

Over its 7-hour life cycle across Iowa and 2-hr time series sampled by the MIPS, this MCS exhibited several noteworthy characteristics. These include:

- NBL depth of 800 m, several oscillations in the mean quantities, (θ, θ_e, r_v) due to gravity waves propagating along the top of the NBL and another stable layer near 2.5 km AGL
- maximum reflectivity value of 54 dBZ from ELDORA at a height of 4 km. The MIPS 915 profiler recorded a maximum Z value of 55 dBZ.
- vertical development up to 15 km
- maximum surface wind gust of 24 m s^{-1} at 0646 UTC
- maximum radial velocity from ELDORA of 40 m s^{-1} at 1 km within the cold pool
- maximum cold pool depth of 4.9 km was is not consistent with the depth of 1.2 km as seen in the 915.
- maximum upward motion of 15 m s^{-1} at 3.5 km just behind the gust front measured by the 915 profiler, and 20 m s^{-1} at 4 km measured by ELDORA.
- strong rotations centered at 8 km associated with the anvil measured by ELDORA in legs 2 and 3, which could have led to the rapid decay of the bow.
- several gravity waves within and in the wake of the system

- lack of any stratiform precipitation in the wake of the system
- 13 mm of rain during a 1.25 h period, with a peak rain rate of 44 mm hr^{-1}

Overall this system matched well in part to past studies conducted both during field projects and through numerical studies conducted by Weisman et al. The main difference appears to be the role of a convectively-induced gravity wave originating from the intense deep convection on the west side of the MCS. This type of structure has not been well documented by past studies. However it appears that it may be a common feature due to the fact that another case from BAMEX shows similar findings. This was a bow echo segment originating from a much larger MCS. Since work has been limited on bow echoes and MCSs it is hard to make general statements about this system compared to other because of the limited data. This case did not allow for an analysis of many of the key scientific objectives laid out for BAMEX. Some of these objectives include but are not limited to: tornadogenesis, documenting in detail the process of up-scale growth from individual cells to coherent bow-shaped segments (was done in some degree, but with only 1 ground based instrument and no air based instruments), and looking at how the importance of lower-tropospheric versus middle-to-upper-tropospheric vertical wind shear. This was a good case to study an elevated cold pool, as well as a case where there were strong velocity signature, 40 m s-1 from ELDORA, but no damage reports, and no severe wind speed reports across the domain.

7.3 Errors and Improvement

As the understanding of weather events such as severe storms, bow echoes, and MCSs continues to grow, so does the knowledge of how to best assess these events.

Therefore, there exists room for errors as well as improvements, and this case study does not fall exception to the rule. Processing and analysis techniques included assumptions and estimations and room for improvement exists in both areas.

Having limited upper air data, estimating the boundary layer values and air mass stability may not be as accurate as one would like it to be. Instrument failures during this case also hindered storm assessment. Many of the MGLASS soundings did not extend above the 900 hPa level, some reached to 300 mb, but none reached the tropospheric level which brings in uncertainty in the atmospheric parameters. Winds for the most part were missing from all but 1 sounding for this case.

To better understand the ELDORA data and extract as much information as possible, assimilation of the raw data was carried out using various software packages to enhance the analysis. Much of the ELDORA data had to be filled or patched because of the convective nature of the line causing the NRL-P3 to maneuver around instead of keeping a straight track. This brings in error not only in the data for the fore and aft reflectivity and velocity, but also in the dual Doppler wind analysis. Another source of air comes from the way the winds are calculated within the analysis program. When performing the 915 calibration to calculate reflectivity and air motion using the disdrometer error come in because of the assumptions that are made. Also if there is ice present it must be accounted for. To date there has been little work done on this subject in regards to graupel in a system. Most work has focused on brightband contamination and how to work through it.

7.4 Applications

One of the most important reasons to study bow echoes and MCSs is to help forecasting and nowcasting issues at present. Much of the severe wind damage across the U.S. today is associated with bow echoes and MCSs. This purpose of this case study is to help forecaster better foresee a bow echo initiation so that warning can be issued with enough lead time to safe life and property. While performing this case study several interesting observations were discovered, basically because research and cases are limited in this area. One of the most surprising findings was that this system, even though it had velocities near 40 m s^{-1} at 1 km AGL they never reached the ground. This could be due to the fact of a strong cold pool which was measured to approximately 1.2 km by the 915 MHz profiler. The system had a very low flash rate compared to other MCSs, and overall had a lower rate than a common afternoon thunderstorm. To fully understand these systems, the cold pool and rear-inflow jet must be understood. These two parameters play a potentially important role in transporting high winds to the surface. It is clear that a good understanding of the environment is needed to support initiation, but there is some discrepancy in what type of environment is needed to sustain these systems. From this case it appears that drier air from the previous days convection, as well as from the large anvil present with this MCS had a major impact in decaying a system quickly. There was not really change in other parameters as the system moved through Iowa, except for the drier air in place. By gather as much information and combining all the instrumentation from the project a better understanding will lead to improved forecasting of strong winds from bow echo phenomena.

REFERENCES

Atkins, N. T., and R. W. Przybylinski, 2000: Radar and damage analysis of the 27 May 2000 tornadic derecho event. Preprints, *21st Conf. on Severe Local Storms,* San Antonio, TX, Amer. Meteor. Soc., 567–570.

——, J. M. Arnott, R. W. Przybylinski, R. A. Wolf, and B. D. Ketcham, 2004: Vortex structure and evolution within bow echoes. Part I: Single-Doppler and damage analysis of the 29 June 1998 derecho. *Mon. Wea. Rev.,* **132,** 2224–2242.

Burgess, D. W., and B. F. Smull, 1990: Doppler radar observations of a bow echo associated with a long-track severe windstorm. Preprints, *16th Conf. on Severe Local Storms,* Kananaskis Park, AB, Canada, Amer. Meteor. Soc., 203–208.

Davis, C., and Coauthors, 2004: The bow echo and MCV experiment (BAMEX): Observations and opportunities. *Bull. Amer. Meteor. Soc.,* **85,** 1075–1093.

Evans, J. S., and C. A. Doswell, 2001: Examination of derecho environments using proximity soundings. *Wea. Forecasting,* **16,** 329–342.

Forbes, G. S., and R. M. Wakimoto, 1983: A concentrated outbreak of tornadoes, downbursts and microbursts, and implications regarding vortex classification. *Mon. Wea. Rev.,* **111,** 220–236.

Fovell, R. G., G. L. Mullendore and S. H. Kim, 2005: Discrete propagation in numerically simulated nocturnal squall lines. Monthly Weather Review, in review.

Fujita, T. T., 1971: Proposed mechanism of suction spots accompanied by tornadoes. Preprints, *Seventh Conf. on Severe Local Storms,* Kansas City, MO, Amer. Meteor. Soc., 208–213.

——, 1978: Manual of downburst identification for project Nimrod. Satellite and Mesometeorology Research Paper 156, Dept. of Geophysical Sciences, University of Chicago, 104 pp.

——, 1979: Objectives, operation, and results of project NIMROD. Preprints, *11th Conf. on Severe Local Storms,* Kansas City, MO, Amer. Meteor. Soc., 259–266.

——, 1981: Tornadoes and downbursts in the context of generalized planetary scales. *J. Atmos. Sci.,* **38,** 1511–1534.

——, 1992: Mystery of severe storms. SMRP Research Paper 239,University of Chicago, 298 pp.

——, and R. M. Wakimoto, 1981: Five scales of airflow associated with a series of downbursts of 16 July 1980. *Mon. Wea. Rev.,* **109,** 1438–1456.

——, G. S. Forbes, and T. A. Umenhofer, 1976: Close-up view of 20 March 1976 tornadoes: Sinking cloud tops to suction vortices. *Weatherwise,* **29,** 117–131.

Funk, T. W., K. E. Darmofal, J. D. Kirkpatrick, V. L. DeWald, R. W. Przybylinski, G. K. Schmocker, and Y.-J. Lin, 1999: Storm reflectivity and mesocyclone evolution associated with the 15 April 1994 squall line over Kentucky and southern Indiana. *Wea. Forecasting,* **14,** 976–993.

Hall, F., and R. D. Brewer, 1959: A sequence of tornado damage patterns. *Mon. Wea. Rev.,* **87,** 207–216. Houze, R. A., S. A. Rutledge, M. I. Biggerstaff, and B. F. Smull, 1989: Interpretation of Doppler weather radar displays of midlatitude mesoscale convective systems. *Bull. Amer. Meteor. Soc.,* **70,** 608–619.

Johns, R. H., 1993: Meteorological conditions associated with bow echo development in convective storms. *Wea. Forecasting,* **8,** 294–299.

——, and W. D. Hirt, 1987: Derechos: Widespread convectively induced wind-storms. *Wea. Forecasting,* **2,** 32–49. Jorgensen, D. P., 1993: Meteorological conditions associated with bow echo development in convective storms. *Wea. Forecasting,* **8,** 294–299.

——, and B. F. Smull, 1993: Mesovortex circulations seen by airborne Doppler radar within a bow-echo mesoscale convective system. *Bull. Amer. Meteor. Soc.,* **74,** 2146–2157.

Lafore, J.-P., and M. W. Moncrieff, 1989: A numerical investigation of the organization and interaction of the convective and stratiform regions of tropical squall lines. *J. Atmos. Sci.,* **46,** 521–544.

Miller, D. J., and R. H. Johns, 2000: A detailed look at extreme wind damage in derecho events. Preprints, *20th Conf. on Severe Local Storms,* Orlando, FL, Amer. Meteor. Soc., 52–55.

Mullendore, G. L., and R. G. Fovell: Conditioning of the inflow environment by organized convection: An investigation based on BAMEX data. Preprints, *11th Conf. on Mesoscale Processes,* Albuquerque, NM, Amer. Meteor. Soc., 52–55.

Oye, R., 1994: REORDER: A program for gridding radar data. Field Observing Facility, National Center for Atmospheric Research, 20 pp. [Available from Atmospheric Technology Division, NCAR, P.O. Box 3000, Boulder, CO 80307.].

Pfost, R. L., and A. E. Gerard, 1997: "Bookend vortex"—Induced tornadoes along the Natchez Trace. *Wea. Forecasting,* **12,** 572–580.

Przybylinski, R. W., 1995: The bow echo: Observations, numerical simulations, and severe weather detection methods. *Wea. Forecasting,* **10,** 203–218.

——, and W. J. Gery, 1983: The reliability of the bow echo as an important severe weather signature. Preprints, *13th Conf. on Severe Local Storms,* Tulsa, OK, Amer. Meteor. Soc., 270– 273.

——, and D. M. DeCaire, 1985: Radar signatures associated with the derecho, a type of mesoscale convective system. Preprints, *14th Conf. on Severe Local Storms,* Indianapolis, IN, Amer. Meteor. Soc., 228–231.

——, G. K. Schmocker, and Y.-J. Lin, 2000: A study of storm and vortex morphology during the intensifying stage of severe wind mesoscale convective systems. Preprints, *20th Conf. on Severe Local Storms,* Orlando, FL, Amer. Meteor. Soc., 173– 176.

Schmidt, J. M., and W. R. Cotton, 1989: A high plains squall line associated with severe surface winds. *J. Atmos. Sci.,* **46,** 281–302.

Schmocker, G. K., R. W. Przybylinski, and Y. J. Lin, 1996: Forecasting the initial onset of damaging downburst winds associated with a mesoscale convective system (MCS) using the midlatitude radial convergence (MARC) signature. Preprints, *15th Conf. on Weather Analysis and Forecasting,* Norfolk, VA, Amer. Meteor. Soc., 306–311.

——, ——, and E. N. Rasmussen, 2000: The severe bow echo event of 14 June 1998 over the mid-Mississippi valley region: A case of vortex development near the

intersection of a preexisting boundary and a convective line. Preprints, *20th Conf. on Severe Local Storms,* Orlando, FL, Amer. Meteor. Soc., 169–172.

Skamarock, W. C., M. L. Weisman, and J. B. Klemp, 1994: Threedimensional evolution of simulated long-lived squall lines. *J. Atmos. Sci.,* **51,** 2563–2584.

Smull, B. F., and R. A. Houze Jr., 1985: A midlatitude squall line with a trailing region of stratiform rain: Radar and satellite observations. *Mon. Wea. Rev.,* **113,** 117–133.

——, and ——, 1987: Rear-inflow in squall lines with trailing stratiform precipitation. *Mon. Wea. Rev.,* **115,** 2869–2889.

Trapp, R. J., and M. L. Weisman, 2003: Low-level mesovortices within squall lines and bow echoes. Part II: Their genesis and implications. *Mon. Wea. Rev.,* **131,** 2804–2823.

——, E. D. Mitchell, G. A. Tipton, D. W. Effertz, A. I. Watson, D. L. Andra Jr., and M. A. Magsig, 1999: Descending and non-descending tornadic vortex signatures detected by WSR- 88Ds. *Wea. Forecasting,* **14,** 625–639.

——, S. A. Tessendorf, E. S. Godfrey, and H. E. Brooks, 2005: Tornadoes from squall lines and bow echoes. Part I: Climatological distribution. *Wea. Forecasting,* **20,** 23–34.

Wakimoto, R. M., 1983: The West Bend, Wisconsin Storm of 4 April 1981: A problem in operational meteorology. *J. Appl. Meteor.,* **22,** 181–189.

——, Convectively Driven High Wind Events. 2001: *Severe Convective Storms, Meteor. Monogr.,* **50**, Amer. Meteor. Soc., 255-298 pp.

——, and J. W. Wilson, 1989: Non-supercell tornadoes. *Mon. Wea. Rev.,* **117,** 1113–1140.

Weisman, M. L., 1993: The genesis of severe, long-lived bow echoes. *J. Atmos. Sci.,* **50,** 645–670.

——, and J. B. Klemp, 1982: The dependence of numerically simulated convective storms on vertical wind shear and buoyancy. *Mon. Wea. Rev.,* **110,** 504–520.

——, and C. A. Davis, 1998: Mechanisms for the generation of mesoscale vortices within quasi-linear convective systems. *J. Atmos. Sci.,* **55,** 2603–2622.

——, and R. J. Trapp, 2003: Low-level mesovortices within squall lines and bow echoes: Part I. Overview and dependence on environmental shear. *Mon. Wea. Rev.,* **131,** 2779–2803.